Crystallographic study on microstructure and martensitic transformation of NiMnSb meta-magnetic multi-functional alloys

Chunyang Zhang

UNIVERSITÉ DE LORRAINE NORTHEASTERN UNIVERSITY

DISSERTATION

Presented at
Université de Lorraine and Northeastern University

Chunyang ZHANG 章春阳

To obtain the doctor's degree of
University of Lorraine and Northeastern University

SPECIAL FIELD: Engineering Sciences
OPTION: Materials Science

Crystallographic study on microstructure and martensitic transformation of NiMnSb meta-magnetic multi-functional alloys

Defended on March 28th, 2017 in front of the jury:

Leo KESTENS	Professor	Ghent University, Belgium	Reviewer & Jury member
Yinong WANG	Professor	Dalian University of Technology, China	Reviewer & Jury member
Yudong ZHANG	Doctor HDR	Université de Lorraine, France	Supervisor
Xiang ZHAO	Professor	Northeastern University, China	Supervisor
Claude ESLING	Professor	Université de Lorraine, France	Invited

Laboratoire d'Étude des Microstructures et de Mécanique des Matériaux, LEM3
Île du Saulcy, 57045 Metz Cedex 01, France

Abstract

NiMnSb based Heusler type alloys, as a novel multi-functional material has attracted considerable attention due to their multiple properties, such as magnetic shape memory effect, magnetocaloric effect, exchange bias effect, magnetoresistance effect. To date, many aspects of the NiMnSb alloys, such as crystal structure, microstructure, magnetic properties and mechanical properties *etc.*, have been widely investigated. However, many fundamental issues of this family of materials have not been fully revealed, which largely restricts the development of this new kind of multi-functional materials.

In the present work, a thorough investigation has been conducted on ternary NiMnSb alloys in terms of crystal structures of austenite and martensite; microstructural and crystallographic features of martensite; martensitic transformation orientation relationship (OR) and its correlation with variant organization; transformation deformation characteristics and self-accommodation of transformation strain.

The work confirmed that the austenite of NiMnSb alloys possesses a cubic $L2_1$ crystal structure belonging to the space group $Fm\bar{3}m$ (No. 225). The martensite has a four-layered orthorhombic (*4O*) structure with space group *Pmma* (No. 051). The lattice constants of the $Ni_{50}Mn_{37}Sb_{13}$ and $Ni_{50}Mn_{38}Sb_{12}$ martensite are a_M = 8.5830 Å, b_M = 5.6533 Å and c_M = 4.3501 Å, and a_M = 8.5788 Å, b_M = 5.6443 Å and c_M = 4.3479 Å, respectively.

The microstructure of the *4O* NiMnSb modulated martensite possesses a hierarchical organization feature. Martensite fine lamellae are first organized into broad plates. Each plate possesses 4 distinct twin related variants *A*, *B*, *C* and *D* forming type I twins (*A* and *C*; *B* and *D*), type II twins (*A* and *B*; *C* and *D*) and compound twins (*A* and *D*; *B* and *C*). The variant interfaces are defined by the corresponding twinning planes. The complete twinning elements for each twin relation are fully determined. The plates are further organized into sub-colonies and sub-colonies into plate colonies. The neighboring plates in one sub-colony and plate colony share one common plate interface orientation. Plate colonies with different oriented plate interfaces finally take the whole original austenite grain.

The Pitsch OR, specified as $\{0\bar{1}\bar{1}\}_A$ // $\{2\bar{2}\bar{1}\}_M$ and $<0\bar{1}1>_A$ // $<\bar{1}\bar{2}2>_M$, is the effective OR between the cubic austenite and the *4O* modulated martensite. Under this OR, a maximum of 24 distinct variants can be produced. The 24 variants are organized into 6 distinct variant colonies, 12 distinct sub-colonies and finally 6 distinct plate colonies. The twinning plane of type I twin and the intra-plate plate interfaces all correspond to the same family of $\{0\bar{1}\bar{1}\}_A$ planes of austenite.

The formation of martensite variant colonies can be both form intragranular and intergranular during the phase transformation. The sandwich structured variant colony is the basic microstructural unit of the martensite. This structure is composed of twin related variants and possesses the full compatible inner variants interfaces and invariant habit planes. The deformation manner of the twin related variants result in the high occurrence frequency of the type II twins and affects the morphology of the sandwich colonies. The wedge-shaped structure is composed of two compatible sandwiches and conjoined by a midrib plane with a small atomic misfit. All these results indicate that the martensitic transformation is self-accommodated and the microstructure is determined by the self-accommodation of the microstructural constituents.

The aim of this work is to provide fundamental crystallographic and microstructural information of NiMnSb alloys for interpreting their magnetic and mechanical characteristics associated with the martensitic transformation and further investigations on property optimization.

Keywords: NiMnSb multi-functional alloys; Twin relationship; Martensitic transformation; Orientation relationship; Crystallography; Deformation gradient tensor; Self-accommodation.

Résumé

Les alliages NiMnSb, matériaux multifonctionnels nouveaux, ont attiré une attention en raison de leurs multiples propriétés, telles que l'effet de mémoire de forme, magnétocalorique, de biais d'échange, de magnétorésistance. Jusqu'à présent, de nombreux aspects des NiMnSb, tels que structure cristalline, microstructure, propriétés magnétiques et mécaniques ont été étudiés. Cependant, de nombreuses questions fondamentales de ces matériaux n'ont pas été entièrement révélées, ce qui limite leur développement.

Une étude a été menée sur les alliages ternaires NiMnSb en termes de structures cristallines de l'austénite et de la martensite; Caractéristiques microstructurales et cristallographiques de la martensite; La relation d'orientation (OR) de transformation martensitique et sa corrélation avec l'organisation des variantes; Les caractéristiques de déformation de la transformation et l'auto-accommodation de la déformation de transformation.

Le travail a confirmé que l'austénite possède une structure cristalline $L2_1$ cubique, groupe spatial $Fm\bar{3}m$ (No. 225). La martensite a une structure orthorhombique modulée (*4O*) à quatre couches, groupe spatial *Pmma* (No. 051). Les constantes de réseau de martensite de $Ni_{50}Mn_{37}Sb_{13}$ et $Ni_{50}Mn_{38}Sb_{12}$ sont a_M = 8.5830 Å, b_M = 5.6533 Å et c_M = 4.3501 Å, et a_M = 8.5788 Å, b_M = 5.6443 Å et c_M = 4.3479 Å.

La microstructure de la martensite *4O* NiMnSb modulée possède une caractéristique d'organisation hiérarchique. Les lamelles fines de martensite sont d'abord organisées en larges plaques. Chaque plaque possède 4 variantes apparentées aux jumeaux *A*, *B*, *C* et *D* formant des jumeaux de type I (*A* et *C*, *B* et *D*), de type II (*A* et *B*, *C* et *D*) et des macles composéés (*A* et *D*; *B* et *C*). Les interfaces des variantes sont définies par les plans de maclage correspondants. Les éléments de maclage sont entièrement déterminés pour chaque relation de maclage. Les plaques sont ensuite organisées en sous-colonies et les sous-colonies en colonies de plaques. Les plaques voisines d'une sous-colonie et d'une colonie de plaques partagent une interface de plaque commune. Des colonies de plaques avec différentes interfaces de plaques ayant différentes orientations occupent finalement l'ensemble du grain d'austénite original.

La OR de Pitsch, spécifiée comme $\{0\bar{1}\bar{1}\}_A$ // $\{2\bar{2}\bar{1}\}_M$ et $<0\bar{1}1>_A$ // $<\bar{1}\bar{2}2>_M$, est l'OR effective entre l'austénite cubique et la martensite *4O* modulée. Sous cette OR, un maximum de 24 variantes distinctes peuvent être produites. Les 24 variantes sont organisées en 6 colonies de variantes distinctes, 12 sous-colonies distinctes et enfin 6 colonies de plaques distinctes. Le plan de maclage de type I et les interfaces intra-plaques correspondent tous à la même famille de plans $\{0\bar{1}\bar{1}\}_A$ de austénite.

La formation des colonies de variantes martensitiques peut être à la fois intragranulaire et intergranulaire pendant la transformation de phase La colonie de variantes structurée en sandwich est l'unité micro-structurale de base de la martensite. Cette structure est composée de variantes de relation macles et possède des interfaces de variantes internes totalement compatibles et les plans d'habitat invariants. Les caractéristiques de déformation des variants en relation de macles conduisent à la fraction de volume élevée de macles de type II et affecte la morphologie des colonies en sandwich. La structure en forme de coin est composée de deux sandwichs compatibles et reliés par un plan de nervure médiane avec une petite incompatibilité atomique. Tous ces résultats indiquent que la transformation martensitique est auto-accommodée et la microstructure est déterminée par l'auto-accommodation des constituants microstructuraux.

Ce travail vise à fournir des informations cristallographiques et micro-structurales fondamentales des alliages NiMnSb pour l'interprétation de leurs caractéristiques magnétiques et mécaniques associées à la transformation martensitique et des recherches complémentaires sur l'optimisation des propriétés.

Mots-clés: Alliages multifonctionnels NiMnSb; Relation de macle; Transformation martensitique; Relation d'orientation; Cristallographie; Tenseur gradient de déformation; Auto-accommodation.

摘要

NiMnSb 系列合金作为一种新型的多功能合金因其多重的优越能性，如磁形状记忆效应，磁热效应，交换偏执效应以及磁阻效应，受到了人们广泛的关注。直至目前，有关该材料的晶体结构，微观组织，磁性能以及机械性能等方面的研究均有广泛的报道。然而有关该材料的许多基本知识还未得到完整的解决，这极大的限制了对该材料研究的进展。

在本论文工作中选用了三组元 NiMnSb 合金为研究对象，对其马氏体相与奥氏体相晶体结构、马氏体相的微观组织与晶体学特征、马氏体相变取向关系及变体组织特征以及相变应变的变形特征与自协调性等问题进行了深入的研究。

研究结果表明，NiMnSb 合金的奥氏体相具有立方 $L2_1$ 晶体结构，对应的空间群为 $Fm\bar{3}m$ (No. 225)。马氏体相具有四层调制的正交晶体结构（*4O*），对应空间群为 *Pmma* (No. 051)。$Ni_{50}Mn_{37}Sb_{13}$ 与 $Ni_{50}Mn_{38}Sb_{12}$ 合金马氏体相的晶格参数分别为 a_M = 8.5830 Å，b_M = 5.6533 Å，c_M = 4.3501 Å 以及 a_M = 8.5788 Å，b_M = 5.6443 Å，c_M = 4.3479 Å。

该调幅马氏体相的微观组织在构成上具有很强的层次性。呈现出细板条形状的马氏体变体首先构成马氏体宽板条，即马氏体变体团。在每个宽板条内存在四种晶体学取向上彼此独立的 *A*、*B*、*C* 和 *D* 马氏体变体。四种变体两两间具有孪生取向关系，可构成 I 型（变体对 *A*:*C* 及 *B*:*D*）、II 型（变体对 *A*:*B* 及 *C*:*D*）及复合型（变体对 *A*:*D* 及 *B*:*C*）孪生三种不同的孪生关系。不同变体间的界面与它们所对应的孪晶界面重合。上述三种类型孪晶的孪生要素已被全部解析。随后，马氏体宽板条又可构成马氏体亚板条团，而亚板条团可进一步组成板条团。在同一亚板条团及板条团中，相邻的两两马氏体板条间具有相同的板条间界面。最终，具有不同取向的板条间界面的板条团组成了原始奥氏体晶粒。

在该合金的马氏体相变过程中，具有立方结构的母相奥氏体与具有正交调幅结构的马氏体间遵循着 Pitsch 取向关系，即$\{0\bar{1}\bar{1}\}_A$ // $\{2\bar{2}\bar{1}\}_M$、$<0\bar{1}1>_A$ // $<\bar{1}\bar{2}2>_M$。在该取向关系下，每个原始奥氏体晶粒中可产生 24 种取向独立的马氏体变体。这 24 种变体可继续构成 6 种独立的变体团、12 种独立的亚板条团，最终形成 6 个独立的板条团。I 型孪生的孪晶面及板条间界面均对应于奥氏体的$\{0\bar{1}\bar{1}\}_A$ 面。

在马氏体相变过程中，马氏体变体团分别可在晶粒内及晶界处产生。新生成的马氏体相以三明治结构的变体团作为基本的微结构单元。该种结构有具有孪生关系的马氏体变体对组成。其内部的变体间界面与外围的同奥氏体交接的惯习面在原子尺度上是完全兼容的。具有孪生关系的变体对的变形特点决定了在该材料微观组织中 II 型孪生占据主要地位，且其也可对三明治结构变体团的形貌特征产生影响。楔形变体团是由两个完全兼容的三明治变体团组合而成。连接两三明治变体团的是一具有较小原子错配度的中脊面，且该面对应于奥氏体的$\{0\bar{1}\bar{1}\}_A$面。上述结果表明马氏体相变是自洽的，其微观组织是由相互自洽的各组分所组织而成。

本论文的所有研究工作提供了 NiMnSb 合金的详尽的、基本的晶体学及微观组织特征信息，为深入理解该材料中与马氏体相变密切相关的磁性能及机械性能以及进一步的性能优化提供了帮助。

关键词：NiMnSb 多功能合金；孪生关系；马氏体相变；取向关系；晶体学；变形矩阵；自洽。

List of the frequently-used abbreviations

4O	Four-layered orthorhombic
$\boldsymbol{\eta_1}$	Twinning direction
γ	Magnitude of shear
A_f	Austenitic transformation finish temperature
A_s	Austenitic transformation start temperature
BSE	Backscattered electron
DSC	Differential scanning calorimetry
EBSD	Electron backscatter diffraction
H_{EB}	Exchange bias field
K_1	Twinning plane
M_{EB}	Exchange bias magnetization
M_f	Martensitic transformation finish temperature
M_s	Martensitic transformation start temperature
MCE	Magnetocaloric effect
MFIS	Magnetic-field-induced strain
MSMA	Magnetic shape memory alloys
MSME	Magnetic shape memory effect
ND	Neutron diffraction
OR	Orientation relationship
RC	Refrigeration capacity
SAED	Selected area electron diffraction
SEM	Scanning electron microscope
SMA	Shape memory alloy
SME	Shape memory effect
T_C^A	Curie temperature of austenite
XRD	X-ray diffraction

Contents

Chapter 1 Literature review

1.1 General introduction

Multi-functional materials, as supporting materials for the development of many scientific domains, such as information technology, energy science, aerospace science and technology and so on, are highly valued by the governments and widely investigated by researchers in the past decades. Generally, this kind of materials can produce some specific functions by an external stimulation, such as light, electric current, magnetic field, stress and heat. Among these materials, the shape memory alloys (SMAs) as a new kind of multi-functional materials have attracted great attention with its advantageous mechanical properties. The first discovery of the shape memory effect (SME) was in an Au - 47.5 at. % Cd alloy in 1951 [1] by studying the movement of the boundaries between the *B2* cubic austenite and the *B19* orthorhombic martensite [2] during the martensitic transformation. Later, the same effect was discovered in a Ni-Ti alloy in 1963 [3]. Since then, SMAs such as NiTi-based (NiTiCu [4-7], NiTiFe [8, 9], NiTiNb [10, 11], NiTiPd [12, 13], *etc.*), Cu-based (CuAlNi [14-16], CuZnAl [17, 18], *etc.*), Fe-based (FeMnSi [19], FePt [20], *etc.*) alloys, which are confirmed to have potential applications in automotive [21] and aeronautic [22, 23] industries, have been developed rapidly. Among these materials, the Ni-Ti based SMAs are regarded as the best ones since they have high strain (up to ~ 8 % [24]). However, the SME of these kind of materials is originated from the reversible martensitic transformation that is driven by a temperature field. Thus, the working frequency is very low, which greatly restricts the development and applications of these materials.

To overcome this disadvantage, magnetic shape memory alloys (MSMAs) were developed in recent years. The common MSMAs contain NiMn-based (NiMnGa [25-28], NiMnIn [29-31], NiMnSn [32, 33], NiMnSb [34-36], NiMnAl [37]), NiFeGa [38, 39], CoNiGa systems [40] and so on. Among these MSMAs, the NiMnX (X = Ga, In, Sn, Sb) alloy systems have been considered to be the most promising ones. Different from the traditional SMAs, these materials can associate the martensitic transformation with their magnetic properties. Thus, the MSMAs

with their magnetic transition temperature at the vicinity of martensitic transformation can realize phase transformation under an external magnetic field incentivisation. The magnetic shape memory effect (MSME) was first detected by applying an external magnetic field to a Hustler type Ni_2MnGa alloy in 1996 (~ 0.2 % strain along the [001] direction) [41]. Later, investigations on enhancing the strain and stress of these materials are widely carried out. To date, the highest magnetic field induced strain of the NiMnGa alloys has amounted up to 12 %, which is detected in a quinary $Ni_{46}Mn_{24}Ga_{22}Co_4Cu_4$ alloy [42]. Moreover, the work frequency of NiMnGa alloys has reached up to kHz [43, 44]. Such an excellent MSME is originated from the rearrangement of the martensite variants through interface movements driven by the external magnetic field. However for the other MSMAs systems, the NiMnX (X = In, Sn, Sb) alloys, the origin of the MSME is quite different from NiMnGa alloys. In these alloys, the magnetism of austenite is much higher than that of martensite, so the martensitic transformation experiences a considerable magnetism drop. Hence, a magnetic induced reverse martensitic transformation phenomenon can be detected in these alloys [30]. When the materials are prestrained before reverse martensitic transformation, the reversible phase transformation under a magnetic field cycle can realize a shape change cycle, hence shape memory effect. In addition, the sharp change of the magnetism accompanying the martensitic transformation also results in many different magnetic effects, such as the magnetocaloric effect (MCE) [45-47], magnetoresistance effect [48-50], and kinetic arrest effect [51]. Moreover, since the martensitic transformation of the NiMnX (X = In, Sn, Sb) alloys is detected in the off-stoichiometric (Mn rich) Heusler type alloys [34], the interaction between the Mn-Mn atoms also leads to an ferromagnetism and antiferromagnetism interaction [52-54] below the Néel temperature. All these novel properties of these materials provide them with great potential as magnetic shape memory materials, magnetic refrigeration materials and magnetic recording materials. Hence, investigations on these materials have been widely carried out in the past decade and these materials also became one of the most promising multi-functional materials.

1.2 State-of-the-art of NiMnSb multi-functional alloy systems

This thesis selects the ternary NiMnSb alloys systems as the research materials. According to the chemical composition of the reported alloys and their specific magnetic properties, the investigations of NiMnSb alloys can be divided into two parts: one is the half-Heusler type NiMnSb alloy and the other is the off-stoichiometric Heusler type $Ni_{(2-x)}Mn_{(1+x+y)}Sb_y$ ($0 < x, y < 1$) alloys. Since the first discovery of the NiMnSb alloy as a half-metallic ferromagnets in 1980s [55], researchers have mainly focused on preparing the half-metallic ferromagnetic NiMnSb thin films using magnetron sputtering and studying the magneto-optical, magnetic and resistivity properties [56-58]. The specific electronic structure of this material makes it valuable candidate materials in the domains of spintronics, spin-electron device and microelectronics. Later in 2004, the martensitic transformation was found in the off-stoichiometric Heusler type $Ni_{50}Mn_{37}Sb_{13}$ alloy [34], this granted it special value as MSMA. In addition, with the multiple magnetic properties mentioned above [47, 50, 54] discovered in this kind of alloys, more and more researchers pay attention to these materials. To date, almost all of the investigations on this kind of materials are on the magnetic properties, and few are on the crystal structures, magnetic structures or martensitic transformation features. Next, the research results on the off-stoichiometric, Mn rich Heusler type NiMnSb alloys will be overviewed in details.

1.2.1 Crystal structure of NiMnSb alloys

As is known, the crystal structures of the constituent phases as basic information of a material is of great importance for many related investigations, such as microstructure, crystallographic features, mechanical properties and so on. The conventional examination methods consisting of the X-ray diffraction (XRD), the neutron diffraction (ND) and the transmission electron microscope (TEM) selected area electron diffraction (SAED) have been applied to investigate the crystal structures of NiMnSb austenite and martensite in the past decade. It is clear that the high temperature austenite processes a cubic $L2_1$ structure, whereas for martensite, its structure varies with the composition. Both modulated and non-modulated structures have been reported in ternary NiMnSb alloys with different compositions. In addition, different structures have been reported for some alloys with the same composition. Hence, the crystal structure of NiMnSb martensite is complicated and the reports on it are not consistent.

As the basis of crystallographic analysis as well as the related physical properties, the detailed crystal structure information is essential.

1.2.1.1 Crystal structure of austenite

Like other NiMn-based (NiMnGa, NiMnIn and NiMnSn) alloys, the high temperature phase – austenite, was confirmed to possess an $L2_1$ (space group: No. 225, $Fm\bar{3}m$) cubic crystal structure, which has been demonstrated by XRD [36, 59-76] and ND [77-79] measurements. Using the $L2_1$ structure information of Ni_2MnSb austenite reported in [60] for lattice parameters and in [77] for atomic position information as an example, the crystal structure of austenite with stoichiometric composition is illustrated in **Fig. 1.1**.

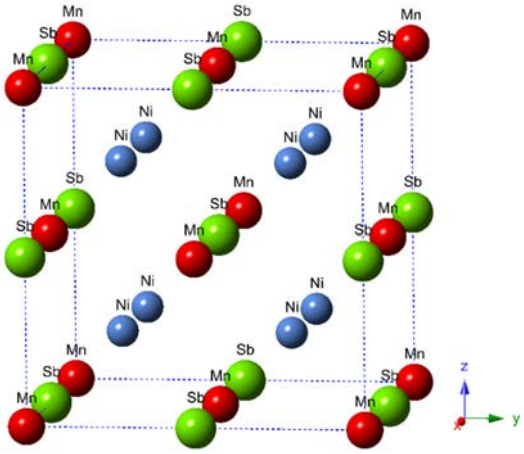

Fig. 1.1 Illustration of a unit cell of Ni_2MnSb austenite.

It can be seen in **Fig. 1.1** that the $L2_1$ structure is highly ordered with a high symmetry. It can be represented by 4 interpenetrating face-centred cubic sublattices: Mn atoms at the *4a* (0, 0, 0) positions, Sb atoms at the *4b* (0.5, 0.5, 0.5) positions, Ni atoms at the *8c* (0.25, 0.25, 0.25) positions and Ni atoms at the *8c* (0.75, 0.75, 0.75) positions. When the composition is Mn rich, *i.e.* off-stoichiometric, the excess Mn atoms will occupy the *4b* position of Sb atoms in $Ni_2Mn_{(1+x)}Sb_x$ ($0 < x < 1$) type alloys, and *4b* and *8c* positions of Sb and Ni atoms in $Ni_{(2-x)}Mn_{(1+x+y)}Sb_y$ ($0 < x, y < 1$) type alloys. However the structure is still of $L2_1$ cubic type [77-79].

1.2.1.2 Crystal structure of martensite

Different from the explicit structure of austenite, the crystal structure of the low–temperature martensite is under clarification. In the past decade, the crystal structure of NiMnSb

martensite have been investigated using XRD [59, 61, 67-69, 71, 73-76, 80, 81], ND [77, 79, 82] and SAED [34]. All the reported experimental results show that the martensite phase possesses an orthorhombic crystal structure. The results are summarized and shown in **Table 1.1**.

Table 1.1 Reported crystal structure information of NiMnSb martensite

Composition	Reference, Year & Experiment	Space group/ Structure	Lattice parameters (a, b, c) (Å)
$Ni_{50}Mn_{37}Sb_{13}$	[34] 2004 SAED	*4O* ($2\bar{2}$)	(4.305, 2.885, 8.407)
$Ni_{50}Mn_{38}Sb_{12}$	[76] 2008 XRD	*Pmm2*	(4.289(1), 5.670(1), 21.564(1))
$Ni_{50}Mn_{37.5}Sb_{12.5}$			(4.296(1), 5.645(1), 21.474(1))
$Ni_{50}Mn_{37}Sb_{13}$			(4.303(1), 5.668(1), 21.467(1))
$Ni_{50}Mn_{37.5}Sb_{12.5}$	[75] 2009 XRD	*Pmma* & *Pnnm*	(4.3654, 5.5930, 8.5875) *Pmma* —— *Pnnm*
$Ni_{50}Mn_{40}Sb_{10}$			(4.3764, 5.5426, 8.5669) *Pmma* —— *Pnnm*
$Ni_{50}Mn_{45}Sb_{5}$		*P4/mmm* & *Pnnm*	(7.6489, 7.6489, 6.9967) *P4/mmm* (4.2446, 28.8246, 5.5627) *Pnnm*
$Ni_{50}Mn_{38}Sb_{12}$	[80] 2009 XRD	Orthorhombic	(4.29, 21.56, 5.67)
$Ni_{50}Mn_{38.5}Sb_{11.5}$			(4.30, 21.47, 5.65)
$Ni_{50}Mn_{38}Sb_{12}$	[73] 2009 XRD	*Pmma*	(8.560, 5.565, 4.351)
$Ni_{50}Mn_{37}Sb_{13}$	[79] 2010 ND	*Pmma*	(8.553(2), 5.590(2), 4.342(2)) 5K
$Ni_{50}Mn_{36.5}Sb_{12.5}B_{1}$	[71] 2010 XRD	*4O Pmma*	(8.593, 5.662, 4.350)
$Ni_{50}Mn_{36.5}Sb_{12}B_{1.5}$			(8.579, 5.660, 4.341)
$Ni_{50}Mn_{38}Sb_{12}B_{1}$	[67] 2011 XRD	*4O*	(8.574(8), 5.625(3), 4.348(1))
$Ni_{50}Mn_{38}Sb_{12}$	[77] 2014 ND	*Pmma*	(8.59(2), 5.56(2), 4.38(2)) 6K (8.60(2), 5.56(2), 4.38(2)) 300K
$Ni_{45}Mn_{38}Co_{5}Sb_{12}$			(8.57(2), 5.57(2), 4.36(2)) 6K
$Ni_{50}Mn_{38}Sb_{12}$	[68] 2011 XRD	*Pmma*	(8.574(8), 5.625(3), 4.348(1))
$Ni_{50}Mn_{37}Sb_{13}$	[82] 2011 ND	*Pmma*	(8.573(2), 5.7144(9), 4.3272(9)) 270K

'——' represents the related lattice parameters having not been given in the literature.

Among the above investigations, the crystal structure of $Ni_{50}Mn_{37}Sb_{13}$ martensite was firstly investigated by Sutou *et al.* using TEM in 2004 [34]. According to the SAED pattern

obtained, they suggested that it has a four-layered orthorhombic (*4O*, where '*O*' stands for orthorhombic) ($2\bar{2}$) crystal structure. In addition, they pointed out that the modulation direction is along the *a*-axis and one martensite unit cell contains two sub cells arranged along the *c*-axis. For explicitly, we refer the direction or axis along which the sub cells stack as the stacking direction or axis. Later, Khan *et al.* carried out a thorough investigation on the crystal structure of $Ni_{50}Mn_{(25+x)}Sb_{(25-x)}$ alloys using XRD [76]. They found that when $x \geq 13$, the alloys possess a modulated orthorhombic structure with space group *Pmm2* (No. 025). However they thought that one martensite unit cell contains more sub cells and the stacking direction is along the *c*-axis, which can be seen from the given lattice parameters in **Table 1.1**. In 2009, Aksoy *et al.* studied the effect of changing Sb-concentration on phase composition and the corresponding crystal structure of $Ni_{50}Mn_{(50-x)}Sb_x$ alloys using XRD (Co *Kα* radiation) [75]. The results revealed that for $x \leq 12.5$, the alloys were in martensite state. By XRD pattern simulation, they found that the martensite phase of $Ni_{50}Mn_{37.5}Sb_{12.5}$ and $Ni_{50}Mn_{40}Sb_{10}$ alloys possesses a mixed orthorhombic structures, one being *4O* with space group *Pmma* (No. 051) (stacking direction: *c*-axis) and the other is seven-fold (7-fold) [75] modulated orthorhombic structure with space group *Pnnm* (No. 058) (stacking direction: *b*-axis). Moreover, they also studied the crystal structure of $Ni_{50}Mn_{45}Sb_5$ alloy and found a 7-fold orthorhombic and $L1_0$ tetragonal (space group: *P4/mmm* (No.125)) mixed structure. It was the first time that an $L1_0$ structure is reported for the NiMnSb martensite. Similarly, Dubenko *et al.* also reported such an orthorhombic structure with the *b*-axis as the stacking direction, like the 7-fold orthorhombic structure [75] discovered in $Ni_{50}Mn_{38}Sb_{12}$ and $Ni_{50}Mn_{38.5}Sb_{11.5}$ alloys [80]. For the *4O* structure, Rao *et al.* also held a different opinion from that of Aksoy *et al.* on the stacking direction [73]. From the XRD patterns obtained at different temperatures of $Ni_{50}Mn_{38}Sb_{12}$, they observed the changes of the diffraction peaks during the heating process (reverse martensitic transformation process) and concluded that the stacking direction is along the *a*-axis. This structure was later confirmed in some other ternary and quaternary NiMnSb alloys [61, 68, 71, 77, 79, 82]. However, Najak *et al.* thought that this structure should be a ten-layered modulated orthorhombic but not *4O*.

It can be seen that, owing to the presence of structural modulation, there exist controversies over the modulation period, the direction and the space group. The alloys with the same or

similar compositions were reported to possess different crystal structures in different studies. Since the crystal structure information is prerequisite for crystallographic orientation analyses, it is necessary to obtain accurate crystal structure information of these alloys.

1.2.2 Microstructure of NiMnSb alloys

It is known that the properties of the NiMnX (X = In, Sn, Sb) alloys, especially the shape memory effect, are closely related to the microstructure features of the parent austenite and the product martensite. As a kind of multi-functional material, the improvement of the properties are extremely important and of significance. Hence, a thorough investigation of the microstructure characteristics of NiMnSb alloys is essential. However, the study is at the beginning state.

Rao *et al.* were the very first to conduct such study. With the help of scanning electron microscope (SEM), they observed the microstructures of $Ni_{50}Mn_{38}Sb_{12}$ martensite for the first time [73]. The backscattered electron (BSE) micrograph of martensite is shown in **Fig. 1.2**. They observed that the $Ni_{50}Mn_{38}Sb_{12}$ martensite has a surface relief and is composed of large amount of thin plates (~ 5 μm wide) with different stretch directions. They believed that these martensite plates should be twin related.

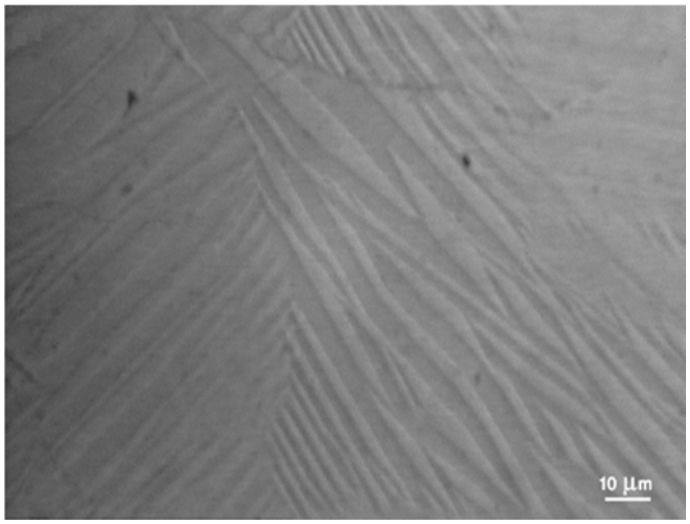

Fig. 1.2 Backscattered electron (BSE) micrograph of $Ni_{50}Mn_{38}Sb_{12}$ martensite [73].

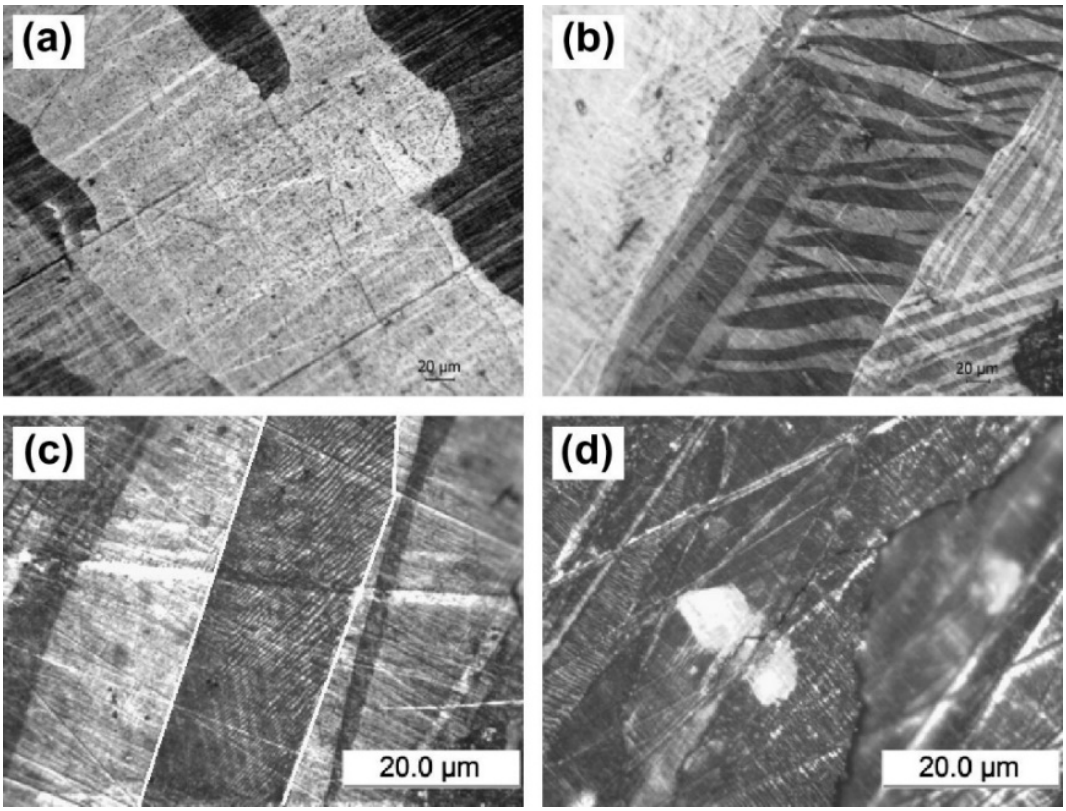

Fig. 1.3 Optical microscope images taken at room temperature for: (a) $Ni_{45}Co_5Mn_{38}Sb_{12}$ taken before temperature cycling, (b) $Ni_{48}Co_2Mn_{38}Sb_{12}$ taken before temperature cycling, (c) $Ni_{48}Co_2Mn_{38}Sb_{12}$ taken with higher magnification and (d) $Ni_{48}Co_2Mn_{38}Sb_{12}$ taken after temperature cycling [83].

Nayak *et al.* studied the effects of repeated martensitic transformation on thermal and magnetic properties in NiCoMnSb alloys [83]. They used the optical microscope (OM) to observe the original microstructures of $Ni_{45}Co_5Mn_{38}Sb_{12}$ austenite and $Ni_{48}Co_2Mn_{38}Sb_{12}$ martensite before temperature cycling as shown in **Fig. 1.3**(a) and **Figs. 1.3**(b) and (c). Similar to the microstructure features of the ternary NiMnSb martensite, the NiCoMnSb martensite also consists of large amount of broad plates with different widths and orientations. Within the broad plates, many fine lamellae can also be observed. After the temperature cycling, the martensite phase still presents the plate-like microstructure. However, many microcracks are generated along the boundaries between the neighboring broad plates, as shown in **Fig. 1.3**(d). This resulted from the poor mechanical properties of this material. They pointed out that the appearance of these microcracks plays an important role in increasing the resistivity of this material.

To sum up, both the OM and SEM observations demonstrated that the martensite of NiMnSb alloys possesses a plate-like microstructure. In addition, twin relationships between neighboring fine lamellae have been speculated. However, all these investigations are confined to morphological observation. Due to the absence of the detailed crystal structure information, further crystallographic information of NiMnSb martensite *e.g.* twin type, twinning elements, twin interface planes, variants distribution, *etc.* is not available, imposing difficulty in interpreting the microstructure-related properties of these alloys. Hence, the corresponding studies is necessary and can provide fundamental information for these alloys, which will be useful for further investigations on properties optimization of NiMnSb alloys.

1.2.3 Multiple performance of NiMnSb alloys

As magnetic materials, the occurrence of many magnetic responses in NiMnSb alloys always accompanies the structural and magnetic transitions. Generally, in NiMnSb alloys, there exist one first-order and two second-order phase transformations: martensitic transformation (from high-temperature austenite to low-temperature martensite), paramagnetism-ferromagnetism transition in austenite and paramagnetism-antiferromagnetism transition in martensite, corresponding to three characteristic temperatures: martensitic transformation temperature, Curie temperature and Néel temperature, respectively. The MSME, MCE, exchange bias effect and magnetoresistance effect are all closely related to these transformations. Since these properties make the materials potential candidates as magnetic shape memory, magnetic refrigeration and magnetic recording materials, many investigations have been carried out on properties optimization and enhancement.

1.2.3.1 Magnetic shape memory effect

In NiMnSb alloys, the MSME is originated from the magnetic-field-induced strain (MFIS). Since the parent austenite is a high-magnetism phase, the application of an external magnetic field could stimulate the reverse martensitic transformation in these alloys. The relationship between the intensity change of the external magnetic field ΔH and the drop of the phase transformation temperature ΔT can be associated with the following Clausius–Clapeyron relation [30]:

$$\Delta T \approx \left(\frac{\Delta M}{\Delta S}\right) \Delta H. \tag{1.1}$$

Here ΔM and ΔS are the differences of the magnetization and entropy between austenite and martensite. Obviously, these two parameters are two decisive factors to the magnetic driving capability. Hence, the alloys whose Curie temperature of austenite (T_C^A) is higher than the martensitic transformation temperature are more favorable as the MSMAs.

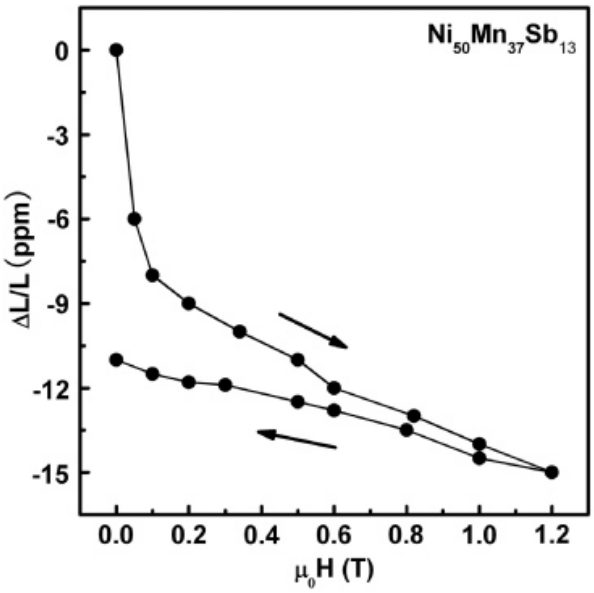

Fig. 1.4 Recovery strain at 290 K induced by a magnetic field for $Ni_{50}Mn_{37}Sb_{13}$ polycrystalline alloy [36].

To date, the investigations of the MSME in NiMnSb alloys are not numerous. Du *et al.* studied the recovery strain induced by the magnetic field in a polycrystalline $Ni_{50}Mn_{37}Sb_{13}$ alloy [36]. **Fig. 1.4** shows the strain versus magnetic field curves for $Ni_{50}Mn_{37}Sb_{13}$ polycrystalline alloy (without prestrain). It can be seen that, a 15 ppm recovery strain was obtained under a 1.2 T magnetic field, and ~ 4 ppm strain was detected in the removing process of the magnetic field. Higher recovery strain could be acquired by increasing the intensity of the external magnetic field, since the recovery strain has not reached saturation at 1.2 T. Hence, a reversible, two-way MSME was detected in this alloy.

Yu *et al.* investigated large temperature and MFIS in polycrystalline NiMnInSb alloys [35]. **Figs. 1.5**(a) and (b) show the temperature and magnetic field dependence of the spontaneous phase transformation for NiMnInSb alloys. In **Fig. 1.5**(a), it can be seen that with the increasing

of the Sb concentration, a ± 1.7 % spontaneous phase transformation strain was obtained during the cooling and heating processes for $Ni_{50}Mn_{36}In_8Sb_6$ alloy, which has been largely enhanced compared with the Sb-free $Ni_{50}Mn_{36}In_{14}$ alloy (∓ 0.08 %). By applying a magnetic field to the $Ni_{50}Mn_{36}In_8Sb_6$ alloy at 295 K (in martensite state), a magnetic-field-induce reverse martensitic transformation and a large strain (up to 1.7 % at 9 T magnetic field) was detected as shown in **Fig. 1.5**(b). In the removing process of the magnetic field, no reversible length change was detected. These results indicate that the magnetic field induced MSME is not reversible. It happens only during the magnetic-field-induced reverse martensitic transformation.

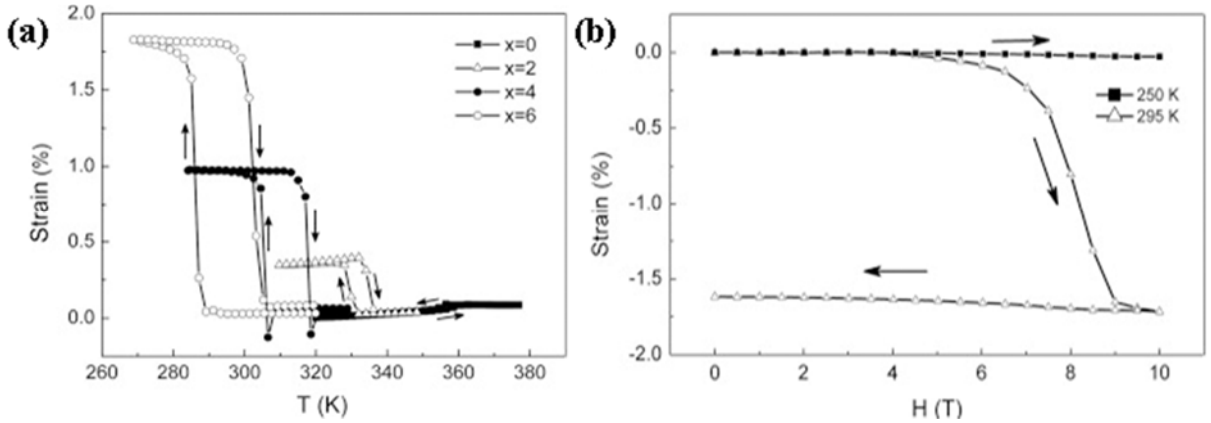

Fig. 1.5 (a) Temperature dependence of the spontaneous phase transformation strain for $Ni_{50}Mn_{36}In_{(14-x)}Sb_x$ (x = 0, 2, 4, 6) alloys and (b) field dependence of the strain for polycrystalline $Ni_{50}Mn_{36}In_8Sb_6$ alloy that measured along the direction of sample solidification during arc melting [35].

To date, a reversible, two-way MSME has been detected in ternary $Ni_{50}Mn_{37}Sb_{13}$ polycrystalline alloy. With the doping of Sb element, the spontaneous phase transformation strain of polycrystalline NiMnIn alloys was largely enhanced. In addition, a large strain that is originated from the magnetic-field-induced reverse martensitic transformation was also detected in this alloy. Although large MFIS are frequently reported in NiMnGa alloys systems, the excellent MSME is only achieved in single crystal. As is known, the cost of single crystal preparation is much higher than polycrystalline alloy preparation. The shape and size of the single crystal alloy is also largely restrained. Moreover, the price of Ga element, as well as In and Sn elements, is much more expensive than Sb. All these factors determine that the

polycrystalline NiMnSb alloys should be a promising candidate as cost-economic and performant MSMAs.

1.2.3.2 Magnetocaloric effect and magnetic refrigeration

The MCE is a thermal-magnetic property of magnetic materials. It represents a temperature change under an actuating magnetic field. To characterize this property, one conventional way is to calculate the maximum entropy change (ΔS_m) of the material under an applied magnetic field around the Curie temperature or martensitic transformation temperature with the help of the measured isothermal magnetization curves and the integrating Maxwell relation:

$$\Delta S(T,H)_M = \int_0^H \left(\frac{\partial M}{\partial T}\right)_H dH\,. \tag{1.2}$$

Then, with the obtained $\Delta S(T,H)_M$ curve, the refrigeration capacity (RC) can be calculated by integrating the curve over the full width at half maximum using the following equation:

$$RC = \int_{T_1}^{T_2} \Delta S_M dT\,. \tag{1.3}$$

It should be emphasized that, this RC is composed of two parts: one is the hysteresis loss and the other is the effective RC. Hence, to acquire the effective RC, the hysteresis loss need to be calculated by integrating the measured Isothermal hysteresis loops.

Fig. 1.6 shows an illustration of the MCE in NiMnX (X = In, Sn, Sb) alloys [45]. Here we consider an adiabatic magnetization process. When an external magnetic field is applied to the paramagnetic martensite, the magnetic moments will be aligned in the field direction. Then the magnetic entropy will be reduced and the material will be heated and release heat to the environment, as shown by the top figures in **Fig. 1.6**. If the magnetic field is applied near the martensitic transformation temperature, it will induce reverse martensitic transformation. As the transformation involves entropy increase from martensite to austenite, under an adiabatic circumstance, the material will be cooled down, as shown by the figures in the middle of **Fig. 1.6**. The net MCE is a summation of these two MCEs: the MCE from magnetic spin alignment and from structural transition. As the latter effect is higher than the former, the resultant effect

is a temperature decrease of the material. Hence, the material will absorb heat from the environment and generate a magnetic refrigeration effect.

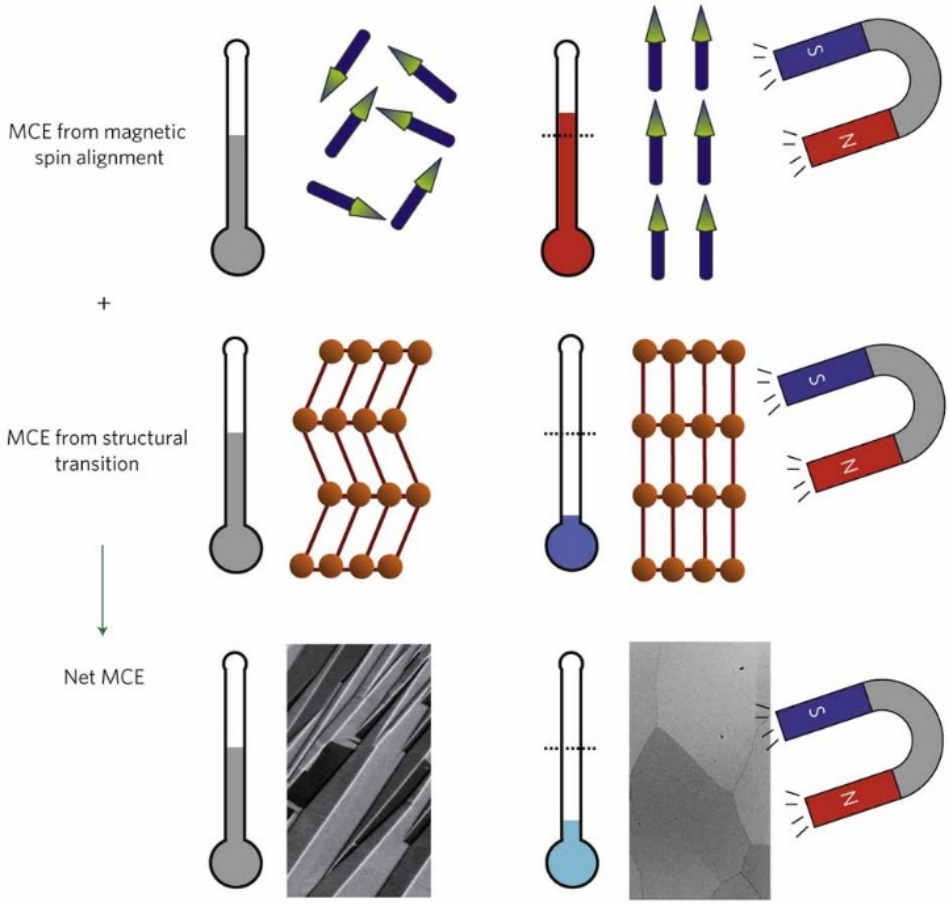

Fig. 1.6 Contributions from the magnetic and structural part for a first-order magnetic transition to the magnetocaloric effect (MCE) [45].

The investigation of MCE for NiMnSb alloys systems was conducted in ternary $Ni_{50}Mn_{(37+x)}Sb_{(13-x)}$ (x = 0, 0.5, 1) polycrystalline bulk alloys for the first time in 2007 [47]. A ΔS_m of 19.1 $J\cdot(kg\cdot K)^{-1}$ and 8.9 $J\cdot(kg\cdot K)^{-1}$ were obtained at 297 K by applying a 5 T and 2 T external magnetic fields for $Ni_{50}Mn_{38}Sb_{12}$ alloy. In addition, the RC of $Ni_{50}Mn_{37}Sb_{13}$ alloy was also studied. Results show that it possesses a ~ 32 $J\cdot kg^{-1}$ for RC, while the hysteresis loss is ~ 13 $J\cdot kg^{-1}$. Hence, the effective RC is ~ 19 $J\cdot kg^{-1}$. Obviously, the large hysteresis loss in $Ni_{50}Mn_{(37+x)}Sb_{(13-x)}$ system is an obstacle for its use as a competent magnetic refrigeration material.

The MCE for ternary $Ni_{50}Mn_{(50-x)}Sb_x$ (x = 13, 14, 15) alloys were studied by Du *et al.* and Chatterjee *et al.* later [36, 84]. The results revealed that a ΔS_m = 9.1 $J\cdot(kg\cdot K)^{-1}$ was detected in

$Ni_{50}Mn_{37}Sb_{13}$ alloy at 287 K with a 5 T magnetic field. Compared with the reported results by Khan *et al.* [47], such a ΔS_m is much lower thus this material could not be a promising magnetic refrigeration material.

Later, Feng *et al.* made a thorough investigation on MCE in the temperature regions of martensitic transformation and paramagnetism-ferromagnetism transition in austenite for $Ni_{(50-x)}Mn_{(38+x)}Sb_{12}$ (x = -1, 0, 1, 2) alloy system [72, 85]. The temperature dependences of entropy change are shown in **Fig. 1.7**. It can be seen that the entropy change of martensitic transformation possesses a positive value, while turns to negative for the paramagnetism-ferromagnetism transition in austenite. The ΔS_m reaches 21.9 $J\cdot(kg\cdot K)^{-1}$ at 279 K for $Ni_{49}Mn_{39}Sb_{12}$ with a 5 T magnetic field, which is the highest one among all the reported results in ternary NiMnSb alloys. In addition, for $Ni_{49}Mn_{39}Sb_{12}$ alloy, with a 1 T magnetic field, the ΔS_m also reaches 6.15 $J\cdot(kg\cdot K)^{-1}$ and with only 0.9 $J\cdot kg^{-1}$ hysteresis loss. Hence, this alloy demonstrates promising potential as room-temperature magnetic refrigeration material.

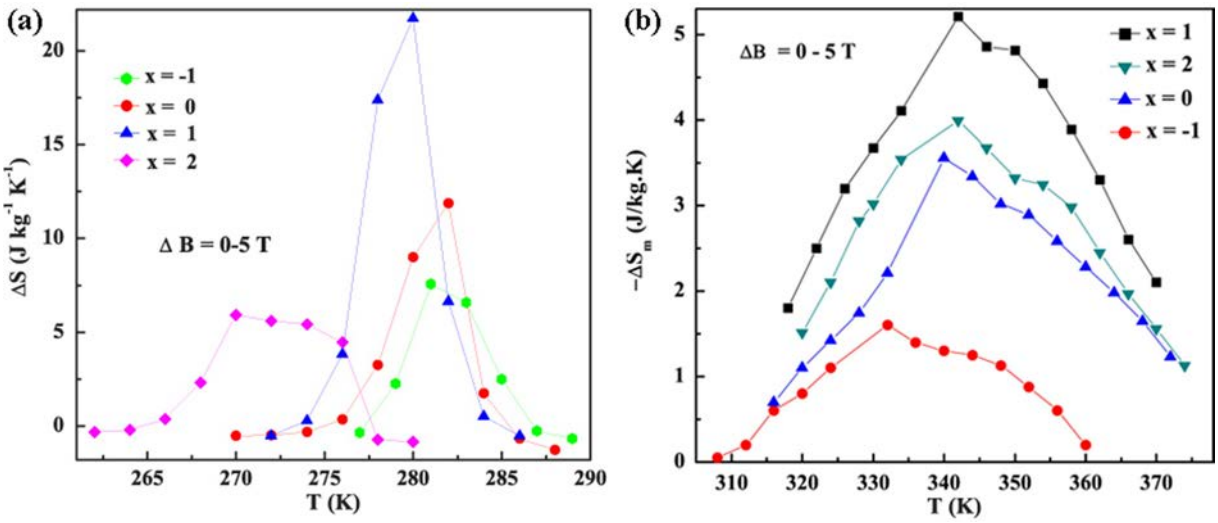

Fig. 1.7 Magnetic entropy changes in the temperature regions of (a) martensitic transformation [85] and (b) magnetic transition in austenite [72] for $Ni_{(50-x)}Mn_{(38+x)}Sb_{12}$ (x = -1, 0, 1, 2) alloys with a magnetic-field change from 0 to 5 T.

Although ternary NiMnSb polycrystalline alloys have an excellent MCE compared with NiMnIn and NiMnSn polycrystalline alloys [46, 86], the ΔS_m is still low. Alloying, as one of the most efficient way to enhance the ΔS_m, has been widely studied by researchers in recent years. Element doping using Cu [69], Fe [66], B [67], Co [74, 87] and so on to ternary NiMnSb

alloys are studied recently. All the results show that the ΔS_m have a certain increase compared with the parent ternary NiMnSb alloys, especially for Co doping.

Nayak *et al.* studied the MCE of forward [87] and reverse [74] martensitic transformation in NiCoMnSb alloys for the first time. The ΔS_m detected in a $Ni_{45}Co_5Mn_{38}Sb_{12}$ polycrystalline alloy with a 5 T magnetic field at ~ 260 K is 68 $J\cdot(kg\cdot K)^{-1}$. Compared with the one reported in the parent $Ni_{50}Mn_{38}Sb_{12}$ alloy (17.7 $J\cdot(kg\cdot K)^{-1}$ at 273 K with a 5 T magnetic field) [47], the value has been largely enhanced. In addition, the effective RC of this alloy is 74 $J\cdot kg^{-1}$, also much larger than the one observed before [47]. Since Co has a lager magnetic moment compared with the replaced Ni, Co doping is an efficient way to enhance the value of ΔS_m.

Effect of pressure on martensitic transformation and MCE for NiCoMnSb alloy was also studied by the group of Nayak *et al.* [88]. The results indicated that pressure can stabilize the martensitic state, *i.e.* increase the martensitic transformation start temperature. The martensitic transformation start temperature has increased by 28 K for $Ni_{45}Co_5Mn_{38}Sb_{12}$ under an 8.5 kbar pressure, while by 25 K for $Ni_{46}Co_4Mn_{38}Sb_{12}$ under a 9 kbar pressure. In addition, the pressure can also decrease the ΔS_m. For $Ni_{45}Co_5Mn_{38}Sb_{12}$ alloy, the ΔS_m increased first from 41.1 $J\cdot(kg\cdot K)^{-1}$ (without pressure) to 46 $J\cdot(kg\cdot K)^{-1}$ (with a 1.1 kbar pressure), and then decreased to 32.5 $J\cdot(kg\cdot K)^{-1}$ (with a 8.5 kbar pressure). For $Ni_{46}Co_4Mn_{38}Sb_{12}$, the ΔS_m decreased from 32.3 $J\cdot(kg\cdot K)^{-1}$ (without pressure) to 16.5 $J\cdot(kg\cdot K)^{-1}$ (with a 9 kbar pressure) continuously. The decrease in MCE can be attributed to the weakening of the martensitic transformation, which results in smaller difference in the magnetization between austenite and martensitic and causes a reduction in the $(\partial M/\partial T)_H$ value.

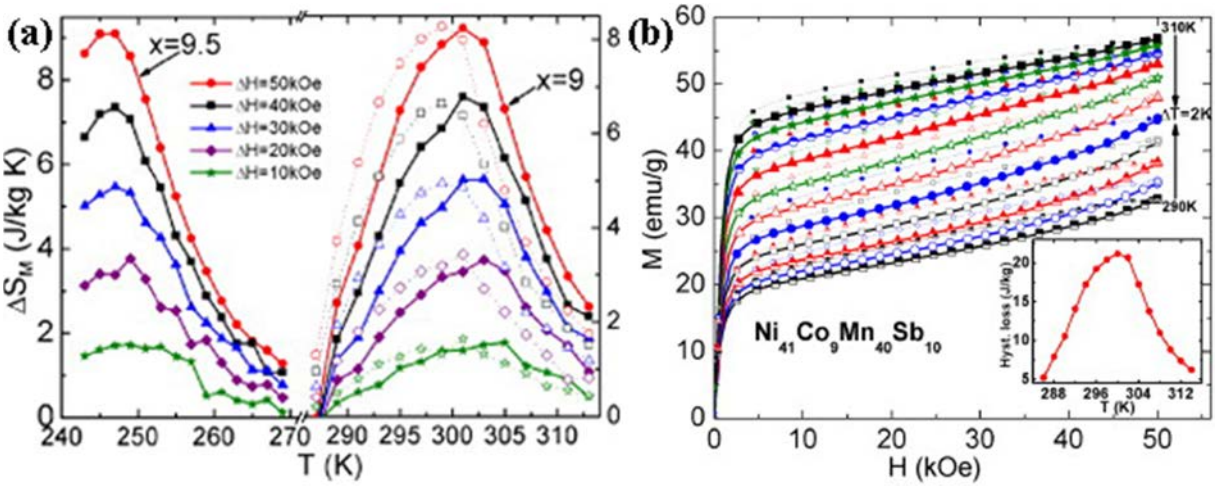

Fig. 1.8 (a) ΔS_m as a function of temperature in $Ni_{50-x}Co_xMn_{40}Sb_{10}$ (x = 9, 9.5); (b) isothermal magnetization curves and hysteresis losses around the martensitic transformation temperature for $Ni_{41}Co_9Mn_{40}Sb_{10}$ alloy [89].

Moreover, they also studied the MCE in $Ni_{50-x}Co_xMn_{40}Sb_{10}$ (x = 9, 9.5) alloy [89]. Although the ΔS_m is very small, 9.2 $J\cdot(kg\cdot K)^{-1}$ and 8.2 $J\cdot(kg\cdot K)^{-1}$ for x = 9 and 9.5 respectively, the MCE peak is quite broad, *i.e.* has an excellent RC, as shown in **Fig. 1.8**(a). In addition, the hysteresis loss is very low, as displayed in **Fig. 1.8**(b). Thus, a remarkable 106 $J\cdot kg^{-1}$ effective RC is finally obtained in $Ni_{41}Co_9Mn_{40}Sb_{10}$ alloy.

Based on the reported high ΔS_m in NiCoMnSb alloys system, Roshnee *et al.* and Sahoo *et al.* investigated the effect of Ga, Si [90] and Ge [81, 91] substitutions on the MCE, respectively. A ΔS_m of 70 $J\cdot(kg\cdot K)^{-1}$ was detected in the Si-doped alloy, $Ni_{46}Co_4Mn_{38}Sb_{11}Si_1$ alloy, at 273.5 K under a 5 T magnetic field. It is the highest entropy change that has been detected in NiMnSb-based polycrystalline bulk alloys, so far. For Ga and Ge substitutions, the ΔS_m is decreased compared with the corresponding parent alloy. However, a remarkable MCE peak broadening phenomenon was observed for Ga substitution, which is considered to be contributive to the RC in this alloy.

The MCE of NiMnSb alloys in other states like ribbon and thin films are also investigated. For an annealed $Ni_{46}Co_4Mn_{38}Sb_{12}$ ribbon, a ΔS_m = 32.5 $J\cdot(kg\cdot K)^{-1}$ was acquired [92], which has a 3.5 $J\cdot(kg\cdot K)^{-1}$ increase compared with the bulk sample that possesses the same composition [74]. A 23 $mJ\cdot(cm^3\cdot K)^{-1}$ and a 15.2 $mJ\cdot(cm^3\cdot K)^{-1}$ ΔS_m were detected in

$Ni_{49.8}Mn_{32.97}Al_{4.43}Sb_{12.8}$ [59] and $Ni_{50}Mn_{36.3}Sb_{10.4}Al_{3.3}$ [93] thin films, respectively. All these results have enriched the MCE investigations in NiMnSb alloys.

Although an excellent MCE and RC have been detected in NiMnSb alloys, there still exists deficiency with respect to the other types of NiMn-based Heusler alloys [94-97]. This mainly results from the relatively low ΔS_m, the narrow MCE peak and the high hysteresis loss in these materials. In addition, decreasing the high actuating magnetic field is also necessary, not only to reduce the cost but also to increase the practicability. Hence, property optimization is still needed for the practical applications of these alloys.

1.2.3.3 Exchange bias effect

Exchange bias effect was first discovered at the surface of a Co (core) – CoO (shell) clad material in 1956 [98]. This effect can be described as a shift of the hysteresis loop as displayed in **Fig. 1.9**. It can be seen that after the specimen is cooled under a magnetic field (the so-called field cooling) to a certain temperature, the hysteresis loop at this temperature shifts toward the negative magnetic field direction in the figure. The exchange bias field (H_{EB}) is defined by the shift of the hysteresis loop, as shown **Fig. 1.9**. For the specimen that is cooled without the magnetic field (the so-called zero field cooling), a double shifted loop [66] can be observed which indicates the existence of the antiferromagnetic region and the exchange bias effect in this material [66].

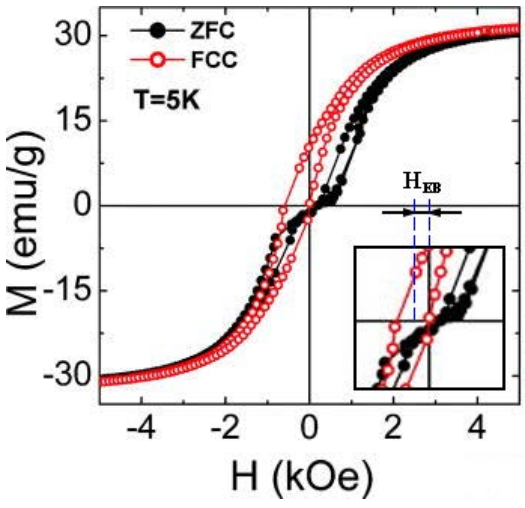

Fig. 1.9 Hysteresis loops at 5 K for $Ni_{50}Mn_{36}Fe_2Sb_{12}$ alloy after zero field cooling (ZFC) and field cooling (FCC). The definitions for the exchange bias field (H_{EB}) is indicated in the figure [66].

For a ferromagnetism and antiferromagnetism concomitant system, when it is cooled down from a temperature between Curie temperature and Néel temperature under a magnetic field to a temperature lower than Néel temperature, the exchange bias effect will occur. This effect is originated from a unidirectional magnetic anisotropy at the interface of the ferromagnetic and antiferromagnetic couplings. The pinning effect of the antiferromagnetic region to the adjacent ferromagnetic region is the origin of the hysteresis loop shift. Potential technological applications of the materials as permanent magnet materials and high density recording media can be achieved by this effect [99].

In NiMnSb alloys, the exchange bias effect was first studied by Khan *et al.* in 2007 [100]. The experiment was conducted in polycrystalline bulk $Ni_{50}Mn_{25+x}Sb_{25-x}$ ($12 \leq x \leq 13.5$) alloys. A maximum shift of the hysteresis loops, *i.e.* the H_{EB}, up to 248 Oe was detected in $Ni_{50}Mn_{38.5}Sb_{11.5}$ alloy at 5 K under a 5 T cooling field. Later, Rao *et al.* investigated the exchange bias effect in $Ni_{50}Mn_{50-x}Sb_x$ ($12 \leq x \leq 14$) alloys. A 230 Oe H_{EB} was obtained in $Ni_{50}Mn_{38}Sb_{12}$ alloy at 10 K under a 5 T cooling field, which is a little lower than the one reported in $Ni_{50}Mn_{38.5}Sb_{11.5}$ alloy. In 2012, Wang *et al.* studied the effect of temperature on H_{EB} in $Ni_{50}Mn_{36}Sb_{14}$ alloy [101]. With a 5 T cooling field, a 223 Oe H_{EB} was obtained at 5 K, then it rose to 413 Oe at 55 K, which is the highest H_{EB} that has been reported in ternary NiMnSb alloys, and finally dropped to 39 Oe at 95 K. In addition, they also carried out an investigation on the exchange bias effect through zero field cooling from different remanent states in this alloy [102] and obtained a maximum of 270 Oe H_{EB} with a 2.437 $emu \cdot g^{-1}$ remanence.

As a promising magnetic recording material, a high H_{EB} and a high blocking temperature are essential to the material. In order to obtain a higher H_{EB}, elements like Co [68, 103], Fe [66], Al [61, 63], Ge [63], Cr [50] *etc.* are doped into the ternary NiMnSb alloys. Results show that the doping of these elements can enhance the H_{EB} [50, 63, 66, 68]. Moreover, the doping of Al can also increase the blocking temperature of the alloy [63]. However, the maximum H_{EB} obtained was only 480 Oe, which was detected in a $Ni_{45}Mn_{38}Co_5Sb_{12}$ alloy at 3 K under a 5 T cooling field [68]. In 2011, Nayak *et al.* prepared powder $Ni_{50-x}Co_xMn_{38}Sb_{12}$ ($x = 0, 5$) alloys using the ball milling method. This time with a same cooling magnetic field and also at 3 K temperature, a huge H_{EB} up to 3200 Oe for $Ni_{50}Mn_{38}Sb_{12}$ alloy was detected, just as shown in

Fig. 1.10 [104], which is ~ 13 times larger than the one reported in bulk sample with the same composition.

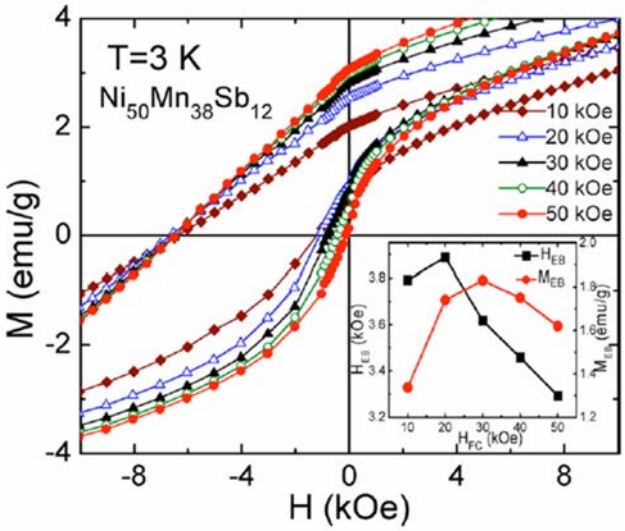

Fig. 1.10 Magnetization isotherms measured at 3 K after field cooling the sample in different fields. The inset shows the cooling field dependence of H_{EB} and exchage bias magnetization (M_{EB}) at 3 K [104].

To increase the blocking temperature, Akkera *et al.* prepared a NiMnSb (ferromagnetism) / CrN (anti-ferromagnetism) heterostructure deposited by magnetron sputtering which can even show the exchange bias effect at the Néel temperature of CrN (270 K) [64]. Although the maximum H_{EB} = 148 Oe was detected at 10 K temperature, a 10 Oe H_{EB} can still be detected at 295 K, which proposed a new approach to develop a room temperature NiMnSb based magnetic recording material.

Besides the bulk sample, the exchange bias effect in ribbon [62, 92] and thin films [54] of NiMnSb alloys were also investigated. The maximum H_{EB} = 610.83 Oe was obtained in a $Ni_{50}Mn_{36.3}Sb_{10.4}Al_{3.3}$ thin film at 10 K [54], a little higher than the bulk sample but also much lower than the one reported in the powder sample.

To summarize, a considerable H_{EB} has been acquired in NiMnSb alloys. However, the material possessing a high blocking temperature together with a high H_{EB} is still not found. As is known, in NiMnX (X = In, Sn, Sb) Heusler type alloys, all the Mn atoms on normal Mn sites have a ferromagnetic interaction, while the excess Mn atoms occupying the X sites are coupled through antiferromagnetic interaction to the surrounding Mn atoms. The antiferromagnetic

interaction between the Mn atoms will be enhanced with the decreasing of the distance between Mn atoms at X sites and the normal sites. Hence, a thorough investigation of the crystal and magnetic structures of these alloys is essential and of significance to understand the exchange bias effect and further investigations on property optimization.

1.2.3.4 Magnetoresistance effect

Magnetoresistance is a physical quantity to describe the variation of the electrical resistivity of a material under an external magnetic field. In NiMnX (X = In, Sn, Sb) alloy systems, during the martensitic transformation, the alloy will undergo a magnetostructural transformation from the high symmetry austenite to a low symmetry martensite, which results in the variation of the band structure. This may lead to a density change near the Fermi level and finally displays as a sharp electrical resistivity change near the martensitic transformation temperature [105] as shown in **Fig. 1.11**.

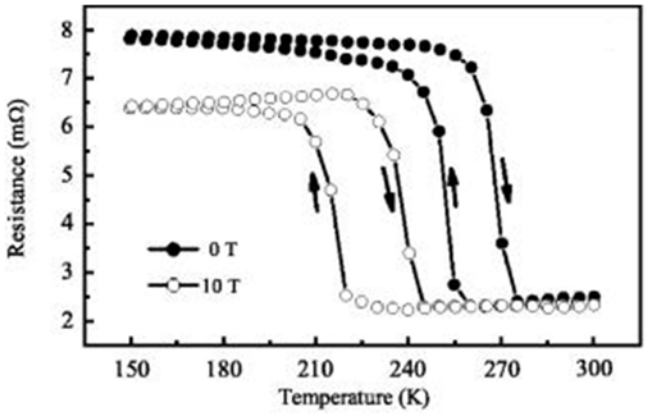

Fig. 1.11 Temperature variation of electrical resistivity for 0 and 10 T in $Ni_{41}Co_9Mn_{39}Sb_{11}$ alloy [106].

Moreover, the external magnetic field also can lead to an reverse martensitic transformation. Thus a considerable MR, as demonstrated in Eq. (1.4), can be acquired in the temperature region of martensitic transformation.

$$\text{Magnetoresistance} = \frac{\rho(H) - \rho(0)}{\rho(0)} \tag{1.4}$$

The magnetoresistance effect in NiMnSb alloy system was first studied in 2007 by Yu *et al.* [106]. An over 70 % recoverable magnetoresistance was detected in a $Ni_{41}Co_9Mn_{39}Sb_{11}$

polycrystalline bulk alloy between 230 ~ 250 K under a 13 T magnetic field. The discovery of such a large magnetoresistance in NiCoMnSb alloy attracted the attention of the researchers. Many approaches have been carried out later with an aim to increase the magnetoresistance value. Part of the reported magnetoresistance are listed in **Table 1.2**. However, the magnitude obtained by Yu *et al.* [106] has not been surpassed.

Table 1.2 Part of the reported magnetoresistance in NiMnSb alloy systems.

Composition	Reference	Magnetic field	Temperature	Magnetoresistance
$Ni_{41}Co_9Mn_{39}Sb_{11}$	[106] 2007	13 T	230 ~ 250 K	> 70 %
$Ni_{43}Co_7Mn_{38}Sb_{12}$	[87] 2010	5 T	~ 100 K	34 %
$Ni_{50}Mn_{37}Fe_1Sb_{12}$	[66] 2011	5 T	293 K	10 %
$Ni_{50}Mn_{36}Fe_2Sb_{12}$			289 K	21 %
$Ni_{50}Mn_{35}Fe_3Sb_{12}$			210 K	4 %
$Ni_{45}Co_5Mn_{38}Sb_{12}$	[81] 2012	5 T	~ 290 K	38 %
$Ni_{45}Co_5Mn_{38}Sb_{11}Ge_1$			~ 260 K	39 %
$Ni_{45}Co_5Mn_{38}Sb_9Ge_3$			~ 250 K	10 %
$Ni_{50}Mn_{36}Cr_1Sb_{13}$	[50] 2013	5 T	~ 320 K	~ 12 %
$Ni_{50}Mn_{37}Sb_{13}$ as-spun ribbon	[62] 2013	5 T	~ 225 K	4 %
$Ni_{50}Mn_{37}Sb_{13}$ annealed ribbon			~ 240 K	13 %
$Ni_{50}Mn_{37}Sb_{13}$ bulk			~ 270 K	20 %
$Ni_{46}Co_4Mn_{38}Sb_{12}$ as-spun ribbon	[92] 2013	5 T	295 K	10 %
$Ni_{46}Co_4Mn_{38}Sb_{12}$ as-spun ribbon			286 K	14 %
$Ni_{46}Co_4Mn_{38}Sb_{12}$ bulk			~ 290 K	28 %

It can be seen that, the magnetoresistance listed above were all obtained under a large magnetic field (≥ 5 T). Although the maximum magnetoresistance amounts to 70 %, the high external magnetic field is still an obstacle for practical applications. Hence, investigations on decreasing the external magnetic field and increasing the magnetoresistance of NiMnSb based alloys are still in need.

1.3 Martensitic transformation crystallography

1.3.1 Development of the martensitic transformation crystallography

Martensitic transformation is a solid to solid phase transformation, which can be observed in many materials, *e.g.* metals, alloys and ceramics [107]. During the transformation there is no diffusion or rearrangement of atoms. Hence, it is also called a displacive first-order phase transformation.

In SMAs (containing MSMAs), this transformation plays an important role in the thermomechanical and thermomagnetic properties of these alloys. During the martensitic transformation, the material always transforms from a high-temperature, high symmetry parent austenite phase to a low-temperature, low symmetry product martensite phase with an abrupt change of the crystal structure. Actually, there is a temperature interval in which the two phases can coexist. The misfit of the crystal lattice between the two phases will bring out the elastic strain. Hence, it is essential to reduce the strain during the nucleation and growth processes of martensitic transformation.

Martensitic transformation crystallography, as an important research field of martensitic transformation, can reveal the change of crystal structure and the physical mechanism of the phase transition.

In 1924, Bain proposed a phase transformation mechanism based on an investigation of the martensitic transformation from body-centered cubic austenite to body-centered tetragonal martensite in high-carbon steel [108]. This mechanism is based on condition of the minimum atomic displacements during phase transformation, which is called Bain distortion or Bain model nowadays. Although Bain distortion is not an invariant plane strain, it is still the fundamental of martensitic transformation crystallography.

In the early 1950s, researchers realized that the martensitic transformation is an invariant plane strain, which possesses an invariant (undistorted and not rotated) phase interface, *i.e.* the habit plane, together with a special orientation relationship (OR) between the two phases. With the help of matrix calculations and Bain model, two independent theories, W-L-R theory (proposed by Wechsler, Leiberman and Read in 1953 [109]) and B-M theory (proposed by

Bowles and Mackenzie in 1954 [110-113]) were proposed to describe the deformation of martensitic transformation, respectively, which formed the early phenomenological theories of martensitic transformation. Although the deformation were described differently in mathematics in the two theories, they are equivalent.

Later in 1987, with the consideration of elastic strain energy, the knowledge of nonlinear elasticity theory and continuum theory were combined with the phenomenological theories of martensitic transformation and finally generated the so-called nonlinear elasticity theory of martensitic transformation by Ball and James [109, 114]. One of the achievements of this theory is to predict/construct the microstructure of martensite just based on the lattice parameters of the two phases. In addition, with the help of crystallographic calculations, information like twin relationships between martensite variants, the twinning elements, the habit planes and OR between austenite and martensite and other interfaces in martensite can also be resolved by applying this theory.

1.3.2 Brief introduction of the nonlinear elasticity theory of martensitic transformation and microstructure construction

The content of this part are summarized based on the following references: [107, 114-123]. Before the introduction, some basic hypothesizes and theorems are needed to be clarified first. The first one is the Cauchy-Bron hypothesis [124]. This hypothesis says that with a given deformation gradient tensor *F*, any lattice vectors of the original state $\boldsymbol{r_o}$ will be transformed to a new lattice vector $\boldsymbol{r_d}$ of the deformed state, which can be described with the equation as below:

$$\boldsymbol{r_d} = F\boldsymbol{r_o}. \tag{1.5}$$

With this hypothesis, the atomic motion is associated with the macroscopic motion. The equation indicates that the deformation of martensitic transformation is considered to be linear and homogeneous.

The second one is the kinematic compatibility condition. Actually, this theory indicated that the construction of the microstructure in martensite phase is based on a minimization of the energy. As we all know, the interfaces between two different oriented regions can be coherent, semi-coherent and incoherent. Among these three types, the coherent interface obviously has

the minimum interfacial energy. Hence, when a body is deformed differently along each side of a plane, as illustrated in **Fig. 1.12**, this plane could be a coherent interface after the deformation if and only if the two given deformation gradients, *F* and *G*, satisfy the following condition:

$$F - G = \boldsymbol{a} \otimes \boldsymbol{n}. \tag{1.6}$$

Here, ***a*** represents a vector on the plane and ***n*** is the normal vector of the plane.

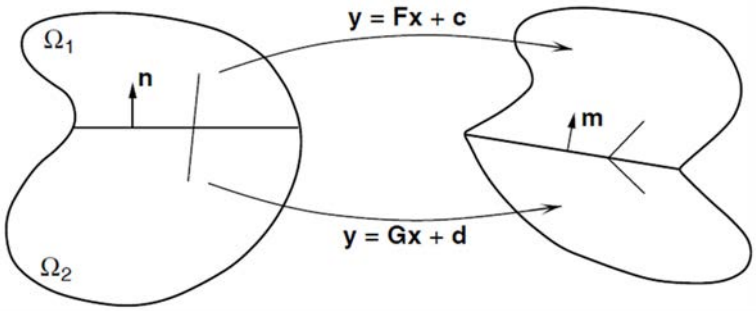

Fig. 1.12 Illustration of the kinematic compatibility condition. *F* and *G* are two deformation gradients of the two regions Ω_1 and Ω_2 which are separated by a plane with normal vector ***n*** (transformed to ***m*** after the deformation) [107].

The third one is the description of the martensitic transformation deformation. In this theory, the deformation of martensitic transformation *F* is considered to be composed of two parts: a first pure stretch distortion *U* and a subsequent pure rigid rotation *R*. Hence, the deformation gradient can be expressed as below:

$$F = RU. \tag{1.7}$$

It is worth mentioning that the pure stretch distortion *U* represents the Bain distortion. Hence, the rotation *R* is imperative to keep an invariant plane strain and a minimization of the energy during the phase transformation.

The last one is the polar decomposition theorem. This is a mathematic theorem describes that for a given positive definite matrix *L*, there exists a unitary matrix *M* and a Hermitian matrix *N* such that

$$L = MN. \tag{1.8}$$

In physics, the positive definite matrix, unitary matrix and Hermitian matrix can be used to describe deformation, extension and rotation. Hence, for any deformation, it can be

decomposed to a pure stretch distortion and a pure rotation. Hence, Eqs. (1.7) and (1.8) are equivalent.

In the study of martensitic transformation and the transformed microstructures, three typical types of martensite named wedge-shaped, triangle-shaped and diamond-shaped can be generated at the beginning stage of the phase transformation, as illustrated in **Figs. 1.13**(a) ~ (c). According to the introduction of the theory, the habit planes between austenite and martensite as well as the interfaces between different martensite variants should be coherent, to minimize the interfacial energy. However, this situation is sensitive to the lattice parameters of the parent and product phases. Hence, more complicated microstructures such as a twin within a twin [107] (as displayed in **Figs. 1.13**(d) and (f)) and a twin within a twin within a twin [118] (as displayed in **Fig. 1.13**(e)) were found in some alloys. Generally, the lattice parameters of the two phases cannot make all the observed interfaces coherent. Therefore, the atoms in the vicinity of some interfaces between martensite variants will have a small mismatch, *i.e.* an incoherent interface as marked in **Fig. 1.13**(f), to keep a coherent habit plane.

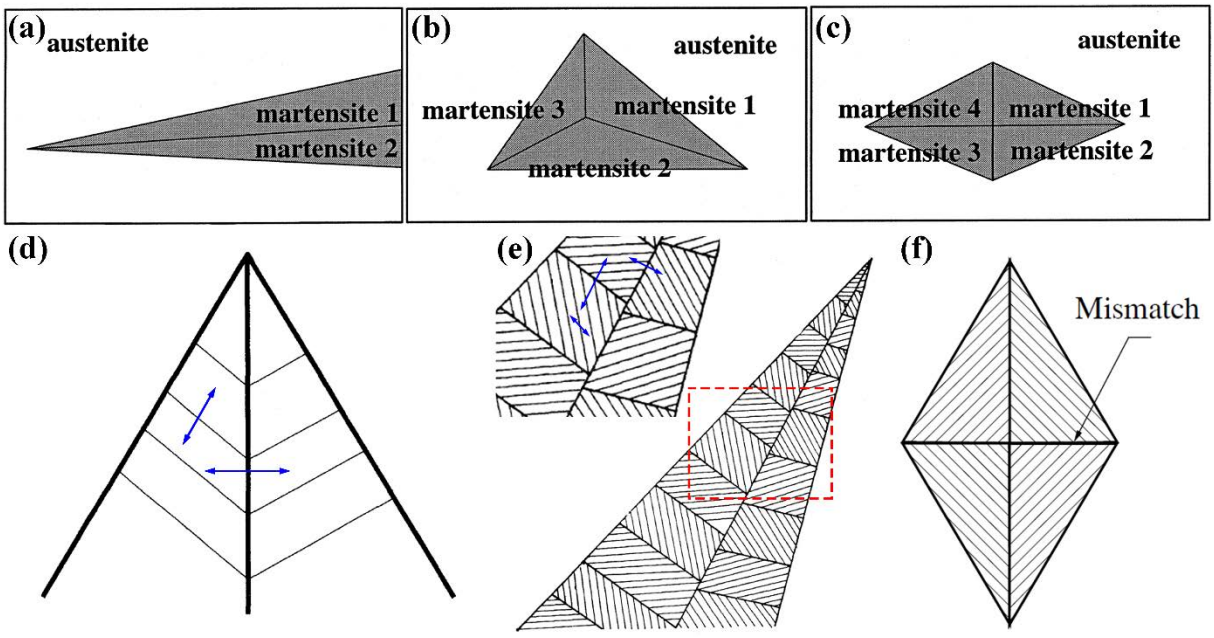

Fig. 1.13 Illustrations of different shaped martensite that forms at the beginning stage of the martensitic transformation: (a) wedge-shaped, (b) triangle-shaped, (c) diamond-shaped, (d) and (e) wedge-shaped with fine lamellae twins and (f) diamond-shaped with fine lamellae twins [107, 118-120]. The twin related variants in **Figs. 1.13**(d) and (e) are marked with blue arrows.

Thus, with these tools the microstructure construction work can be effectuated. During the construction process, the first step is to calculate the deformation gradient of Bain distortion and add a rotation to judge if a single variant can satisfy an invariant plane strain, *i.e.* can obtain a coherent phase interface with the austenite with the help of the kinematic compatibility condition. If it could, then investigations on the compatibility of the interfaces between different variants with the given models can be continued. If not, more complicated microstructures and calculations should be taken into account and carried out. Compatibilities on the interfaces of different variant combinations, and between different variant combinations and the parent austenite are needed to be considered.

As summarized, the crystal structure information is a decisive factor to the morphology of martensite. The organization of the phases and martensite variants, characterizations of different interfaces between martensite variants, deformation gradient tensors of different martensite variants and even their ORs all can be resolved with the help of the nonlinear elasticity theory [125] of martensitic transformation and the lattice parameters of the corresponding phases. In addition, the phase transition path, volume distortion and the misfit between the two phases which can affect the phase transition resistance can also be studied with this theory. For NiMnSb alloys, the magnetic properties are closely associated with the martensitic transformation. The practical applications of these properties require repeated phase transitions of materials. A high phase transition resistance will be disadvantageous to their applications. Hence, a thorough investigation through crystallographic analysis of the microstructural configuration in NiMnSb alloys is essential, which can provide fundamental information of these materials and be useful for further compositional regulation and control and the subsequent magnetic and mechanical properties optimization of these materials.

1.4 Content of the present work

As a novel multi-functional material, many aspects of the Heusler type NiMnSb alloys, such as crystal structure, microstructure, magnetic properties and mechanical properties *etc.*, have been widely investigated in the past thirteen years. However, many fundamental issues of this material have not been fully revealed, which largely restricts the development of this new

kind of multi-functional materials. For example, the crystal structure of martensite, as the basis information of the material is still controversial. Due to the lack of the accurate crystal structure information, further crystallographic orientation analyses have not yet been carried out with the electron backscatter diffraction (EBSD) technique. In addition, the microstructural and crystallographic features of martensite, which plays an important role in the consequent magnetic properties have not been reported until now. Hence, the related investigations are in great need and of significance.

Based on such a background, the present work was oriented to carry out a thorough investigation on microstructural and crystallographic features of martensite phase, and the martensitic transformation mechanism in ternary NiMnSb alloys. The main contents of this work can be summarized as below:

(1) Crystal structure determination and crystallographic features characterization of $Ni_{50}Mn_{38}Sb_{12}$ martensite by means of XRD diffraction and SEM EBSD techniques. (Chapter 4)

(2) Study on martensitic transformation OR and martensite variant organization in $Ni_{50}Mn_{38}Sb_{12}$ alloy by means of SEM EBSD technique. (Chapter 5)

(3) Investigation on martensitic transformation strain characters in $Ni_{50}Mn_{37}Sb_{13}$ alloy and its impact on microstructural organizations by means of EBSD technique and crystallographic theory of martensitic transformation. (Chapter 6)

This work aims at resolving the crystal structure of NiMnSb martensite, enriching the microstructure information and providing fundamental information on crystallographic features in martensite, martensitic transformation OR, martensite variants organization and martensitic transformation mechanism for the understanding of the multi properties and further property optimization of NiMnSb alloys.

Chapter 2 Materials and experiments

2.1 Materials preparations and heat treatments

Fig. 2.1 shows the process of the sample preparations consisting of arc melting, spray casting and heat treatments. In the present work, polycrystalline alloys with nominal compositions of $Ni_{50}Mn_{38}Sb_{12}$ (at.%) and $Ni_{50}Mn_{37}Sb_{13}$ (at.%) were prepared by arc melting high-purity elements Ni (99.99 wt.%), Mn (99.8 wt.%) and Sb (99.995 wt.%). During this process, 2 % (wt%) extra Mn and 2 % (wt%) extra Sb were added to compensate for their weight losses. The ingot was re-melted 4 times to ensure compositional homogeneity. The prepared ingot was then spray cast into a copper mould in order to obtain a dense bulk cylindrical sample. To avoid compositional inhomogeneity, annealing was applied before and after the spray casting at 1173 K for 24 h, followed by water quenching. The arc melting, spray casting and heat treatments were carried out under an argon atmosphere.

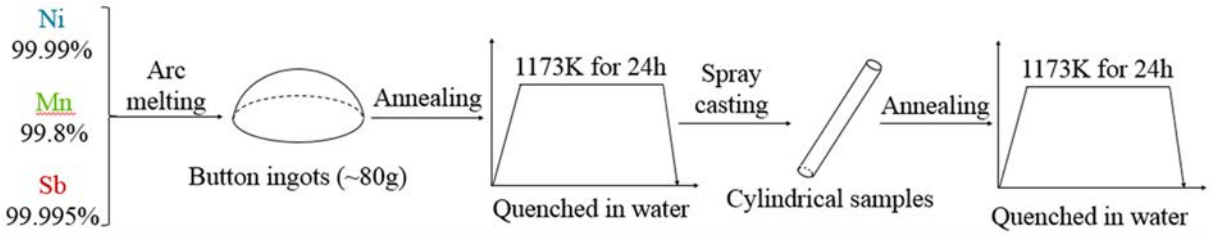

Fig. 2.1 Illustration of the sample preparation process.

Bulk samples with a size of 4 × 6 × 10 mm were prepared by electrical-discharge wire cutting from the annealed cylinder. A powder sample was ground from the bulk alloy with a particle size smaller than 74 μm. In order to release the stress produced by the grinding, the powder sample was annealed at 873 K for 5 h in a sealed vacuum quartz tube.

2.2 Experimental details

2.2.1 Forward and reverse martensitic transformation temperature measurements

The forward and reverse martensitic transformation temperatures were determined by differential scanning calorimetry (DSC) (TA Instruments Q100). During the measurement, powder samples (~ 20 mg) were used. The heating/cooling rate was 10 $K \cdot min^{-1}$ within the temperature range 183 K ~ 473 K. The measurement was carried out under a nitrogen atmosphere to avoid the sample from oxidation.

2.2.2 Determination of crystal structures

The powder diffraction patterns were measured using XRD (Rigaku, Smartlab) with a 9 kW rotating anode using Cu $K\alpha$ (λ = 1.540598 Å) radiation and a graphite monochromator. For $Ni_{50}Mn_{38}Sb_{12}$ alloy, the experiment was carried out at room temperature. For $Ni_{50}Mn_{37}Sb_{13}$ alloy, two patterns were acquired at 213 K and 333 K, respectively. The cooling/heating rate was 10 $K \cdot min^{-1}$ and before the measurements, the sample was held at the set temperatures for 15 minutes. The measurements were conducted under the protection of nitrogen atmosphere. The 'step' mode was used with a scanning step of 0.02° (2θ) to obtain high-resolution patterns.

2.2.3 Microstructural and crystallographic characterizations

The microstructural and crystallographic features were characterized on the bulk samples. The samples were mechanically ground with SiC papers and electrolytic polished using a solution of 20 % (in volume) nitric acid and 80 % (in volume) methanol. The electrolytic polishing was conducted at 273 K and 297 K under a continuous multistep mode: 8 V for 10 s, 15 V for 5 s and 18 V for 3 s, for $Ni_{50}Mn_{38}Sb_{12}$ and $Ni_{50}Mn_{37}Sb_{13}$ alloys, respectively. The microstructural characterizations were performed using a field emission gun SEM (JEOL JSM 6500F). The crystallographic characterizations were conducted using the same SEM equipped with an EBSD acquisition camera (Oxford) and the *AZTEC* online acquisition software (Oxford Instruments). Two modes, manual and automatic, were used in orientation acquisition. To ensure the certainty of the measurement, the sample was rotated to make the length directions of the fine lamellar microstructural constituents parallel to the elongation direction of the electron beam for both modes, as the sample was tilted for EBSD measurements.

Chapter 3 Basic crystallographic calculations

3.1 Coordinate system setting, Euler angle and orientation matrix

Three Cartesian coordinate systems were used in the crystallographic calculations in the present PhD work in addition to the Bravais lattice basis of the cubic austenite and the orthorhombic martensite. One, *i.e.* '*x*-*y*-*z*', is set to the sample, and the other two to the Bravais lattice of the corresponding phase, *i.e.* the cubic austenite lattice and the orthorhombic martensite lattice. The former is termed as sample coordinate system and the latter Cartesian crystal coordinate system. The relation between the Cartesian crystal coordinate system and the Bravais lattice basis conforms to the convention described in the *Channel 5* software package, as illustrated in **Fig. 3.1**.

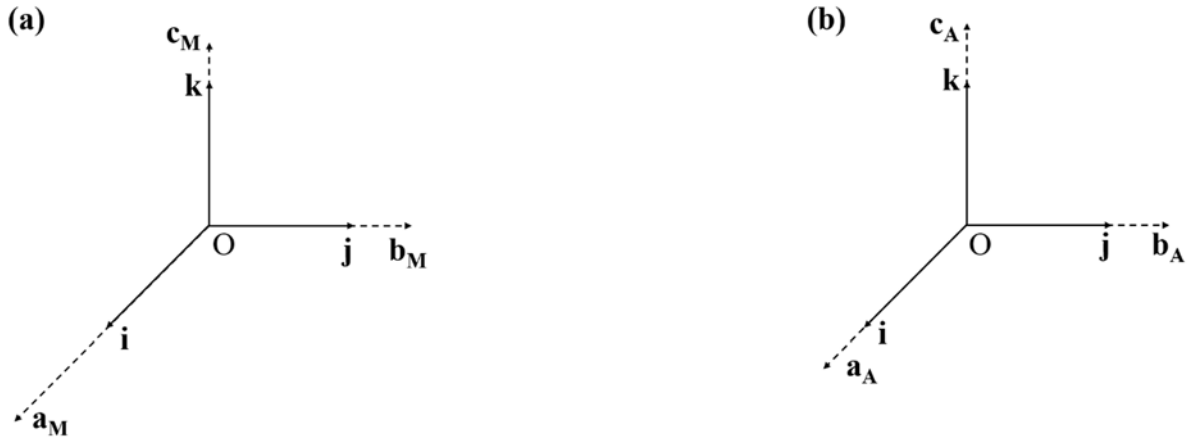

Fig. 3.1 Relationship between the Cartesian crystal coordinate system '*i*-*j*-*k*' and (a) the Bravais lattice basis of the orthorhombic martensite 'a_M-b_M-c_M' and (b) the Bravais lattice basis of the cubic austenite 'a_A-b_A-c_A'.

Under the *Channel 5* (Oxford Instruments) convention, the three basis vectors of the Bravais lattice basis $\boldsymbol{a_M}$, $\boldsymbol{b_M}$ and $\boldsymbol{c_M}$ or $\boldsymbol{a_A}$, $\boldsymbol{b_A}$ and $\boldsymbol{c_A}$ are parallel to the respective basis vectors $\boldsymbol{i}$, $\boldsymbol{j}$ and $\boldsymbol{k}$ of the Cartesian crystal coordinate system '*i*-*j*-*k*'. If we define the lengths of the three basis vectors of the Bravais lattices a_M, b_M and c_M for martensite and a_A, b_A and c_A ($a_A = b_A = c_A$) for austenite, the corresponding coordinate transformation matrices from the '*i*-*j*-*k*' frame to the crystal coordinate systems can be written as:

$$G_{EM} = \begin{pmatrix} a_M & 0 & 0 \\ 0 & b_M & 0 \\ 0 & 0 & c_M \end{pmatrix} \tag{3.1}$$

$$G_{EA} = \begin{pmatrix} a_A & 0 & 0 \\ 0 & b_A & 0 \\ 0 & 0 & c_A \end{pmatrix} \tag{3.2}$$

As is known, in a polycrystalline material there exists large amount of differently oriented crystals. In order to describe the orientation of the crystals, the concept of a triplet rotations represented in Euler angles is usually used. In the present work, the Euler angles (φ_1 Φ φ_2) under Bunge notation [126, 127] is adopted. The definition of the three rotations φ_1, Φ and φ_2 are illustrated in **Fig. 3.2**, where the '*x*-*y*-*z*' represents the sample coordinate system. Thus, the crystal coordinate system is associated with the sample coordinate system with the Euler angles. The rotation matrix R_{SE} (it should be mentioned that all the coordinate transformation matrices and rotation matrices used in the thesis for crystallographic calculations are expressed in matrix notation) from the sample coordinate system to the Cartesian crystal coordinate system can be described as:

$$R_{SE} = \begin{pmatrix} \cos\varphi_1\cos\varphi_2 - \sin\varphi_1\sin\varphi_2\cos\Phi & -\cos\varphi_1\sin\varphi_2 - \sin\varphi_1\cos\varphi_2\cos\Phi & \sin\varphi_1\sin\Phi \\ \sin\varphi_1\cos\varphi_2 + \cos\varphi_1\sin\varphi_2\cos\Phi & -\sin\varphi_1\sin\varphi_2 + \cos\varphi_1\cos\varphi_2\cos\Phi & -\cos\varphi_1\sin\Phi \\ \sin\varphi_2\sin\Phi & \cos\varphi_2\sin\Phi & -\cos\Phi \end{pmatrix}. \tag{3.3}$$

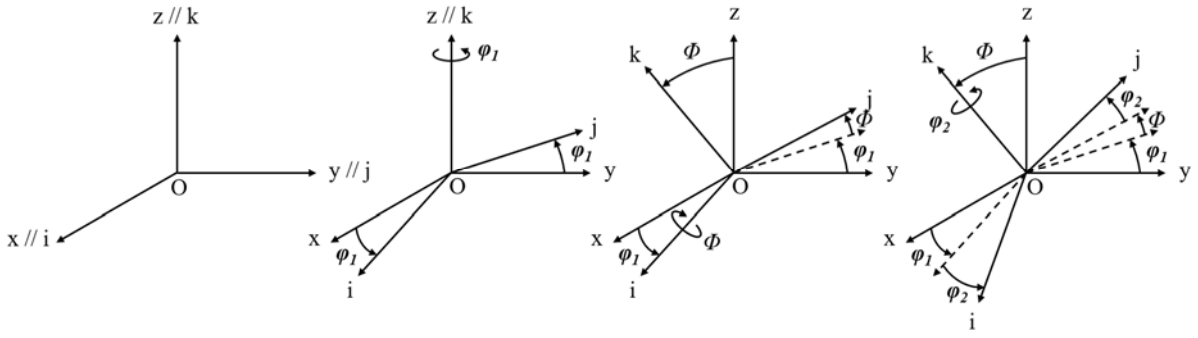

Fig. 3.2 Illustration of the three rotations in Bunge notation. '*x*-*y*-*z*': sample coordination system; '*i*-*j*-*k*': the Cartesian crystal coordinate system.

3.2 Stereographic projection

The stereographic projection is a two-dimensional (2D) map to represent the projection of a vector (or a plane normal) to the equatorial plane of the sphere, as illustrated in **Fig. 3.3**.

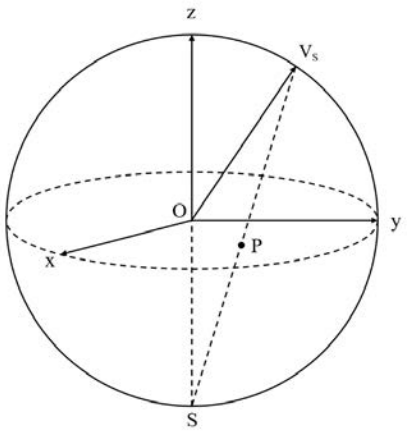

Fig. 3.3 Illustration of stereographic projection on the equatorial plane *xOy* of vector $\boldsymbol{OV_S}$. Point *P* is the projection pole of vector $\boldsymbol{OV_S}$ on the equatorial plane and point *S* is the south pole of the projection sphere.

To calculate the projection of a crystalline direction, this direction should be expressed under the coordinate system of the projection, for example the sample coordinate frame, with the following equation:

$$\boldsymbol{V_S}=R_{SE} \times S_i \times G_{EC} \times \begin{pmatrix} u \\ v \\ w \end{pmatrix}. \tag{3.4}$$

Here, R_{SE} is the rotation matrix from the sample coordinate system to the Cartesian crystal coordinate system, S_i is the rotational symmetry matrices of the crystal system, G_{EC} is the coordinate transformation matrix from the Cartesian crystal coordinate system to the Bravais lattice basis and [*uvw*] is the Miller indices of the crystalline direction.

Suppose that the coordinates of vector $\boldsymbol{V_S}$ in the sample coordinate system are [xV_S yV_S zV_S], the radius of the projection sphere *R* should be:

$$R = (xV_S^2 + yV_S^2 + zV_S^2)^{1/2}. \tag{3.5}$$

If $zV_S \geq 0$, the equation of line V_SS can be expressed as:

$$\frac{x}{xV_S} = \frac{y}{yV_S} = \frac{z+R}{zV_S+R}. \tag{3.6}$$

Let *z=0*, the abscissa *x* and ordinate *y* of point *P* can be obtained. After normalization, the abscissa and ordinate values of the stereographic projection of the vector are:

$$\begin{aligned} x &= \frac{xV_S}{zV_S+R} \\ y &= \frac{yV_S}{zV_S+R}. \end{aligned} \tag{3.7}$$

To plot the projection of a crystalline plane (*hkl*), the normal vector $\boldsymbol{n}$ should be calculated first with the following equation:

$$\boldsymbol{n} = g^* \times \begin{pmatrix} h \\ k \\ l \end{pmatrix}, \tag{3.8}$$

where g^* is the reciprocal metric tensor of the corresponding crystal:

$$g^* = \begin{pmatrix} \boldsymbol{a}^* \cdot \boldsymbol{a}^* & \boldsymbol{a}^* \cdot \boldsymbol{b}^* & \boldsymbol{a}^* \cdot \boldsymbol{c}^* \\ \boldsymbol{b}^* \cdot \boldsymbol{a}^* & \boldsymbol{b}^* \cdot \boldsymbol{b}^* & \boldsymbol{b}^* \cdot \boldsymbol{c}^* \\ \boldsymbol{c}^* \cdot \boldsymbol{a}^* & \boldsymbol{c}^* \cdot \boldsymbol{b}^* & \boldsymbol{c}^* \cdot \boldsymbol{c}^* \end{pmatrix}. \tag{3.9}$$

Here, $\boldsymbol{a}^*$, $\boldsymbol{b}^*$, $\boldsymbol{c}^*$ are the three basis vectors of the reciprocal space of the crystal. Then repeat the procedures using Eqs. (3.4) ~ (3.7), the stereographic projection of a given plane can be obtained.

3.3 Mean orientation

Since the crystal is hardly perfect, *i.e.* there exists misorientation at different regions of one crystal, the mean orientation of the crystal is used to represent the orientation of the crystal for crystallographic calculations. The algorithm mentioned below is summarized from reference [128].

To calculate the mean orientation, a four-dimensional orientation vector $\boldsymbol{O}$ is defined:

$$\boldsymbol{O} = [o_1 \quad o_2 \quad o_3 \quad o_4], \tag{3.10}$$

where

$$\begin{aligned} o_1 &= -\cos\frac{\Phi}{2}\cos\frac{\varphi_1+\varphi_2}{2} \\ o_2 &= -\sin\frac{\Phi}{2}\cos\frac{\varphi_1-\varphi_2}{2} \\ o_3 &= -\sin\frac{\Phi}{2}\sin\frac{\varphi_1-\varphi_2}{2} \\ o_4 &= -\cos\frac{\Phi}{2}\sin\frac{\varphi_1+\varphi_2}{2} \end{aligned} \tag{3.11}$$

and (φ_1 Φ φ_2) are the measured Euler angles. Thus, the mean orientation vector $\bar{\boldsymbol{O}}$ that corresponds to the mean orientation of a group of Euler angles can be calculated with the equation below:

$$\bar{\boldsymbol{O}} = \sum_{i=1}^{n} \boldsymbol{O}_i \Big/ \sum_{i=1}^{n} |\boldsymbol{O}_i|, \tag{3.12}$$

where

$$|\boldsymbol{O_i}| = \sqrt{o_1^2 + o_2^2 + o_3^2 + o_4^2} \tag{3.13}$$

and *n* is the total number of the sets of measured Euler angles. Thus, according to the definition of vector ***O*** shown in Eqs. (3.10) and (3.11), the mean Euler angles $\left(\overline{\varphi_1}\ \overline{\Phi}\ \overline{\varphi_2}\right)$ can be calculated from the mean orientation vector $\overline{\boldsymbol{O}}$.

3.4 Misorientation

Generally, the misorientation between two crystals can be expressed in angle/axis pair — (ω, ***d***), which describes a rotation from one symmetrically equivalent Cartesian crystal coordinate system of one crystal to one symmetrically equivalent Cartesian crystal coordinate system of the other crystal.

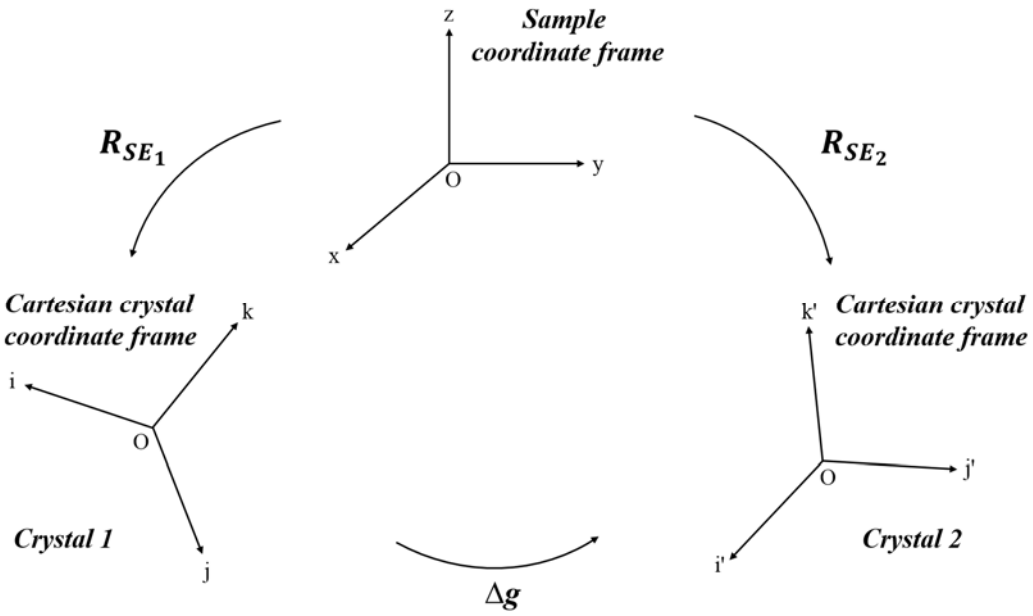

Fig. 3.4 Schematic of misorientation between two crystals. '*x*-*y*-*z*' is the sample coordinate system. '*i*-*j*-*k*' and '*i'*-*j'*-*k'*' are the Cartesian crystal coordinate systems. R_{SE_1} and R_{SE_2} are rotation matrices from the sample coordinate system to the Cartesian coordinate systems of the two crystals. Δg is the misorientation matrix between the two crystals.

To determine the (ω, ***d***), the misorientation matrix Δg between the two crystals should be calculated first, as illustrated in **Fig. 3.4**:

$$\Delta g = \left(S_1^i\right)^{-1} \times \left(R_{SE_1}\right)^{-1} \times R_{SE_2} \times S_2^j, \tag{3.14}$$

where S_1^i and S_2^j represent the rotational symmetric matrices of crystal 1 and crystal 2, R_{SE_1} and R_{SE_2} represent the rotation matrices from the sample coordinate system to the corresponding Cartesian crystal coordinate systems of crystal 1 and crystal 2 that are obtained by experiments. Denote the misorientation matrix Δg as below:

$$\Delta g = \begin{pmatrix} g_{11} & g_{12} & g_{13} \\ g_{21} & g_{22} & g_{23} \\ g_{31} & g_{32} & g_{33} \end{pmatrix}. \tag{3.15}$$

The misorientation angle ω and the rotation axis $\boldsymbol{d}$ $[d_1 d_2 d_3]$ expressed in the Cartesian crystal coordinate system can be calculated:

$$\omega = arc\,cos\left(\frac{g_{11} + g_{22} + g_{33} - 1}{2}\right), \tag{3.16}$$

(1) $\omega = 0°$

$$\boldsymbol{d} = [d_1 \quad d_2 \quad d_3] = [1 \quad 0 \quad 0]; \tag{3.17}$$

(2) $0° < \omega < 180°$

$$\boldsymbol{d} = [d_1 \quad d_2 \quad d_3] = \left[\frac{g_{23} - g_{23}}{2\,sin\,\omega} \quad \frac{g_{31} - g_{13}}{2\,sin\,\omega} \quad \frac{g_{12} - g_{21}}{2\,sin\,\omega}\right]; \tag{3.18}$$

(3) $\omega = 180°$

$$\begin{gathered} \boldsymbol{d} = [d_1 \quad d_2 \quad d_3] = [\pm\sqrt{\frac{g_{11} + 1}{2}} \quad \pm\sqrt{\frac{g_{22} + 1}{2}} \quad \pm\sqrt{\frac{g_{33} + 1}{2}}] \\ with \begin{pmatrix} |d_m| = max(|d_i|, i = 1,2,3) \\ d_m > 0 \\ \forall\, i \neq m, d_i = sign(g_{im}) \cdot |d_i| \end{pmatrix}. \end{gathered} \tag{3.19}$$

Due to the existence of the crystallographic rotational symmetry, the misorientation matrix between two crystals is not unique (except that the two crystals are both triclinic), but all the calculated (ω, $\boldsymbol{d}$) are crystallographically equivalent.

3.5 Twin relationship and twinning elements

According to the definition of twin, two twin related crystals should possess at least one 180° misorientation angle ω. If the corresponding rotation axis $\boldsymbol{d}$ is the normal vector of a rational crystalline plane, the two crystals are type I twin. Among the twinning elements (K_1 -

the twinning plane, $\boldsymbol{\eta_1}$ - the twinning direction, K_2 - the conjugate twinning plane, $\boldsymbol{\eta_2}$ - the conjugate twinning direction, P - the plane of shear and γ - the magnitude of shear), only the Miller indices of the twinning plane K_1 and the conjugate twinning direction $\boldsymbol{\eta_2}$ are rational. If the corresponding rotation axis $\boldsymbol{d}$ is a rational crystalline direction, the two crystals are type II twin and the Miller indices of the twinning direction $\boldsymbol{\eta_1}$ and the conjugate twinning plane K_2 are rational. If the two crystals possess two 180° misorientation angles and the corresponding rotation axes are perpendicular, the two crystals are compound twin and all the Miller indices of the twinning elements are rational.

To determine all the twinning elements, the twin relationship between the two crystals should be first determined by experiments. Then with the known K_1 indices (for type I or compound twin) or $\boldsymbol{\eta_1}$ direction (for type II twin), all the twinning elements can be resolved using the method proposed in reference [129].

This method is based on the minimum shear operation that transforms the lattice points of a crystal into their counterpart twin positions. **Fig. 3.5** is the schematic of the twinning direction and twinning shear determination for type I (or compound) twin.

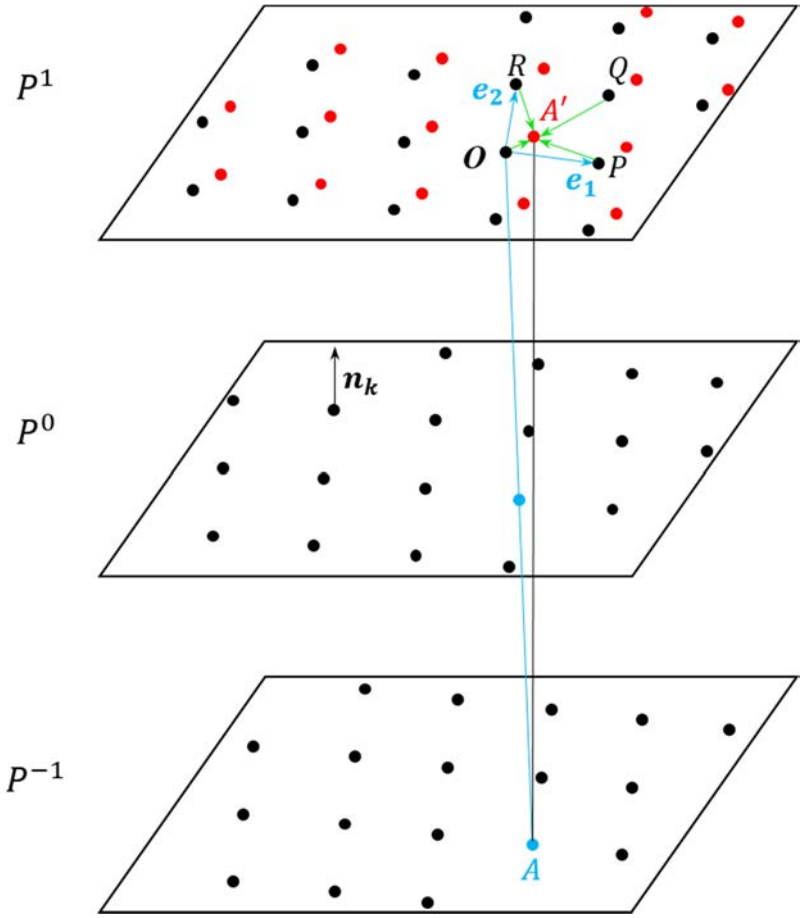

Fig. 3.5 Schematic of the twinning element determination for type I (or compound) twin.

P^0 is the twinning plane that separates the twin lattice (the upper part) from the parent lattice (the lower part). P^1 and P^{-1} are two nearest neighboring crystalline planes that parallel to the twinning plane. The black points are the initial lattice points, while the red points in plane P^1 are the twin lattice points. $\boldsymbol{e_1}$ and $\boldsymbol{e_2}$ are two reduced basis vectors of the twinning plane that possesses the shortest moduli and are the most orthogonal to each other. For a point A' of the twin lattice in P^1 plane, its initial lattice point in the parent lattice maybe one of the 4 points *O*, *P*, *Q* and *R*. Based on the minimum shear criterion, the 4 vectors $\boldsymbol{OA'}$, $\boldsymbol{PA'}$ $\boldsymbol{QA'}$ and $\boldsymbol{RA'}$ which possesses the minimum moduli should be the twinning direction $\boldsymbol{\eta_1}$. Denote this vector as $\boldsymbol{s}$ and the interplanar spacing of K_1 plane as d_{K_1}, the magnitude of shear is given by:

$$\gamma = |\boldsymbol{s}|/d_{K_1}. \tag{3.20}$$

For other twinning elements, we can calculate according to the geometric relationship between them as illustrated in **Fig. 3.6**. The resolved twinning elements have been marked in red.

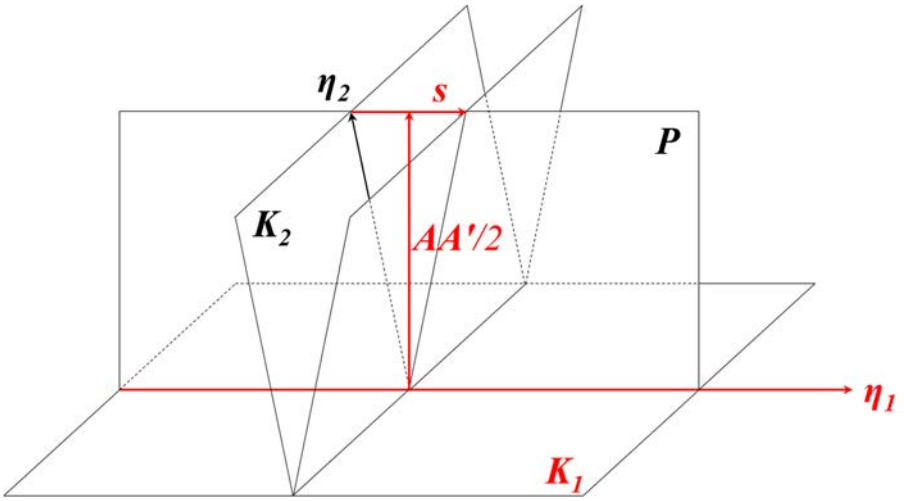

Fig. 3.6 Geometric relationship between different twinning elements.

The conjugate twinning direction $\boldsymbol{\eta_2}$ can be obtained such that

$$\boldsymbol{\eta_2} = \boldsymbol{AA'}/2 - \boldsymbol{s}/2. \tag{3.21}$$

The normal of plane of shear *P* can be calculated by the vector cross product of $\boldsymbol{\eta_1}$ and $\boldsymbol{\eta_2}$. The normal of the conjugate twinning plane K_2 is the vector cross product of the normal of plane *P* and vector $\boldsymbol{\eta_2}$. Hereto, all the 6 twinning elements in type I (or compound) twin are resolved.

As is known a vector in the direct space corresponds to a plane normal to it in the corresponding reciprocal space and a plane in the direct space corresponds to a vector normal to it in the corresponding reciprocal space. Hence, the twinning elements for a type II twin in the direct space is equivalent to the twinning elements for a type I twin in the corresponding reciprocal space. With the measured EBSD data, a rational twinning direction $\boldsymbol{\eta_1}$ for a type II twin can be determined, *i.e.* the K_1 plane of the corresponding type I twin in the reciprocal space. Hence, the determination of the twinning elements for a type II twin can be resolved with the same procedure mentioned above for type I but in the reciprocal space.

3.6 Trace analysis method

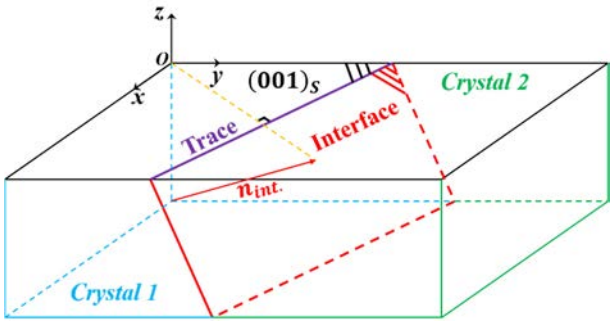

Fig. 3.7 Schematic of trace analysis method.

During the crystallographic characterization and identification processes, the trace analysis method can be used to characterize the interfaces. **Fig. 3.7** is the schematic of this method. '*x*-*y*-*z*' is the sample coordinate frame. The *xOy* plane marked in black, *i.e.* the $(001)_S$ plane, is the observation and measurement plane, where the subscript 'S' represents the sample coordinate frame. Two neighboring crystals indicated in blue and in green are separated by an interface marked in red. The purple line is the intersection line of the sample surface $(001)_S$ and the interface, *i.e.* the trace of the interface. Take the *xOy* plane as the projection plane, the stereographic projection of the interface normal $\boldsymbol{n_{int.}}$ should be in the plane that consists of $\boldsymbol{n_{int.}}$ and *z* axis. That is to say the pole should be in the orange line in *xOy* plane. Since the trace of the interface is perpendicular to $\boldsymbol{n_{int.}}$ and *z* axis, it must be perpendicular to the line between point *O* and its projection pole. Hence, for a given crystalline plane and the orientation information of the crystal, the trace of this plane can be calculated. By comparing the calculated trace with the observed ones, the Miller indices of the interface can be determined.

3.7 Orientation relationship

The transformation OR between the parent crystal and the product crystal is usually defined by a pair of parallel crystalline planes and a pair of in-plane parallel directions from the corresponding parent and product phases, as demonstrated in the equation below:

$$(h_1k_1l_1)_{parent}//(h_2k_2l_2)_{product} \qquad [u_1v_1w_1]_{parent}//[u_2v_2w_2]_{product} \tag{3.22}$$

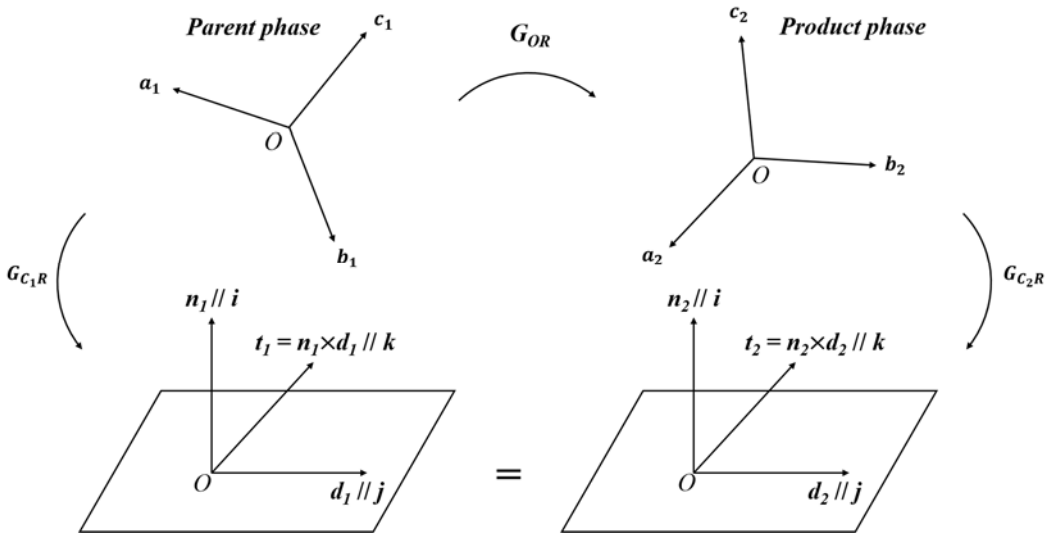

Fig. 3.8 Schematic of coordinate transformation between the parent and the product crystals under a specific OR.

To determine the OR, the coordinate transformation matrix of OR should be calculated first. As illustrated in **Fig. 3.8**, a Cartesian coordinate system '*i*-*j*-*k*' is built based on the OR plane and the OR direction. Basis vector $\boldsymbol{i}$ is parallel to the normal of the OR plane, $\boldsymbol{j}$ is parallel to the OR direction and $\boldsymbol{k}$ is parallel to the cross product of the OR plane normal direction and the OR direction. According to the geometrical relations between the OR plane normal and OR direction, we have

$$\begin{aligned} \boldsymbol{n_i} &= \left((h_i \quad k_i \quad l_i) \times g_i^*\right)^T \\ \boldsymbol{d_i} &= \begin{pmatrix} u_i \\ v_i \\ w_i \end{pmatrix} \qquad (i = 1, 2) \\ \boldsymbol{t_i} &= \boldsymbol{n_i} \times \boldsymbol{d_i}. \end{aligned} \tag{3.23}$$

After orthonormalization, the three basis vectors of the Cartesian coordinate system can be obtained:

$$\begin{aligned} \boldsymbol{i_i} &= \frac{\boldsymbol{n_i}}{\sqrt{(\boldsymbol{n_i})^T \times g_i \times \boldsymbol{n_i}}} \\ \boldsymbol{j_i} &= \frac{\boldsymbol{d_i}}{\sqrt{(\boldsymbol{d_i})^T \times g_i \times \boldsymbol{d_i}}} \qquad (i = 1, 2) \\ \boldsymbol{k_i} &= \frac{\boldsymbol{t_i}}{\sqrt{(\boldsymbol{t_i})^T \times g_i \times \boldsymbol{t_i}}}, \end{aligned} \tag{3.24}$$

where g_i is the metric tensor of the direct space of the corresponding crystal. The coordinate transformation matrices G_{C_1R} and G_{C_2R} can be written as:

$$G_{C_1R} = (\boldsymbol{i_1} \quad \boldsymbol{j_1} \quad \boldsymbol{k_1}) \qquad G_{C_2R} = (\boldsymbol{i_2} \quad \boldsymbol{j_2} \quad \boldsymbol{k_2}). \tag{3.25}$$

Thus, the coordinate transformation matrix of OR — G_{OR} can be acquired with the equation below:

$$G_{OR} = G_{C_1R} \times \left(G_{C_2R}\right)^{-1}. \tag{3.26}$$

With a given OR, the coordinate transformation matrix between the parent and product phases can be easily calculated. Hence, for a two phases coexisting material, the effective OR can be easily determined with the measured orientation information of the two phases. Moreover, the orientation of the parent or product phase can also be derived with the given OR even if the microstructure of the alloy contains only one phase, either the parent or the product.

3.8 Martensitic transformation crystallography

3.8.1 Bain distortion

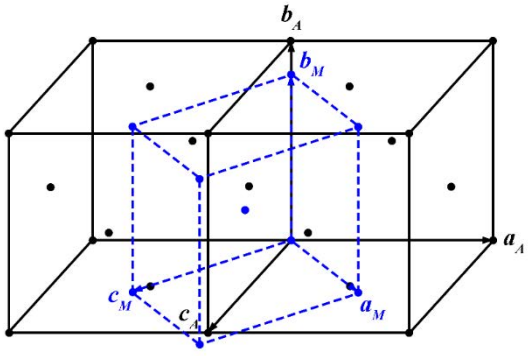

Fig. 3.9 Illustration of the Bain distortion in the alloy undergoes a martensitic transformation from face-centred cubic austenite to body-centred orthorhombic martensite. The black and blue points represent the Bravais lattice points of the austenite and martensite, respectively.

Fig. 3.9 is an illustration of the Bain distortion in an alloy undergoes a martensitic transformation from face-centred cubic austenite to body-centred orthorhombic martensite. a_M, b_M, c_M and a_A are the lattice parameters of the martensite and austenite, respectively. The stretch transformation tensor is as follows [107]:

$$U_1 = \begin{pmatrix} \frac{\eta_1+\eta_3}{2} & 0 & \frac{\eta_1-\eta_3}{2} \\ 0 & \eta_2 & 0 \\ \frac{\eta_1-\eta_3}{2} & 0 & \frac{\eta_1+\eta_3}{2} \end{pmatrix}, \tag{3.27}$$

where

$$\eta_1 = \sqrt{2}a_M/a_A,\ \eta_2 = b_M/a_A,\ \eta_3 = \sqrt{2}c_M/a_A \tag{3.28}$$

are the principal strains of lattice distortion under Bain distortion. With the symmetry operations of the cubic crystal system, other equivalent stretch transformation tensors U_n can be obtained:

$$U_n = (S_A^n)^{-1} U_1 S_A^n \ (\mathrm{n} = 1\sim24), \tag{3.29}$$

where S_A^n is the *n*-th symmetry operation of the cubic crystal system. Thus, we can obtain 6 distinct stretch transformation tensors in total, *i.e.* there exist 6 equivalent Bain distortions.

3.8.2 Sandwich-like microstructure, habit plane and deformation gradient tensor

As mentioned in Chapter 1, in general a single variant cannot form an invariant-plane. Hence, the martensite always exhibits a sandwich-like microstructure, as illustrated in **Fig. 3.10**, especially in the cubic to orthorhombic transformation. In this figure, two distinct variants are distributed alternately. Variant V_B is the basic component of this structure and in majority in volume, whereas variant V_A is formed to accommodate the deformation generated by V_B and to ensure a macroscopic invariant-plane, *i.e.* the habit plane. Here we define the variant that has a higher volume fraction in this structure as the major variant and the other the minor variant.

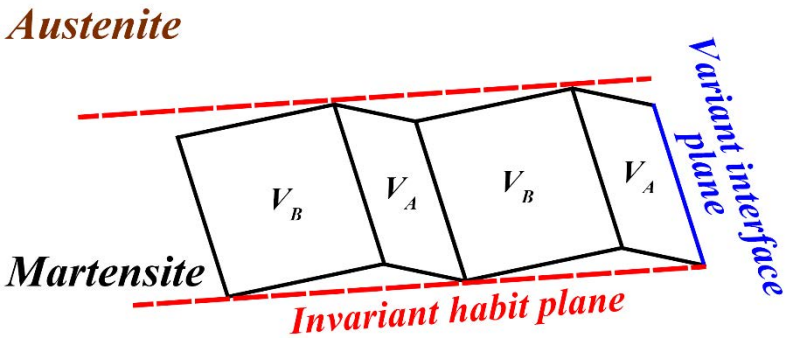

Fig. 3.10 Illustration of the sandwich-like microstructure from martensitic transformation.

In order to minimize the interfacial energy and keep the coherency of the interfaces (the variant interface plane and the habit plane), during the formation of such a microstructure, two geometrical compatibility conditions should be satisfied. One is on the variant interface plane, expressed as Eq. (3.30) [107] and the other is on the habit plane, expressed as Eq. (3.31) [107]. The following two equations:

$$Q_1 U_B - U_A = \boldsymbol{a_t} \otimes \boldsymbol{n_t} \tag{3.30}$$

$$Q_2(\lambda Q_1 U_B - (1-\lambda)U_A) - I = \boldsymbol{a_h} \otimes \boldsymbol{n_h}, \tag{3.31}$$

must have solutions ($\boldsymbol{a_t}$, $\boldsymbol{n_t}$, $\boldsymbol{a_h}$, $\boldsymbol{n_h}$, Q_1, Q_2, λ) for given U_A and U_B. Here Q_1 and Q_2 are two additional rotation matrices for the geometrical compatibility conditions; U_B and U_A are two stretch transformation tensors corresponding to variant V_B and V_A; $\boldsymbol{n_t}$ and $\boldsymbol{n_h}$ are the normal direction of the variant interface plane and the habit plane that are expressed under the crystal coordinate frame of austenite; $\boldsymbol{a_t}$ and $\boldsymbol{a_h}$ are two vectors on the variant interface plane and the habit plane, respectively; λ is the volume fraction of V_B; I is the identity matrix.

3.8.3 Wedge model and interface mismatch

At the beginning stage of martensitic transformation from cubic austenite to orthorhombic martensite, two sandwich-like martensite can form a wedge-shaped morphology in some alloys, as illustrated in **Fig. 3.11**.

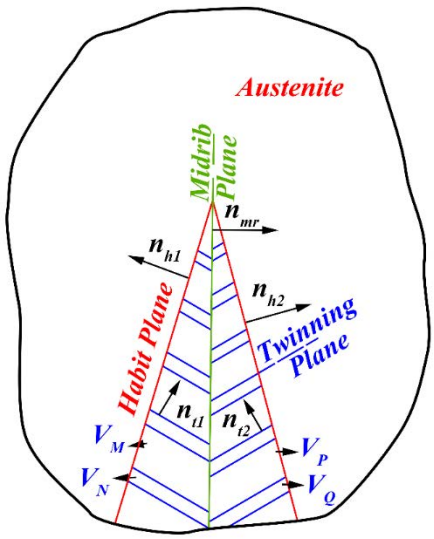

Fig. 3.11 Illustration of wedge-shaped morphology in austenite.

It can be seen that on each side of the midrib plane, there are two variants forming a sandwich-like structure. In order to form such a wedge-shaped microstructure with 2 sandwiches with the minimum interfacial energy, in addition to the 4 geometrical compatibility conditions for the 2 adjacent variant interfaces (with the normal directions $\boldsymbol{n_{t1}}$ and $\boldsymbol{n_{t2}}$) and the two habit planes (with the normal directions $\boldsymbol{n_{h1}}$ and $\boldsymbol{n_{h2}}$), the geometrical compatibility condition for the midrib plane should also be satisfied. Thus, we have [107]:

$$\begin{aligned} Q_{11}U_M - U_N &= \boldsymbol{a_{t1}}\otimes\boldsymbol{n_{t1}} \\ Q_{21}U_P - U_Q &= \boldsymbol{a_{t2}}\otimes\boldsymbol{n_{t2}} \\ Q_{12}(\lambda_1 Q_{11}U_M - (1-\lambda_1)U_N) - I &= \boldsymbol{a_{h1}}\otimes\boldsymbol{n_{h1}} \\ Q_{22}\left(\lambda_2 Q_{21}U_P - (1-\lambda_2)U_Q\right) - I &= \boldsymbol{a_{h2}}\otimes\boldsymbol{n_{h2}} \\ (\boldsymbol{a_{h1}}\otimes\boldsymbol{n_{h1}} + I) - (\boldsymbol{a_{h2}}\otimes\boldsymbol{n_{h2}} + I) &= \boldsymbol{a_{mr}}\otimes\boldsymbol{n_{mr}}, \end{aligned} \tag{3.32}$$

where Q_i (i = 11, 12, 21, 22) are additional rotation matrices for the geometrical compatibility conditions; U_i (i = M, N, P, Q) are the transformation stretch tensors of the 4 variants; $\boldsymbol{a_i}$ (i = t1, t2, h1, h2, mr) are vectors on the corresponding planes with the normal directions $\boldsymbol{n_i}$; λ_i (i = 1, 2) are the volume fractions of variants V_M and V_P, the major variants, as shown in **Fig. 3.11**.

It should be noticed that the midrib plane constructed by the last equation of Eq. (3.32) is a coherent and stress free plane without atomic misfits. However, in reality, such conditions are rarely met. Thus to characterize a non-coherent midrib plane, we can induce a tiny rotation Q_{mr} [130] to describe the incompatibility of the two sandwiches on the midrib plane, as demonstrated in:

$$Q_{mr}(\boldsymbol{a_{h1}}\otimes\boldsymbol{n_{h1}} + I) - (\boldsymbol{a_{h2}}\otimes\boldsymbol{n_{h2}} + I) = \boldsymbol{a_{mr}}\otimes\boldsymbol{n_{mr}}. \tag{3.33}$$

Then, we can use a rotation angle θ_{mr} [130]:

$$\theta_{mr} = \left| arc\cos\left(\frac{tr(Q_{mr}) - 1}{2}\right)\right|, \tag{3.34}$$

instead of the rotation matrix Q_{mr} to quantify the misfit on this plane. By considering the value of the rotation angle θ_{mr}, we can judge the possibility of the formation of wedge-shaped structure (with a non-coherent midrib plane) and predict the morphology of a microstructure produced by martensitic transformation.

Chapter 4 Crystal structure and crystallographic characteristics of martensite in $Ni_{50}Mn_{38}Sb_{12}$ alloy

4.1 Introduction

For NiMnSb ferromagnetic multifunctional alloys, the crystal structure and the ORs between martensite variants are decisive factors for their magnetic-field-induced behaviors and hence of importance. In this chapter, the forward and its reverse martensitic transformation temperatures of $Ni_{50}Mn_{38}Sb_{12}$ alloy was explored firstly. Then the crystal structure of $Ni_{50}Mn_{38}Sb_{12}$ martensite, including the crystal system, the space group, the lattice parameters and atomic coordinates, are fully resolved. The morphology of martensite was observed using SEM. In addition, with the accurately determined crystal structure information, EBSD measurement was conducted. Twin relationship and twinning elements for different variant pairs and twin types were determined. Finally, the characteristics of the twinning plane was investigated with the trace analysis method.

4.2 Experimental

In this chapter, a polycrystalline NiMnSb alloy with nominal composition $Ni_{50}Mn_{38}Sb_{12}$ (at. %) was used. The detailed information on sample preparation are given in Chapter 2. The transformation temperatures were detected by DSC. The lattice constants of the constituent phase was measured by XRD at room temperature. The microstructural and crystallographic features were investigated by SEM-EBSD.

4.3 Martensitic transformation and crystal structure of martensite

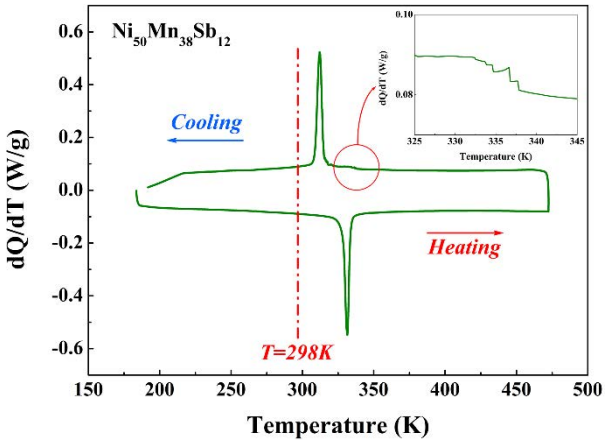

Fig. 4.1 Cooling and heating DSC curves for the $Ni_{50}Mn_{38}Sb_{12}$ alloy.

Fig. 4.1 displays the heating and cooling DSC curves of the $Ni_{50}Mn_{38}Sb_{12}$ alloy. The sharp exothermic and endothermic peaks on cooling and heating indicate the first-order phase transformations (the martensitic transformation and its reverse). The small steps outlined with the red circle on the cooling curve infer that a second-order transformation has occurred (the magnetic transformation). It can be seen that, during the cooling process, both the first- and the second-order transformations can be detected, whereas during the heating process only the austenitic transformation (first-order) can be detected since the temperature of the magnetic transformation (second-order) is close to the austenitic transformation temperature. The martensitic transformation start temperature M_s, martensitic transformation finish temperature M_f, austenitic transformation start temperature A_s and austenitic transformation finish temperature A_f determined using the tangent method, and the Curie temperature T_C^A of the $Ni_{50}Mn_{38}Sb_{12}$ austenite determined from the tangent change at the highest step in the cooling curve, are summarized in **Table 4.1**. Compared with the transformation temperatures of the NiMnSb alloys that have common or similar compositions, obtained by DSC, vibrating sample magnetometer (VSM) and physical property measurement system (PPMS) in the literature [34, 36, 59, 66, 69, 73, 75, 93], we find that the difference for each temperature in the present measurements is within ± 30K. This is mainly related to the change in composition, as for NiMnSb alloys the transformation temperatures are very sensitive to the concentrations of the

constituent elements. Different measurement approaches, like VSM and PPMS, could also have influences on the transformation temperatures and cause deviations. Obviously, at room temperature, the martensitic transformation is complete for the present alloy, and a single martensite phase is obtained.

Table 4.1 Martensitic transformation start (M_s) and finish (M_f) temperatures, austenitic transformation start (A_s) and finish (A_f) temperatures, and Curie temperature of $Ni_{50}Mn_{38}Sb_{12}$ austenite (T_C^A) determined from DSC data (K).

Component	*Ms*	M_f	A_s	A_f	T_C^A
$Ni_{50}Mn_{38}Sb_{12}$	314.79	308.60	328.42	333.76	332.45

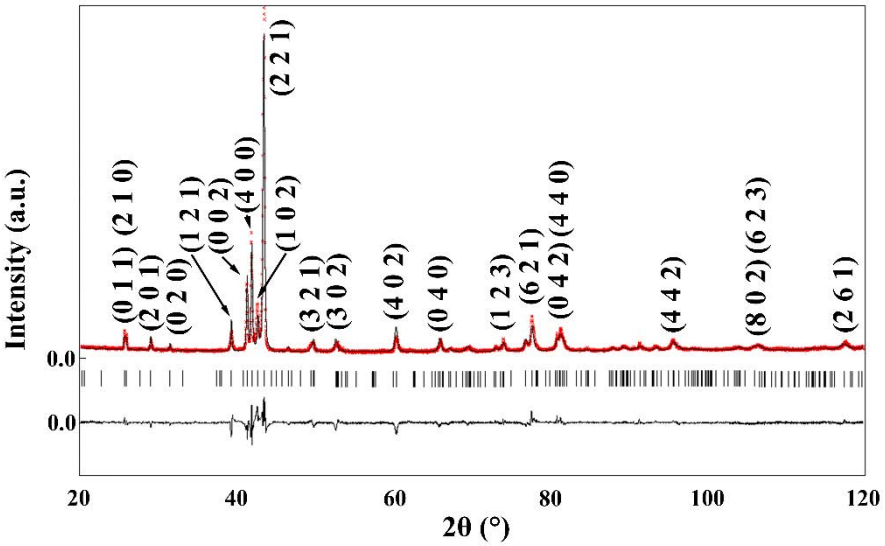

Fig. 4.2 Measured (red points) and simulated (black line) XRD patterns for the $Ni_{50}Mn_{38}Sb_{12}$ alloy at room temperature. The difference between the two patterns is shown as a line profile in black at the bottom of the figure. The agreement factors R_p and R_{wp} are 0.09 and 0.13, respectively. For reference, the exact Bragg diffraction positions are indicated with the black vertical lines.

Fig. 4.2 shows the measured (red points) room-temperature XRD pattern for the $Ni_{50}Mn_{38}Sb_{12}$ alloy. Using the *4O* crystal structure model [77, 79], the measured diffraction peaks are all indexed. This indicates that the martensite of the $Ni_{50}Mn_{38}Sb_{12}$ alloy possesses a *4O* modulated structure, which is in good agreement with the results reported for other alloys with similar compositions [77, 79]. The lattice constants and the fractional atomic positions of the present martensite were further refined by the Rietveld method using *JANA2006* [131]. Complete crystal structure information, *i.e.* lattice parameters, fractional atomic coordinates

and site-occupancy factors (s.o.f.s), for the present martensite, was obtained and is displayed in **Table 4.2**. The simulated pattern and its difference from the measured one (in black) are shown in **Fig. 4.2**. Good agreement factors, such as R_p = 0.09 and R_{wp} = 0.13, are obtained. These values are comparable to those reported for NiMnGa [132, 133] and NiMnIn [134] Heusler type alloys. The results indicate that the measured and simulated patterns are in good agreement. The determined structural parameters were further verified by EBSD. **Fig. 4.3** shows a measured Kikuchi line pattern for the martensite and the calculated pattern using the determined structure parameters in **Table 4.2**. The excellent fit between the experimental and calculated patterns validates the structure parameters given in **Table 4.2**. With this complete crystal structure information, further crystallographic characterizations of the associated martensite can be realized by EBSD.

Table 4.2 Space group, lattice parameters, atomic coordinates (*x*, *y*, *z*) and site occupancy factors (s.o.f.s) for $Ni_{50}Mn_{38}Sb_{12}$ martensite at room temperature.

Space group	Lattice parameters	Atom	Wyckoff position	*x*	*y*	*z*	s.o.f.
No.051 *Pmma*	a = 8.5788 Å b = 5.6443 Å c = 4.3479 Å $\alpha = \beta = \gamma = 90°$	Ni	*4h*	0	0.7547	0.5	1
			4k	0.25	0.2483	0.0731	1
		Mn	*2a*	0	0	0	1
			2f	0.25	0.5	0.5731	1
			2b	0	0.5	0	0.52
			2e	0.25	0	0.5731	0.52
		Sb	*2b*	0	0.5	0	0.48
			2e	0.25	0	0.5731	0.48

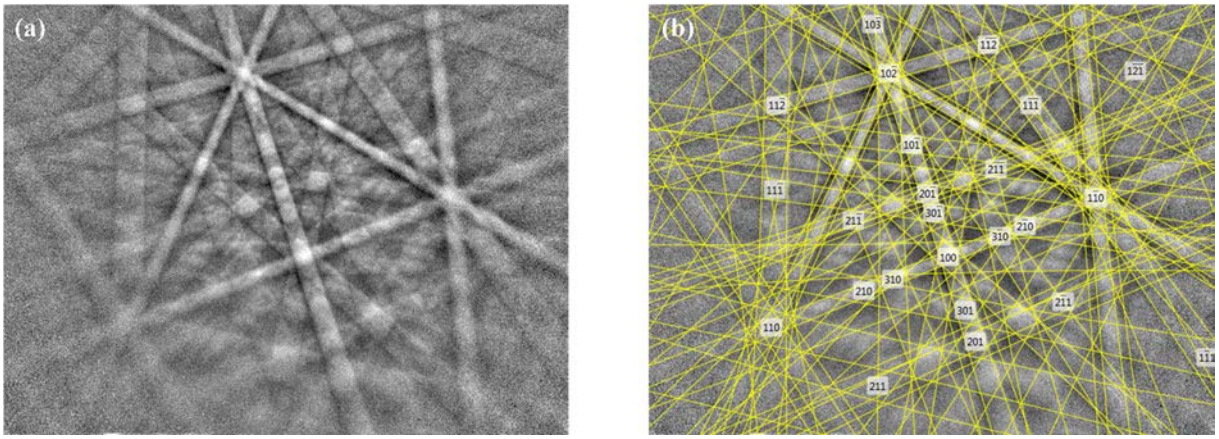

Fig. 4.3 (a) Measured Kikuchi line pattern of martensite. (b) The calculated pattern (in yellow) using the *4O* crystal structure parameters in **Table 4.2**.

4.4 Microstructural features

Fig. 4.4(a) shows a typical SEM BSE image of the present $Ni_{50}Mn_{38}Sb_{12}$ alloy at room temperature. The original austenite grain boundaries are marked with yellow lines. It can be seen that, within the original austenite grains, martensite is organized in broad plates 5 - 10 micrometers wide, sometimes running through the whole grain. From **Fig. 4.4**(b), an enlarged BSE image of the area enclosed in the red rectangle in **Fig. 4.4**(a), it is seen that the broad plates contain a large amount of fine lamellar martensite; the width of the lamellae is in sub-micrometer range. Within the plates, the lamellae are nearly parallel, whereas from plate to plate, their length directions change, as indicated by the labels P_1 and P_2 in **Fig. 4.4**(b): in plate P_1, the lamellae are oriented vertically, whereas in P_2, they are oriented horizontally. In each plate, there are two kinds of lamellar boundary, one straight (shown in zone Z_1 in **Fig. 4.4**(b)) and the other bent (shown in zones Z_2 and Z_3 in **Fig. 4.4**(b)).

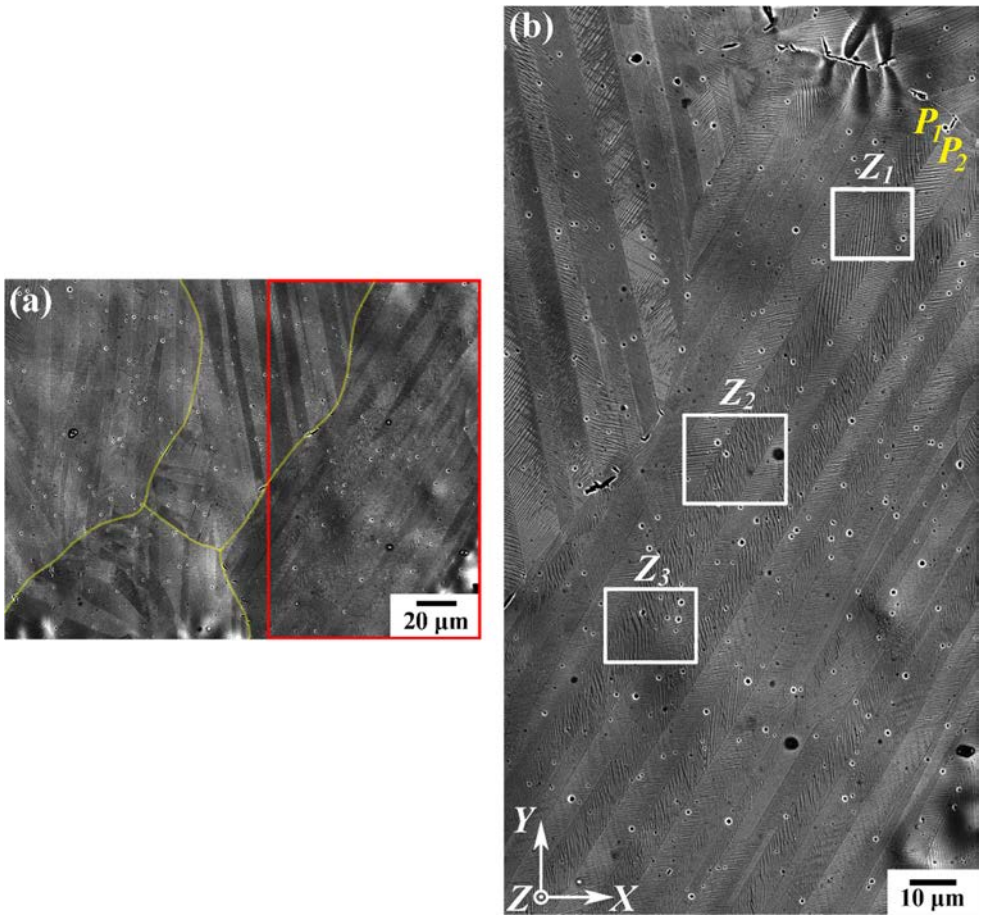

Fig. 4.4 (a) SEM BSE image of the $Ni_{50}Mn_{38}Sb_{12}$ alloy. (b) An enlarged BSE image of the area enclosed in the red rectangle in part (a).

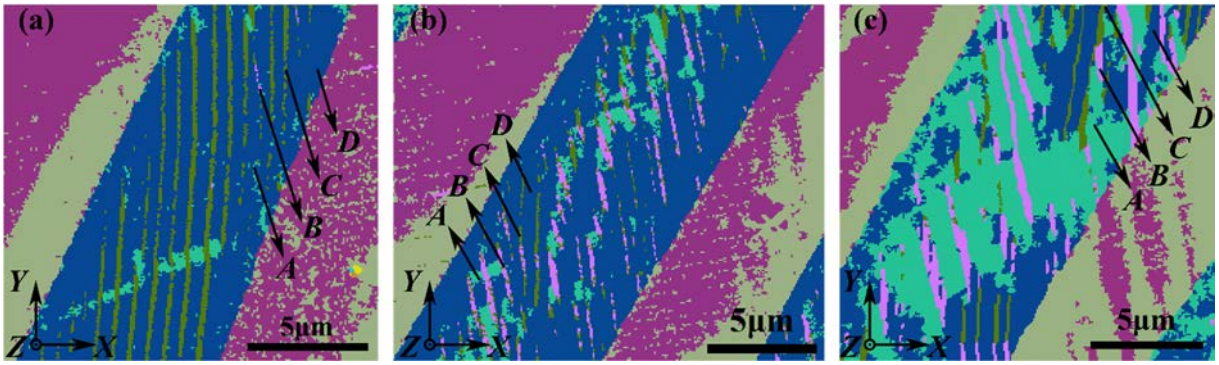

Fig. 4.5 EBSD 'All Euler' (*Channel5*) orientation maps of *4O* martensite in different areas of **Fig. 4.4**(b): (a) zone Z_1; (b) zone Z_2; (c) zone Z_3.

Global EBSD analyses demonstrated that the number of martensite variants in terms of crystallographic orientation in each broad plate is constant, equal to 4. One straight lamellar martensite corresponds to one orientation variant and the variants appear repeatedly in each broad plate. The area fractions of the variants change from place to place within the plate, but the number of variants remains constant. As examples, the EBSD orientation maps of the three zones marked Z_1, Z_2 and Z_3 in **Fig. 4.4**(b), which belong to one broad plate but have differently oriented lamellar boundaries, are displayed in **Fig. 4.5**. In Z_1, close to the austenite boundary, most of the lamellar boundaries are straight, whereas in Z_3, in the interior of the austenite, they are bent. Zone Z_2 is between the two and is a mixture of the two. It can be seen that there are always 4 orientation variants (*A*, *B*, *C* and *D*) in each zone, although the fractions of the variants are different. In **Fig. 4.5**(a) (Z_1), variants *C* (thinner) and *D* (thicker) are distributed alternately and are in the majority. Only very occasionally do variants *A* and *B* appear. In **Fig. 4.5**(b), the fine lamellae begin to bend and the amounts of variants *A* and *B* increase. Although the amounts of variants *C* and *D* begin to decrease, that of variant *D* is still the highest among all the variants. In **Fig. 4.5**(c), the fractions of variants *A* and *B* increase further and become dominant, especially variant *A*. As the lamellae are too fine and oriented unfavorably, the EBSD system could not distinguish thin variants in neighboring plates, so orientation information on the variants coloured in grey and pink on the left- and the right-hand sides of the central plate in **Figs. 4.5**(a) ~ (c) is not available.

4.5 Orientation relationships between martensite variants and variant interfaces

Table 4.3 shows the calculated misorientation between different variant pairs, represented by a rotation angle ω and a rotation axis ***d***. The rotation axes are expressed in the Cartesian crystal coordinate system of the martensite. For convenient identification of the rotation axis, the nearest rational lattice direction or the nearest normal direction to a rational lattice plane, together with the angular deviation, are also given in the table.

Table 4.3 Misorientation angle ω, indices of rotation axis ***d*** (Cartesian crystal coordinate system), and angles between ***d*** and its nearest rational lattice direction (Miller indices) or nearest rational lattice plane normal (Miller indices) for different variant pairs.

Variant pair	ω (°)	Rotation axis ***d***	Angle between ***d*** and its nearest rational direction	Angle between ***d*** and its nearest plane normal
A and *D*	179.5164	[$\overline{0.7083}$ $\overline{0.0029}$ 0.7059]	0.52° from [$\bar{1}02$]	0.33° from ($\bar{2}01$)
	179.6647	[0.7059 0.0042 0.7083]	0.37° from [102]	0.53° from (201)
B and *C*	179.4425	[0.7030 0.0009 0.7112]	0.07° from [102]	0.74° from (201)
	179.9019	[$\overline{0.7112}$ $\overline{0.0049}$ 0.7029]	0.77° from [$\bar{1}02$]	0.30° from ($\bar{2}01$)
A and *B*	93.9657	[0.7146 0.0028 0.6995]		
	179.7659	[$\overline{0.5115}$ $\overline{0.6822}$ 0.5225]	0.33° from [$\bar{1}\bar{2}2$]	
C and *D*	94.3951	[$\overline{0.7085}$ $\overline{0.0036}$ 0.7057]		
	179.6938	[0.5178 0.6795 0.5198]	0.22° from [122]	
A and *C*	85.9411	[$\overline{0.7054}$ $\overline{0.0003}$ $\overline{0.7088}$]		
	179.9794	[$\overline{0.4831}$ 0.7317 0.4808]		0.29° from ($\bar{2}21$)
B and *D*	85.7085	[0.7047 $\overline{0.0091}$ $\overline{0.7094}$]		
	179.2905	[$\overline{0.4825}$ 0.7331 $\overline{0.4793}$]		0.17° from ($\bar{2}2\bar{1}$)

It is seen that, within the limits of experimental accuracy, there are two 180° rotation axes between variant pair *A* and *D* (or *B* and *C*), but only one between *A* and *B* (or *C* and *D*) and between *A* and *C* (or *B* and *D*). It can also be seen that one of the 180° rotation axis for variant pair *A* and *D* (or *B* and *C*) is close to the rational direction [102], and the other is close to the normal direction of the rational plane ($\bar{2}$01). For variant pair *A* and *B* (or *C* and *D*), the 180° rotation axis is close to the rational direction [$\bar{1}\bar{2}$2], whereas for variant pair *A* and *C* (or *B* and

D), the 180° rotation axis is close to the normal directon of the rational plane $(\bar{2}21)_M$. The angles between the calculated directions and the rational approximations are very small. The small discrepancies can be considered as systematic errors, within the limits of the accuracy of the EBSD measurements. Thus, according to the defination of the various twin types, variant pair *A* and *D* (or *B* and *C*) could be a compound twin, variant pair *A* and *C* (or *B* and *D*) a type I or mirror twin and variant pair *A* and *B* (or *C* and *D*) a type II or rotation twin.

With this twin type information, all the twinning elements can be calculated on the basis of the method as mentioned in Chapter 3. The results are displayed in **Table 4.4**. It can be seen that the indices of the K_1 and K_2 planes in type I and type II twins are interchanged, and so are the $\boldsymbol{\eta_1}$ and $\boldsymbol{\eta_2}$ directions. The shear magnitudes for type I and type II twins are identical but much higher than that of the compound twin.

Table 4.4 Twinning elements expressed in the orthorhombic Bravais lattice basis of the $Ni_{50}Mn_{38}Sb_{12}$ martensite.

Twinning elements	Type I twin (*A*:*C*, *B*:*D*)	Type II twin (*A*:*B*, *C*:*D*)	Compound twin (*A*:*D*, *B*:*C*)
K_1	$(2\bar{2}\bar{1})_M$	$(1.374\ \overline{1.687}\ \bar{1})_M$	$(201)_M$
K_2	$(\overline{1.374}\ \overline{1.687}\ 1)_M$	$(\bar{2}\bar{2}1)_M$	$(\bar{2}01)_M$
$\boldsymbol{\eta_1}$	$[\bar{1}\ \overline{2.377}\ 2.755]_M$	$[\bar{1}\bar{2}2]_M$	$[10\bar{2}]_M$
$\boldsymbol{\eta_2}$	$[1\bar{2}\bar{2}]_M$	$[1\ \overline{2.377}\ \overline{2.755}]_M$	$[102]_M$
P	$(13.602\ 1\ 5.801)_M$	$(13.602\ \bar{1}\ 5.801)_M$	$(010)_M$
γ	0.1590	0.1590	0.0271

The interface planes between the 6 pairs of variants were further identified using trace analysis method as mentioned in Chapter 3. With the orientation information of the variants, the trace of any given crystalline plane of a variant on the sample surface can be calculated through coordinate transformation of the plane normal to the sample coordinate system and then through the vector cross product of the plane normal with the sample surface normal. Thus, the plane having the trace which is best matched with the observed one should be the interface plane. Analyses show that the interface planes between the variants are very close to their corresponding twinning planes, *i.e.* the K_1 planes. The results are represented with pole figures of the K_1 planes, as shown in **Figs. 4.6**(a) ~ (f). For ease of comparison, part of the orientation

map and the band contrast image of **Fig. 4.5**(b) are given in **Figs. 4.6**(g) and (h), respectivly. The interfaces between different variant pairs are marked with coloured lines on the orientation map and the band contrast image, and their traces are plotted in the corresponding pole figures with dashed lines.

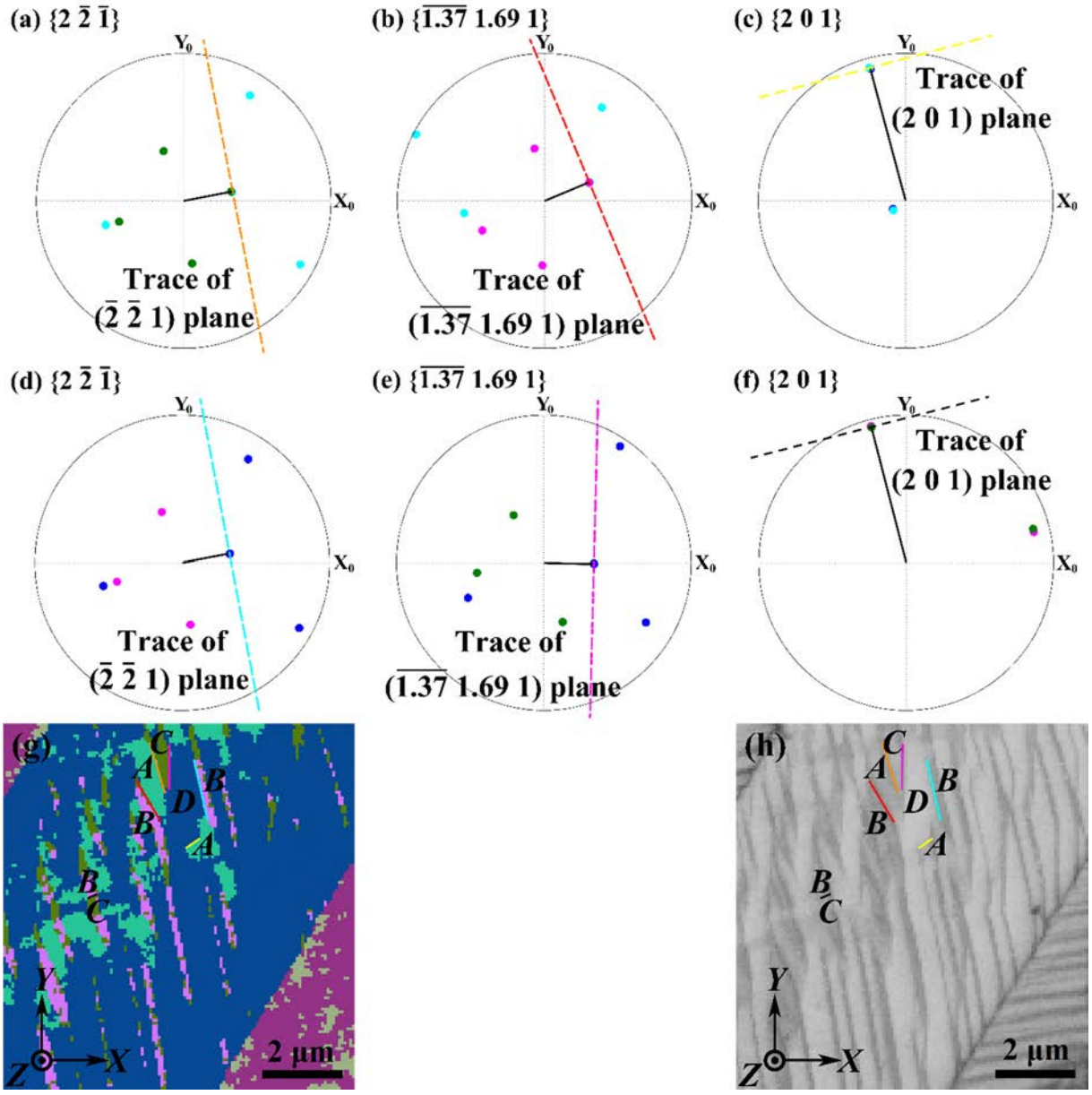

Fig. 4.6 (a) ~ (f) Pole figures of the K_1 planes for different variant pairs. (a) *A* and *C*, (b) *A* and *B*, (c) *A* and *D*, (d) *B* and *D*, (e) *C* and *D*, and (f) *B* and *C*. (g) Part of the orientation map of **Fig. 4.5**(b) and (h) its corresponding band contrast image. For convenience, the interface traces of different variant pairs in parts (g) and (h) are outlined in different colours that correspond to those of the related K_1 plane traces in the pole figures above.

For each variant pair, ten interfaces have been verified. The deviation angles between the calculated trace of the K_1 plane and the measured variant interface are listed in **Table 4.5**. It can be seen that, the trace of the K_1 plane is almost parallel to the variant interface trace. As the twinning plane is the invariant plane shared by the two variants, the interface between each variant pair should be coherent. Notably, for type I twins the twin interface of variant pair *A* and *C* is almost parellel to that of variant pair *B* and *D* (with a deviation of 0.15°). A similar situation is also found for compound twins (with 1.93°deviation). However, for type II twins, the twin interfaces between different variant pairs (*A* and *B*, and *C* and *D*) are not parallel. The angular difference between the two type II twin interfaces is about 14.5°. This indicates that the type II twins possess two differently oriented interfaces, whereas the type I and the compound twins each have only one kind of interface.

Table 4.5 Deviation angles (°) between the calculated trace of the K_1 plane and the measured trace of twin interface for different variant pairs.

Twin interface	Type I twin		Type II twin		Compound twin	
No.	*A* and *C*	*B* and *D*	*A* and *B*	*C* and *D*	*A* and *D*	*B* and *C*
1	3.96	0.96	0.03	0.77	0.75	3.64
2	0.04	1.87	3.52	2.84	0.84	0.40
3	0.60	0.25	0.62	1.74	3.90	0.09
4	2.30	0.47	0.07	1.33	0.34	2.04
5	3.40	0.35	2.96	1.98	3.09	1.41
6	2.00	0.15	2.25	0.78	3.83	3.40
7	2.57	0.66	2.22	1.29	2.89	1.77
8	3.87	0.71	0.02	2.53	4.70	4.30
9	3.23	1.71	1.84	2.26	4.41	3.05
10	1.31	1.94	0.13	0.26	5.03	0.92
Minimum	0.04	0.15	0.02	0.26	0.34	0.09
Maximum	3.96	1.94	3.52	2.84	5.03	4.30
Average	2.33	0.91	1.37	1.58	2.98	2.10

For NiMn-based ferromagnetic multifunctional alloys, the magnetic field-induced strain effect and the MCE are two important and widely investigated properties that are closely associated with the crystal structure and the microstructure. So far the highest shape memory effect and caloric effect have been realized in trained single-crystal alloys [32, 135, 136]. The aim of the training is to optimize these properties by eliminating the undesired variants.

Obviously, variant elimination through mechanical training is realized by variant reorientation *via* detwinning processes through variant interface movement. The above results on twin characteristics between variants demonstrate that for NiMnSb martensite the variant organizations are similar to those of NiMnGa alloys [137-139]. Type I and type II twins possess the same amount of shear, which is almost one order of magnitude higher than that of the compound twin. The type II twin has an irrational indexed interface as in the case of NiMnGa. Such interfaces should be composed of stepped planes with rational indices. The crystallographic information on the martensite variants of the present NiMnSb alloy regarding their twin relationship, twinning elements and interfaces is essential to the design of effective training routes and to the understanding of the behaviour of the alloy during the training process. Hence, the detailed crystallographic information on the martensite variants in NiMnSb alloy systems revealed by the present work will be helpful for further investigations on property optimization in these materials.

4.6 Summary

The crystal structure, microstructure and twin relationships of $Ni_{50}Mn_{38}Sb_{12}$ martensite have been investigated in detail. At room temperature $Ni_{50}Mn_{38}Sb_{12}$ alloy is in the martensite state. The crystal structure of the martensite is orthohombic and can be represented with a *4O* superstructure, belonging to the space group *Pmma* (No. 051). The lattice parameters and atomic positions of the martensite are fully resolved. Within the original austenite grains, martensite is organized into broad plates, 5 - 10 μm wide. The plates are composed of fine lamellae. In each plate, there are 4 types of orientation variants appearing repeatedly and forming three types of twins, the type I twin (for variant pairs *A* and *C*, and *B* and *D*), the type II twin (for variant pairs *A* and *B*, and *C* and *D*) and the compound twin (for variant pairs *A* and *D*, and *B* and *C*). The complete twinning elements for each type of twin have been determined. The twin interfaces are identified to be the corresponding twinning planes, K_1. All these results provide fundamental information for NiMnSb alloys and could be useful for interpreting their magnetic and mechanical characteristics.

Chapter 5 Martensitic transformation OR and martensite variant organization of $Ni_{50}Mn_{38}Sb_{12}$ alloy

5.1 Introduction

As is known, in NiMnSb alloys the OR between austenite and martensite is an influential factor on the microstructure of the resultant martensite. As the mechanical and magnetic properties of NiMnSb alloys are closely associated with the martensitic transformation and variant organization, studies on transformation OR and microstructure characteristics of martensite are of importance. In this chapter, a thorough investigation on the organization features of the martensite, the martensitic transformation OR and its correlation with variant organizations of $Ni_{50}Mn_{38}Sb_{12}$ alloy have been fully resolved with the help of SEM BSE imaging, SEM EBSD technique and crystallographic calculations. All these results on morphological and crystallographic characteristics of $Ni_{50}Mn_{38}Sb_{12}$ martensite (resolved in Chapter 4 and this chapter) and martensitic transformation will provide basic information for NiMnSb alloys and could be useful for interpreting the subsequent magnetic and mechanical characteristics associated with the martensitic transformation and further investigation on martensitic transformation crystallography of these alloys.

5.2 Experimental

In this chapter, polycrystalline NiMnSb alloy with nominal composition $Ni_{50}Mn_{38}Sb_{12}$ (at. %) was used. The detailed information on sample preparation are shown in Chapter 2. The microstructural and crystallographic features were investigated by SEM-EBSD.

5.3 Microstructure of $Ni_{50}Mn_{38}Sb_{12}$ martensite

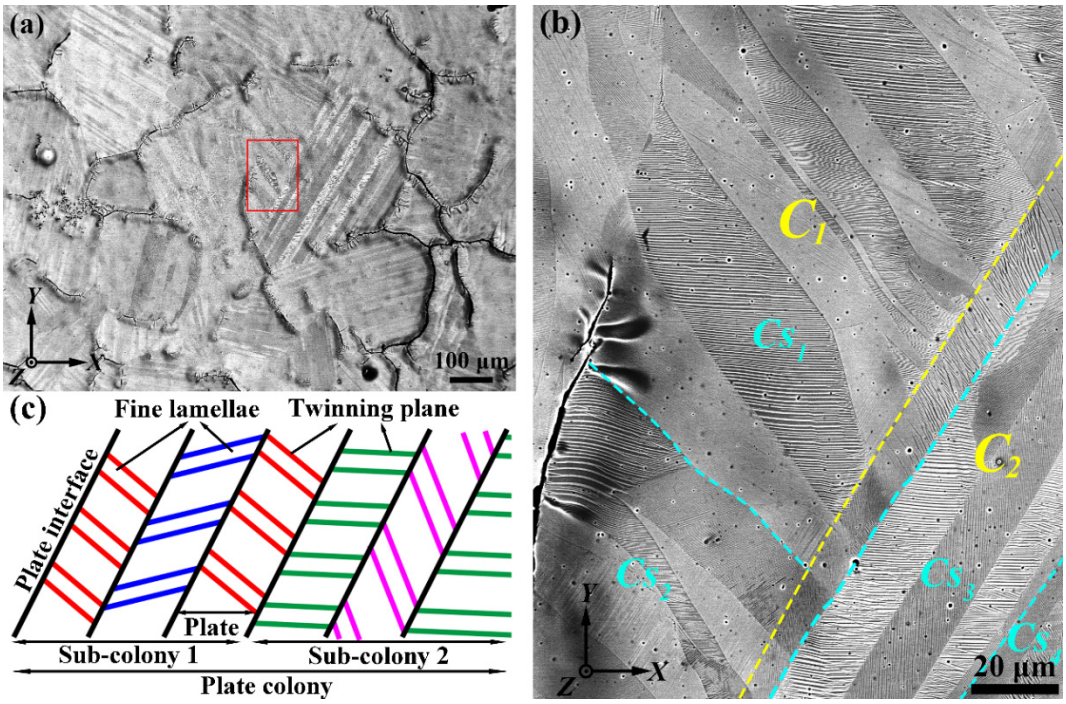

Fig. 5.1 (a) A typical BSE image of $Ni_{50}Mn_{38}Sb_{12}$ alloy; (b) the magnified BSE image of the area enclosed in the red rectangle in (a). The yellow line outlines plate colonies and the light blue lines sub-plate colonies; (c) a microstructrual schema demonstrating the organization of plates from sub-colony to plate colony.

Fig. 5.1 shows a typical BSE micrograph of $Ni_{50}Mn_{38}Sb_{12}$ martensite. It is seen that within the original austenite grains that are in equiaxed shape and outlined by their boundary cracks, martensite is, at mesoscopic scale, organized in plates with various plate interface trace orientations (**Fig. 5.1**(a)). Locally, adjacent plates share a straight plate interface, as seen in **Fig. 5.1**(b), the magnified BSE image of the area enclosed in the red rectangle in **Fig. 5.1**(a). The plates are composed of fine parallel lamellae. From plate to plate, the orientation of the lamellar interface trace changes (**Fig. 5.1**(b)). Here we define a group of plates possessing a common plate interface trace orientation as plate colony, as outlined with the yellow dashed line in **Fig. 5.1**(b) and indicated with C_1 and C_2 in the figure. Global BSE observation reveals that up to 4 distinct plate colonies can be detected in some original austenite grains. Visibly, the plate colonies are composed of plate units according to the lamellar interface trace orientations. By repeating this plate unit, the plate colony is produced. For convenience, we denote such a plate

unit sub-colony and label it *Cs*, as marked with the light blue lines in **Fig. 5.1**(b). For easy understanding of the above definitions from lamella to plate colony, a microstructural schema is made and shown in **Fig. 5.1**(c). It should be noted that at the vicinities of the original austenite grain boundaries, the trace of some plate interfaces become curved. The same situation happens also in plate colony boundary areas. This may be due to the specific local constraints in these areas, indicating that the martensitic transformation is sensitive to mechanical constraints.

5.4 Crystallographic characterization of $Ni_{50}Mn_{38}Sb_{12}$ martensite

Global BSE observation reveals that there are 6 different kinds of plates in terms of the internal lamellar interface trace orientation in each original austenite grain. Thus, we manually measured the orientations of all possible variants in the 6 plates. In total, we found 24 distinct martensite variants and each plate contains 4 distinct variants. The 4 lamellar or intra-plate variants are related one another by three kinds of twin relationships (type I, type II and compound twin), as revealed in Chapter 4, and share one lamellar interface orientation, *i.e.* the K_1 plane $\{2\bar{2}\bar{1}\}_M$ of the type I twin of each variant. The subscript 'M' indicates the martensite. Considering this common feature, we plotted the stereographic projections of the $\{2\bar{2}\bar{1}\}_M$ planes of the 24 variants in the sample coordinate frame. The projections are shown in **Fig. 5.2**.

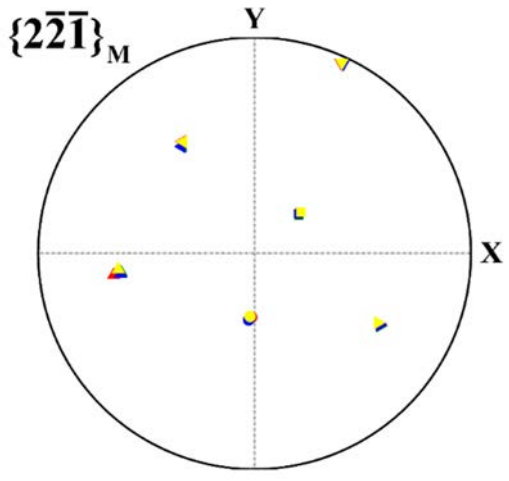

Fig. 5.2 $\{2\bar{2}\bar{1}\}_M$ stereographic projections of the 24 martensite variants. The 4 variants that are originated from one plate are plotted with the same symbol but different colors.

It can be seen that the 24 variants are clustered in 6 groups, each representing one plate. Clearly the number of the variants equals the number of the rotational symmetry elements of the cubic crystal, *i.e.* the variants should be inherited under certain OR from the parent austenite. The transformation ORs will be discussed later.

Using the measured orientation of the variants and their spatial distribution information, variant configurations in sub-colonies and plate colonies are further analyzed. It turns out that one plate colony is composed of 2 distinct sub-colonies and 1 sub-colony contains 2 distinct plates that appear alternately. Thus there are in total 16 distinct variants in one plate colony and 8 distinct variants in one sub-colony. It is clear that the organizations of plate colony and sub-colony, as shown in **Fig. 5.1**(c), are selective but not arbitrary as the numbers of the variants are fixed both in plate colonies and in sub-colonies, hence specific ORs may exist between the adjacent variants in neighboring plates. To find out the selection rule, crystallographic analyses were further conducted on the ORs between the variants in the adjacent plates. Here we take the sub-colony Cs_3 in **Fig. 5.1**(b) as an example and display it with the forward scattered electron (FSD) image in **Fig. 5.3**. For convenience, we denote the plate with the horizontal lamellar interface traces P_h and that with roughly vertical traces P_v, and the corresponding lamellar variants A_i, B_i, C_i and D_i (i = 1, 2) (**Fig. 5.3**). Then we measured the orientations of these variants manually.

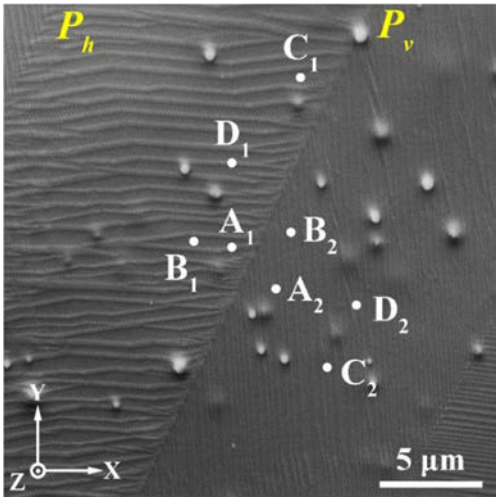

Fig. 5.3 Forward scattered electron (FSD) image of the plates in sub-colony Cs_3 in **Fig. 5.1**(b) and the 8 distinct variants A_1 ~ D_1 and A_2 ~ D_2 detected manually by EBSD. (The bulgy points in the BSE image result from the electrolytic polishing.)

As seen in **Fig. 5.3**, the variants in one plate meet the variants in the adjacent plate at the plate interface. Thus each variant in one plate can have 4 possible combinations with the 4 variants in the other plate. Hence, we calculated the misorientation (ω, ***d***) and the plane normal to the rotation axis ***d*** of all the possible variant pairs from plates P_h and P_v. Results show that for any variant in one plate, there exists only one variant in the adjacent plate that has a 180° rotation relationship with it. The misorientation information of such variant pairs are given in **Table 5.1**.

Table 5.1 180° rotation (ω, ***d***) and the plane normal to the rotation axis ***d*** of the inter-plate variant pairs in sub-colony Cs_3.

Variant pair	Misorientation angle ω (º)	Rotation axis ***d*** (Cartesian crystal coordinate system set to the lattice basis of *4O* modulated martensite)	Plane normal to ***d*** (in the Bravais lattice basis of the *4O* modulated martensite)
A_1&B_2	179.49	<0.03 0.04 1.00>	{0.28 0.20 4.34}$_M$ (2.76° from {001}$_M$)
B_1&A_2	179.42	<0.49 0.72 0.49>	{4.21 4.07 2.13}$_M$ (1.16° from {221}$_M$)
C_1&D_2	179.66	<0.48 $\overline{0.72}$ 0.50>	{4.11 $\overline{4.07}$ 2.18}$_M$ (0.51° from {2$\bar{2}$1}$_M$)
D_1&C_2	179.29	<1.00 $\overline{0.02}$ $\overline{0.02}$>	{8.57 $\overline{0.13}$ $\overline{0.10}$}$_M$ (1.87° from {100}$_M$)

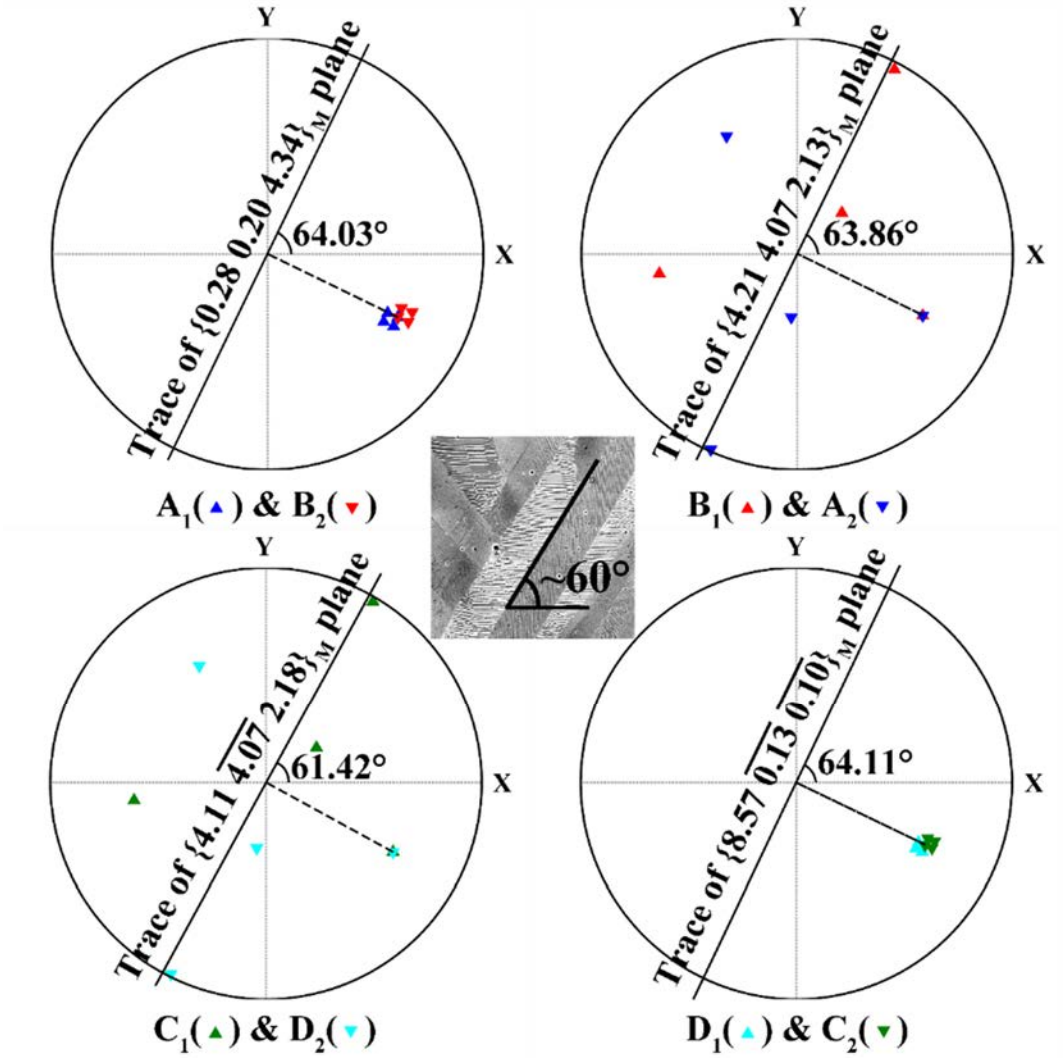

Fig. 5.4 Stereographic projections of the common plane normal to the 180° rotation axis of each inter-plate variant pair from plate P_h and P_v that possesses a 180° rotation. The trace of the common plane is indicated with a solid black line and the rotation axis with a dashed black line. For comparison, the trace of the plate interface is indicated in the image of the microstructure (sub-colony *Cs3* in **Fig. 5.1**(b)).

Then we studied the orientation character of the plane that is normal to the rotation axis of each variant pair. Such a plane should be shared by the corresponding pair of variants. We found that although the Miller indices of the plane change from pair to pair, the spatial orientations of these planes are very close and coincident with that of the plate interface, as shown in **Fig. 5.4**. In the figure, these planes are represented with their stereographic projections in the macroscopic sample coordinate system and their traces as well as the plate interface trace between P_h and P_v in the microstructure are indicated with the black solid lines. The deviation between these planes and the plate interface should be attributed to the experimental uncertainty

arising from the tilt of the sample for EBSD measurement. This result indicates that the plate interface should be the mirror plane of the two variants that possess the 180° rotation. The same results were confirmed by the variants in the plates in the other three sub-colonies *Cs*$_1$, *Cs*$_2$ and *Cs*$_4$ in **Fig. 5.1**(b). However, such a situation is not applicable to the adjacent plates that border the sub-colony boundaries and plate colony boundaries as indicated with the respective light blue lines and yellow lines in **Fig. 5.1**(b). The characteristic variant organization features suggest that during martensitic transformation sub-colonies may form coordinately and grow coordinately. Sub-colony boundaries and plate colony boundaries may form when these sub-colonies meet during the transformation. The knowledge of transformation ORs should be useful to understand the organization features of the present martensite.

5.5 Determination of martensitic transformation OR

5.5.1 Crystal structure and structure simplification

As identified in Chapter 4, the martensite of the $Ni_{50}Mn_{38}Sb_{12}$ alloy possesses a *4O* $(2\bar{2})$ modulated structure of space group *Pmma* (No. 051) with lattice parameters a_M = 8.5788 Å, b_M = 5.6443 Å and c_M = 4.3479 Å [140]. The austenite has a cubic *L2*$_1$ structure of space group *Fm*$\bar{3}$*m* (No. 225) with lattice parameter a_A = 5.964 Å [72]. The subscript 'A' indicates the cubic lattice of austenite. According to the published atom occupation information of austenite [79] (in a very similar composition $Ni_{50}Mn_{37}Sb_{13}$) and the structural information of martensite, the unit cells of the austenite and the martensite can be obtained and shown in **Figs. 5.5**(a) and (b).

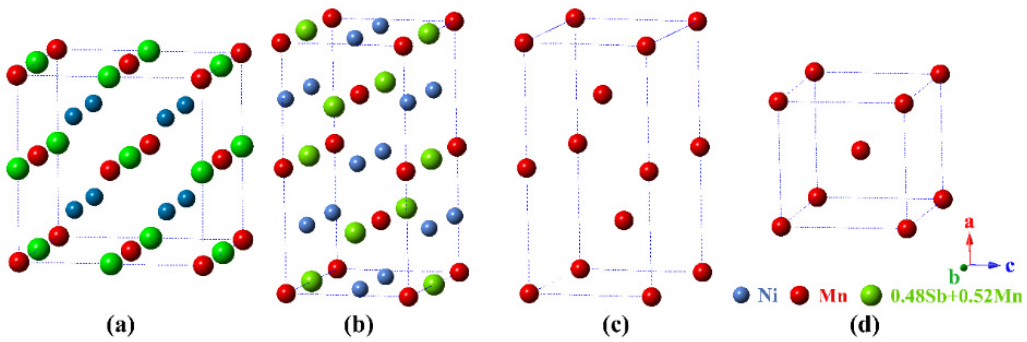

Fig. 5.5 Crystal structure of (a) cubic austenite, (b) *4O* modulated martensite, (c) simplified *4O* modulated martensite and (d) average unit cell of the *4O* modulated martensite.

For simplicity and explicitly, the martensite structure is illustrated with only the Mn atoms and shown in **Fig. 5.5**(c). By ignoring the structural modulations along the *c*-axis of the two Mn at the body centers in each sub cell, the structure can be further simplified and represented with one sub cell, as shown in **Fig. 5.5**(d). We denote such a cell average unit cell. The lattice parameters of this cell are $a_{\overline{M}}$ = 4.2894 Å, $b_{\overline{M}}$ = 5.6443 Å and $c_{\overline{M}}$ = 4.3479 Å. The subscript '$\overline{M}$' indicates the orthorhombic lattice of the average unit cell of martensite.

5.5.2 Determination of transformation OR by crystallographic calculations

Generally, the transformation OR is defined by one pair of parallel crystalline planes and one pair of in plane parallel directions from the corresponding parent and product phases. By consulting the literature, 4 representative ORs, namely the Bain [108], the Kurdjumov-Sachs (K-S) [141], the Nishiyama-Wassermann (N-W) [142, 143] and the Pitsch [144], were selected as the possible transformation OR for the present alloy. By adapting the Miller indices of the published ORs to the structures of the present austenite and the average cell of the martensite, the plane and the direction parallelisms defined by these ORs are specified in **Fig. 5.5**.

Table 5.2 Plane and direction parallelisms defined by the 4 ORs adapted to the structures of the austenite and the average structure of the present martensite.

OR	Parallel lattice plane and direction in two phases
Bain relation	$(010)_A$ // $(010)_{\overline{M}}$ & $[001]_A$ // $[101]_{\overline{M}}$
K-S relation	$(\bar{1}11)_A$ // $(011)_{\overline{M}}$ & $[\bar{1}\bar{1}0]_A$ // $[\bar{1}\bar{1}1]_{\overline{M}}$
N-W relation	$(111)_A$ // $(011)_{\overline{M}}$ & $[1\bar{2}1]_A$ // $[0\bar{1}1]_{\overline{M}}$
Pitsch relation	$(0\bar{1}\bar{1})_A$ // $(1\bar{2}\bar{1})_{\overline{M}}$ & $[0\bar{1}1]_A$ // $[\bar{1}\bar{1}1]_{\overline{M}}$

The above microstructural observations of the $Ni_{50}Mn_{38}Sb_{12}$ reveal that, at room temperature, the martensitic transformation is completed. All the parent austenite has transformed to the product martensite without any retained austenite. Thus the OR is determined indirectly by inspecting the calculated orientations of the austenite from the measured orientation of the martensite variants originated from the same initial austenite grain under the 4 ORs listed in **Table 5.2**. The OR that ensure a common austenite orientation should be the effective one.

Fig. 5.6 displays an EBSD orientation map of the fine martensite lamellas in one plate of *C2*. 4 orientation variants were detected and marked with *A*, *B*, *C* and *D*. To ensure the accuracy of the determination, we used the mean orientation of the 4 martensite variants.

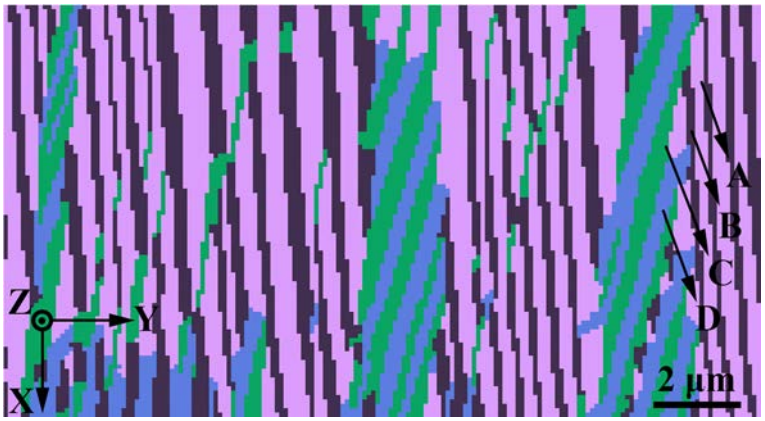

Fig. 5.6 EBSD orientation map of the fine martensite lamellae in one plate.

Thus, a rotation matix R_A that expresses the orientation of the possible original austenite with respect to the sample coordinate system can be calculated with the following equation:

$$R_A = R_M \times G_{M\bar{M}} \times S_M^i \times G_{OR} \times \left(S_A^j\right)^{-1} \tag{5.1}$$

where R_M is the rotation matrix representing the measured orientation of the martensite variant with respect to the sample coordinate system; $G_{M\bar{M}}$ is the coordinate transformation matrix from the crystal coordinate frame set to the *4O* modulated martensite to the crystal coordinate frame set to the average unit cell of martensite; S_M^i (i = 1 ~ 4) and S_A^j (j = 1 ~ 24) are the corresponding rotational symmetry matrices of the orthorhombic and cubic crystal systems and G_{OR} is the coordinate transformation matrix of the possible ORs as listed in **Table 5.2** from the crystal coordinate frame set to the average unit cell of martensite to the crystal coordinate coordinate frame set to the lattice basis of austenite. The detailed calculation method of G_{OR} has been given in Chapter 3. The calculated orientations of the austenite are represented with their $\{001\}_A$ stereographic projections in the sample coordinate system and shown in **Fig. 5.7**.

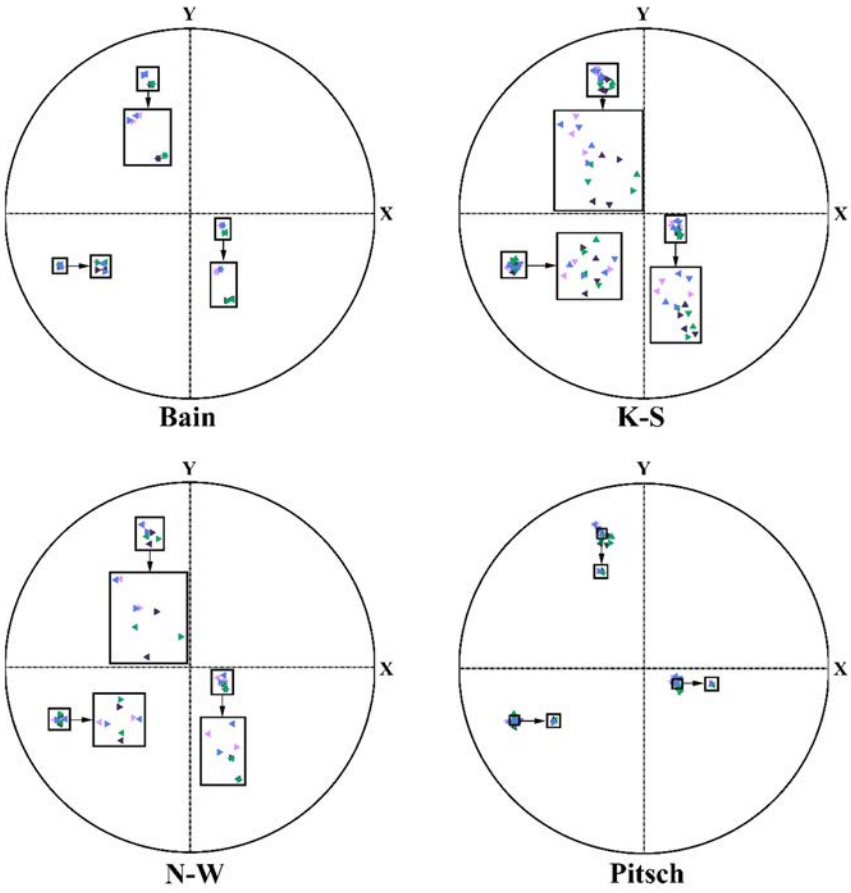

Fig. 5.7 $\{001\}_A$ stereographic projection of austenite under the 4 ORs. Orientations obtained from different martensite variants are distinguished with different colors that correspond to those in **Fig. 5.6**: pink for variant *A*, dark brown for variant *B*, green for variant *C* and blue for variant *D*. The non-equivalent austenite orientations obtained from one martensite variant are differentiated with the orientations of the triangular symbols. The clusters of poles in each stereographic projection are further magnified to a convenient visualization of the positions of the poles.

Due to the symmetry of the cubic system, one austenite orientation is represented with three distinct but equivalent $\{001\}_A$ poles that have been marked with the triangles of the same color and of the same triangle orientation in the figures. The color of the triangles corresponds to that of the martensite variants displayed in **Fig. 5.6**. Due to crystal symmetry, one measured martensite variant can generate several distinct austenite orientations depending on the OR. If the OR is effective for the transformation of the present alloy, the orientations of the austenite calculated from the 4 martensite variants should share a common one. That means that each of the three $\{001\}_A$ poles from the corresponding variants should superimpose on the $\{001\}_A$ stereographic projection. It can be seen from **Fig. 5.7** that among all the selected ORs, only

Pitsch relation ensures a common austenite orientation from all the martensite variants, indicating that this OR could be the effective one. To further quantify the mismatch between the closest orientations of austenite calculated from the variants under the 4 ORs, the disorientation angles between every two austenite orientations were calculated and listed in **Table 5.3**. Obviously, under the Pitsch OR, the disorientation angles are the smallest, which confirms that this OR specified as $\{0\bar{1}\bar{1}\}_A$ // $\{2\bar{2}\bar{1}\}_M$ and $<0\bar{1}1>_A$ // $<\bar{1}\bar{2}2>_M$ is the effective OR for the transformation from the austenite to the *4O* modulated martensite.

Table 5.3 Disorientation angles between calculated austenite orientations obtained under different ORs.

Variant Pair	Disorientation angle for different ORs(°)			
	Bain	K-S	N-W	Pitsch
A&*B*	4.53	0.07	2.13	0.07
C&*D*	4.83	0.40	2.30	0.40
A&*C*	4.66	1.86	2.29	0.18
B&*D*	4.69	2.06	2.47	0.28
A&*D*	0.74	2.12	2.67	0.30
B&*C*	0.76	1.80	2.58	0.20

5.6 Correlation between martensitic transformation OR and martensite variant organization

Since the parent austenite and the product *4O* modulated martensite possess the parallel relationship $\{0\bar{1}\bar{1}\}_A$ // $\{2\bar{2}\bar{1}\}_M$ and $<0\bar{1}1>_A$ // $<\bar{1}\bar{2}2>_M$ under the Pitsch relation, each $\{0\bar{1}\bar{1}\}_A$ plane can provide 4 coplanar $\{0\bar{1}\bar{1}\}_A$ - $<0\bar{1}1>_A$ combinations by reversing the sign of the $\{0\bar{1}\bar{1}\}_A$ plane and that of $<0\bar{1}1>_A$ direction, as shown in **Table 5.4**, thus giving rise to 4 distinct martensite variants.

Table 5.4 OR between the original austenite and the 4 variants A_1, B_1, C_1 and D_1 shown in **Fig. 5.3**.

Variant	OR	Variant	OR
A_1	$(\bar{1}01)_A$ // $(2\bar{2}\bar{1})_M$ $[\bar{1}0\bar{1}]_A$ // $[\bar{1}\bar{2}2]_M$	B_1	$(10\bar{1})_A$ // $(2\bar{2}\bar{1})_M$ $[\bar{1}0\bar{1}]_A$ // $[\bar{1}\bar{2}2]_M$
C_1	$(\bar{1}01)_A$ // $(2\bar{2}\bar{1})_M$ $[101]_A$ // $[\bar{1}\bar{2}2]_M$	D_1	$(10\bar{1})_A$ // $(2\bar{2}\bar{1})_M$ $[101]_A$ // $[\bar{1}\bar{2}2]_M$

As the $\{2\bar{2}\bar{1}\}_M$ plane of the 4 variants that result from one common $\{0\bar{1}\bar{1}\}_A$ plane are parallel, these 4 variants are, in fact, those belonging to one variant plate. According to the symmetry of cubic crystal system, there are 6 equivalent $\{0\bar{1}\bar{1}\}_A$ planes, hence one original austenite can produce 6 groups of 4 martensite variants (in total 24 variants) that correspond to the 6 distinct variant plates revealed by the above microstructural analyses.

With the determined OR between the austenite and the martensite, the interface between the plates in each sub-colony can be correlated with the plane of austenite. As revealed by the above experimental results, the plate interface is defined by the plane that is normal to the 180° rotation axis (listed in **Table 5.1**) shared by the corresponding martensite variants in the adjacent plates. Calculations showed that the plate interface corresponds to one of the $\{0\bar{1}\bar{1}\}_A$ planes (with a very small angular deviation of about 0.75°). In fact the three $\{0\bar{1}\bar{1}\}_A$ planes, one corresponding to the plate interface and the other two to the type I twin interfaces in the adjacent plates, are related by 60°. In other words, the three $\{0\bar{1}\bar{1}\}_A$ planes belong to one $<11\bar{1}>$ axis zone. This indicates that the plate interface and the type I twin interfaces in the adjacent plates in one sub-colony are also related by 60°. Due to the cubic symmetry, one $\{0\bar{1}\bar{1}\}_A$ plane can be shared by two $<11\bar{1}>_A$ axis zones. For example $\mathbf{(0\bar{1}1)_A}$, $(10\bar{1})_A$ & $(\bar{1}10)_A$ in $[111]_A$ axis zone and $\mathbf{(0\bar{1}\bar{1})_A}$, $(110)_A$ & $(\bar{1}0\bar{1})_A$ in $[\bar{1}11]_A$ axis zone, as shown in **Fig. 5.8**(a). If we take the $\mathbf{(0\bar{1}1)_A}$ plane, *i.e.* the common plane in the 2 axis zones, as the plate interface in the sub-colony, 2 distinct sub-colonies can be constructed, as illustrated in **Fig. 5.8**(b). Each $\{0\bar{1}\bar{1}\}_A$ group corresponds to one sub-colony and the 2 sub-colonies correspond to one plate colony as defined above.

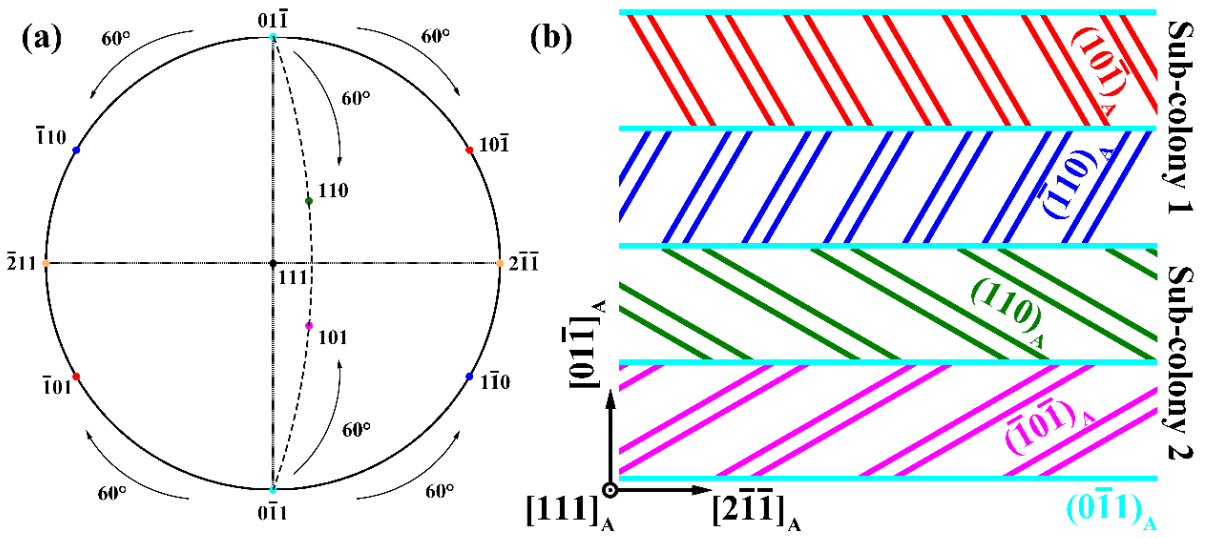

Fig. 5.8 (a) $(111)_A$ standard stereographic projections, where $(0\bar{1}1)_A$, $(10\bar{1})_A$ and $(1\bar{1}0)_A$ planes that are located on the circumference belong to the $[111]_A$ axis zone, whereas the $(0\bar{1}1)_A$, $(110)_A$ and $(101)_A$ planes that are located on the dash arc line belong to the $[\bar{1}11]_A$ axis zone. (b) A microstructural schema of the corresponding plate colony containing two sub-colonies, one being related to the $(0\bar{1}1)_A$, $(10\bar{1})_A$ and $(1\bar{1}0)_A$ group and the other to the $(0\bar{1}1)_A$, $(110)_A$ and $(101)_A$.

This result is completely consistent with the microstructure features observed above. According to the symmetry of the cubic crystal system, we can have 6 equivalent $\{0\bar{1}\bar{1}\}_A$ planes, each of which can be associated with one plate colony. Thus in total, one original austenite grain can produce 6 distinct plate colonies. Our experimental observation has revealed 4 distinct plate colonies. As our microstructure observations were conducted on a two-dimensional sample section, it is possible that there exist 6 distinct plate colonies in the three-dimensional space of one austenite grain. The specific geometrical combination of the martensite plate colony and sub-colony may result from the self-accommodation of elastic strains generated from the structural transformation (from austenite to martensite) and will be thoroughly discussed in Chapter 6. Hereto, the martensitic transformation OR and the associated hierarchical martensite variant organization features of $Ni_{50}Mn_{38}Sb_{12}$ are fully detected that will provide fundamental information for further investigation on property optimization and the crystallography of martensitic transformation of NiMnSb alloys.

5.7 Summary

In this work, the martensitic transformation OR and the martensite variant organization in $Ni_{50}Mn_{38}Sb_{12}$ alloy are investigated. EBSD analysis and crystallographic calculation indicate that the Pitsch OR specified as $\{0\bar{1}\bar{1}\}_A$ // $\{2\bar{2}\bar{1}\}_M$ and $<0\bar{1}1>_A$ // $<\bar{1}\bar{2}2>_M$ is the effective OR for the transformation from the austenite to the *4O* modulated martensite. Under such an OR, 24 martensite variants can be produced during the martensitic transformation. All these variants can form 6 different plates and each plate contains 4 distinct variants. Plates are hierarchically organized into sub-colonies and sub-colonies to plate colonies. Each sub-colony contains 2 distinct plates having in total 8 distinct variants. The interfaces of the lamellar variants having type I twin relation in the adjacent plates and the common plate interface in the sub-colony correspond to three $\{0\bar{1}\bar{1}\}_A$ planes that are related by 60° and belonging to one $<11\bar{1}>_A$ axis zone. 2 distinct sub-colonies form a plate colony that contains 16 distinct variants. One original austenite grain can produce at most 6 different plate colonies in theory. All these results provide basic information for NiMnSb alloys and could be useful for interpreting their magnetic and mechanical characteristics associated with the martensitic transformation and further investigation on martensitic transformation crystallography of these alloys.

Chapter 6 Self-accommodation character of martensitic transformation and its impact on microstructure

6.1 Introduction

In the last two chapters, the crystallographic and morphological characteristics of the orthorhombic NiMnSb martensite and the crystallographic correlations between martensite variants and between variant colonies have been discussed in detail. All these features are closely related to the martensitic transformation. However, the underlying mechanisms of the formation of this kind of microstructure and its correlation with the martensitic transformation have not been studied. To investigate this, a ternary $Ni_{50}Mn_{37}Sb_{13}$ alloy whose martensitic transformation temperature is near the room temperature was used in this chapter. Since this alloy is in a dual phase state at room temperature, fruitful morphological and crystallographic features can be directly observed and detected. Then in the frame of the theory of martensitic transformation crystallography and the crystallographic calculations and analyses, the formation mechanism and the morphological and crystallographic features of this orthorhombic NiMnSb martensite microstructure are thoroughly investigated.

6.2 Experimental

In this chapter, a polycrystalline NiMnSb alloy with nominal composition $Ni_{50}Mn_{37}Sb_{13}$ (at. %) was used. The detailed information on sample preparation can be found in Chapter 2. The transformation temperatures were detected by DSC. The lattice constants of the constituent phases were measured by XRD at the temperature range from 333 K to 213 K. The microstructural and crystallographic features were investigated by SEM-EBSD.

6.3 Results

6.3.1 Martensitic transformation temperatures and crystal structures of $Ni_{50}Mn_{37}Sb_{13}$

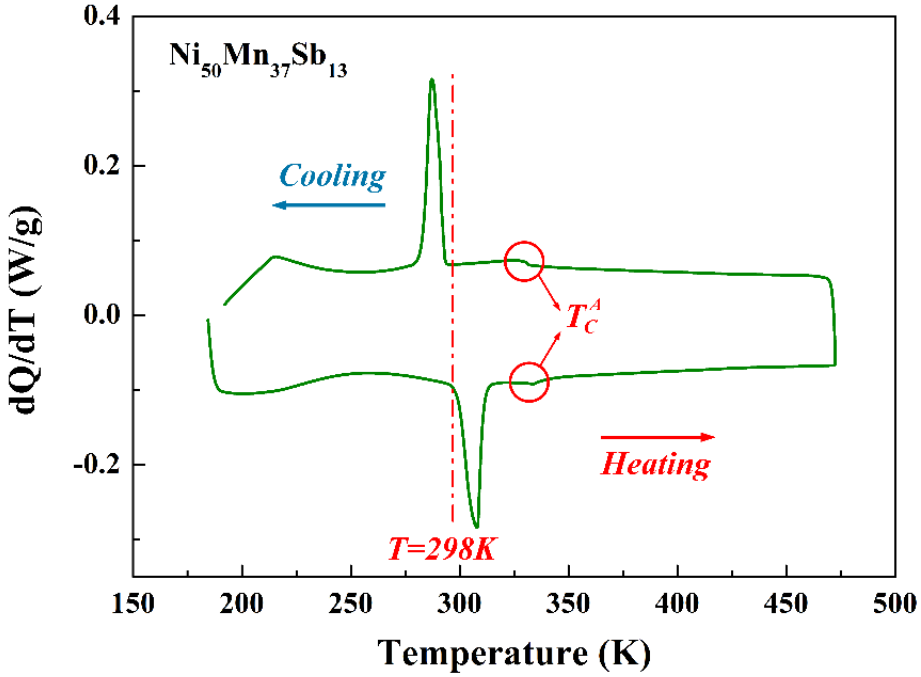

Fig. 6.1 Cooling and heating DSC curves of $Ni_{50}Mn_{37}Sb_{13}$ alloy.

Fig. 6.1 displays the heating and cooling DSC curves of the $Ni_{50}Mn_{37}Sb_{13}$ alloy. Similar to that of the $Ni_{50}Mn_{38}Sb_{12}$ alloy in Chapter 4, both the forward and the reverse martensitic transformations (shown as two sharp peaks in **Fig. 6.1**) and the magnetic transformation of austenite state (shown as two small steps in **Fig. 6.1**) can be detected. Thus, the five characteristic temperatures (M_s, M_f, A_s, A_f and T_C^A) are determined using the tangent method. The results are summarized in **Table 6.1**. Comparing with the transformation temperatures of the $Ni_{50}Mn_{38}Sb_{12}$ alloy from Chapter 4, we can find that with the addition of Sb, the martensitic transformation temperatures are lowered by about 20 ~ 30K, whereas the Curie temperature of the austenite T_C^A remains almost unchanged. Thus at room temperature, as indicated by the red dot-dash line in **Fig. 6.1**, austenite is retained for the present alloy.

Table 6.1 Forward and reverse martensitic transformation temperatures (M_s, M_f, A_s and A_f) and magnetic transformation temperature T_C^A of $Ni_{50}Mn_{37}Sb_{13}$ alloy determined from DSC data (K).

Component	*Ms*	M_f	A_s	A_f	T_C^A
$Ni_{50}Mn_{37}Sb_{13}$	292.39	282.85	299.37	311.63	332.95

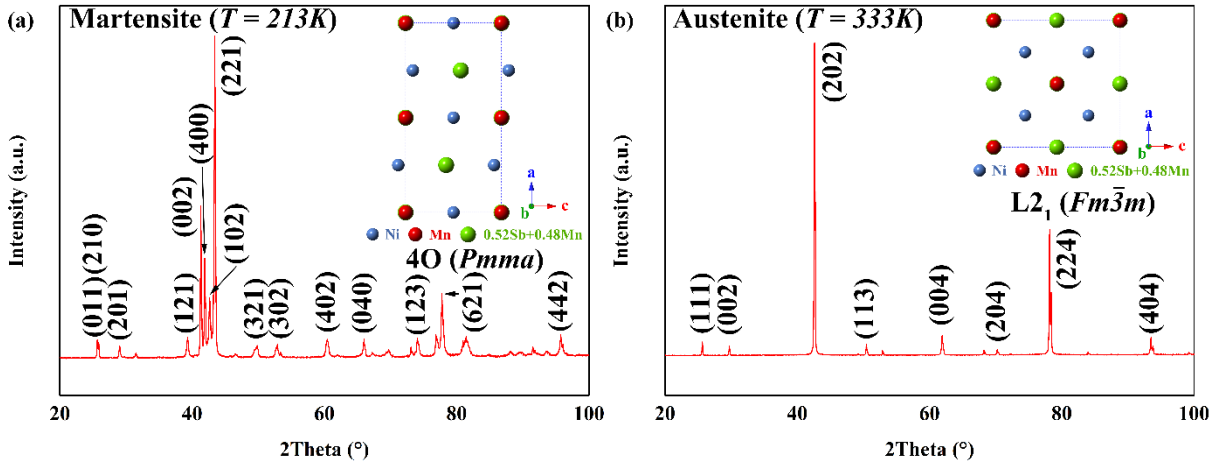

Fig. 6.2 XRD patterns of $Ni_{50}Mn_{37}Sb_{13}$ alloy measured at martensite and austenite state, respectively: (a) T = 213 K and (b) T = 333 K.

Fig. 6.2 shows the XRD patterns of the $Ni_{50}Mn_{37}Sb_{13}$ alloy measured at 213 K (pure martensite state) and 333 K (pure austenite state). Using the published structure models of austenite (cubic in space group $Fm\bar{3}m$ (No. 225) [79]) and martensite (*4O* in space group *Pmma* (No. 051) [79]) of NiMnSb alloys, all the diffraction peaks of the two phases are properly indexed, confirming that the present austenite has a cubic $L2_1$ structure belonging to the space group $Fm\bar{3}m$ (No. 225) and the martensite possesses a *4O* crystal structure belonging to the space group *Pmma* (No. 051). The lattice parameters determined from the diffraction patterns are a_A = 5.9749 Å for austenite, and a_M = 8.5830 Å, b_M = 5.6533 Å, and c_M = 4.3501 Å for martensite.

6.3.2 Microstructure

6.3.2.1 Intragranular martensite

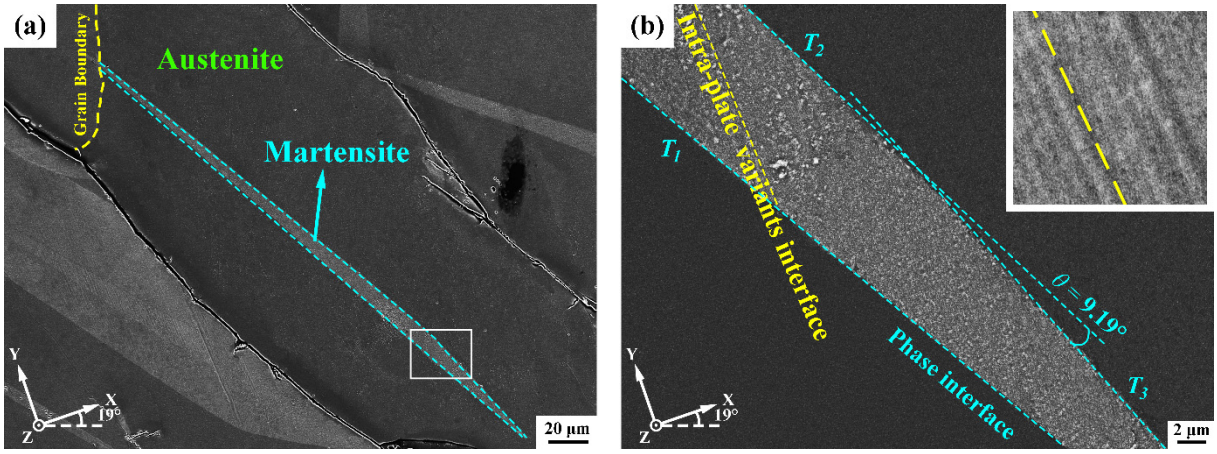

Fig. 6.3 (a) BSE micrographs of one martensite colony in an austenite grain. The phase interfaces are outlined with the light blue dash lines. (b) The magnified micrograph of the zone enclosed in the white rectangle in (a). The inset shows the alternately distributed lamellae with two contrasts. The lamellar interface is outlined with the yellow dash lines. The three differently oriented phase interfaces are denoted T_1, T_2 and T_3.

Fig. 6.3(a) shows a typical BSE micrograph of an austenite grain partially transformed to martensite. It can be seen that martensite (with lighter contrast) are formed intragranularly in the austenite grain (with darker contrast). The martensite colony is in plate shape, enveloped in three differently oriented phase interfaces, and outlined with the light blue dash lines in **Fig. 6.3**(a). In order to investigate the phase interfaces (habit planes) and the interior microstructure of martensite, we choose a zone that contains three differently oriented phase interfaces, as marked with the white rectangle in **Fig. 6.3**(a) for further crystallographic analyses. The magnified BSE micrograph of this zone is shown in **Fig. 6.3**(b). It can be seen that the martensite is composed of fine martensite lamellae with two contrasts and distributed alternately, as shown in the inset of **Fig. 6.3**(b). The lamellar interface is marked with the yellow dash lines in the figure. The three differently oriented phase interfaces are labeled with T_1, T_2 and T_3, respectively.

Then we manually measured the orientations of the martensite lamellae and the austenite around the martensite colony. Along each interface, two distinct martensite variants can be

detected (V_1 and V_1' for T_1, V_2 and V_2' for T_2, and V_3 and V_3' for T_3). Of the two variants, one is much thicker (denoted V_i) than the other (denoted V_i'). The details of the orientation information are given in **Table 6.2**.

Table 6.2 Orientation information of lamellar martensite variants and the adjacent austenite determined by EBSD.
(The Euler angles listed in the table below represent the mean orientation of the martensite variants and the austenite, respectively.)

Position	Euler angle (φ_1 Φ φ_2) (°)		
	Austenite	Martensite	
		Major variant	Minor variant
T_1	Aus_1 (103.5 41.6 36.8)	V_1 (67.0 73.5 56.0)	V_1' (19.8 25.9 22.9)
T_2	Aus_2 (105.1 42.3 35.2)	V_2 (65.9 72.9 56.3)	V_2' (130.0 80.0 113.2)
T_3	Aus_3 (103.8 42.0 35.9)	V_3 (66.4 73.2 55.9)	V_3' (130.5 79.6 113.0)

It is seen that V_1, V_2 and V_3 are the same variants. The small deviation in the Euler angles is either from measurement imprecision or from local lattice distortion. Similarly, V_2' and V_3' are also the same variants. Thus in total, there are three distinct variants in the martensite colony (V_1, V_1' and V_2'). With the measured orientations of the three pairs of variants, we calculate the misorientation between each pair. Calculations show that all of the three pairs, each possesses at least one 180° rotation, as listed in **Table 6.3**. Comparing these 180° rotations with what we have determined in $Ni_{50}Mn_{38}Sb_{12}$ alloy in Chapter 4, we found that the variant pair near T_1 (V_1 and V_1') possesses the type I twin relationship and the pair near T_2 and T_3 (V_2 and V_2' or V_3 and V_3') the type II twin relationship. Following the conventional terminology on martensite variants in NiMn-based alloys (*A*, *B*, *C* and *D*), we found that variant V_1 corresponds to variant *A*, V_1' to *C*, and V_2' to *B*. However, in the intragranular martensite colony in the present alloy, variant *D* was not detected. Either it has not appeared at beginning of the martensitic transformation or its volume fraction is too small beyond the detection resolution.

Table 6.3 Misorientation and twin relationships between the measured variants.

Variant pair	V_1 and V_1'	V_2 and V_2'	V_3 and V_3'
Misorientation angle ω (°)	179.9079	179.4205	179.6801
Rotation axis ***d***	$[\bar{1}\ \overline{2.2755}\ 1.9431]_M$ 0.34° from $(\bar{2}\bar{2}1)_M$ normal	$[1\ \overline{2.0288}\ \overline{1.9969}]_M$ 0.43° from $[1\bar{2}\bar{2}]_M$	$[\bar{1}\ 2.0191\ 1.9876]_M$ 0.38° from $[\bar{1}22]_M$
Twin type	Type I	Type II	Type II

The OR between austenite and martensite was further verified using the Pitsch relation ($\{0\bar{1}\bar{1}\}_A$ // $\{2\bar{2}\bar{1}\}_M$ and $<0\bar{1}1>_A$ // $<\bar{1}\bar{2}2>_M$) that was identified for the $Ni_{50}Mn_{38}Sb_{12}$ alloy in Chapter 5. That material possesses a similar composition with the present alloy, $Ni_{50}Mn_{37}Sb_{13}$. Result shows that the Pitsch relation is also obeyed by the martensite variants with respect to the surrounding austenite in the present alloy, as shown by the corresponding OR plane and OR direction pole figures of the two phases in **Fig. 6.4**. It can be seen that the three variants share one $\{2\bar{2}\bar{1}\}_M$ plane, as enclosed in the red square that are parallel to the $(110)_A$ plane of austenite and the three variants also share one $<\bar{1}\bar{2}2>_M$ direction, as enclosed in the green square, that are parallel to the $[\bar{1}10]_A$ direction of austenite.

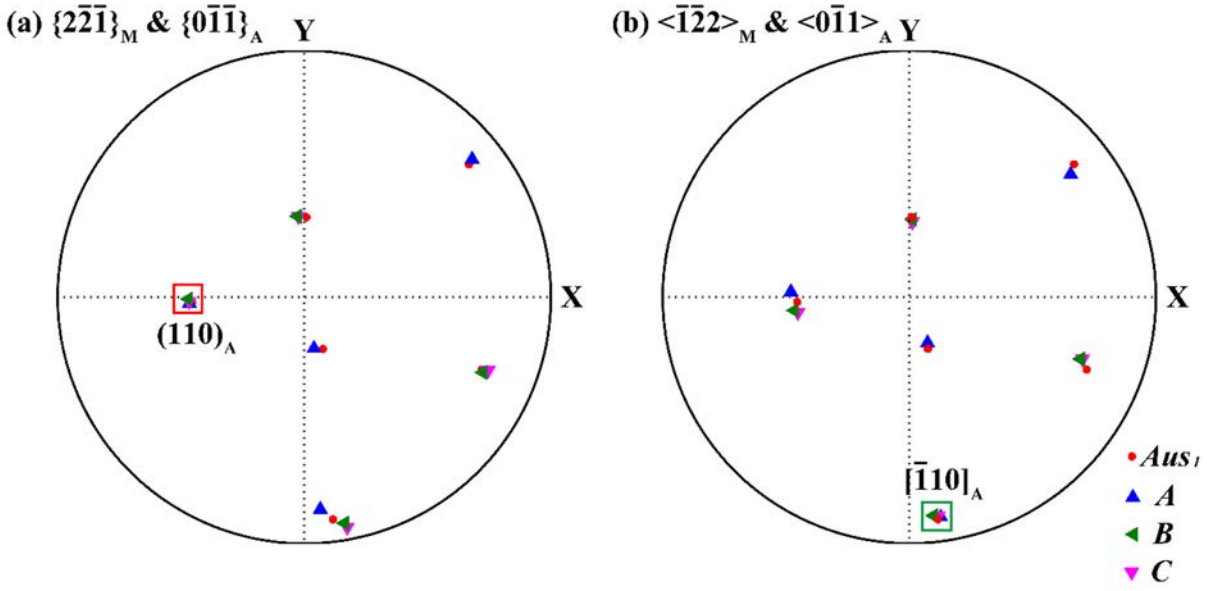

Fig. 6.4 (a) $\{2\bar{2}\bar{1}\}_M$ stereographic projection of the three measured martensite variants *A*, *B* and *C*, and the $\{0\bar{1}\bar{1}\}_A$ stereographic projection of the measured austenite *Aus*$_1$. (b) $<\bar{1}\bar{2}2>_M$ stereographic projection of the three measured martensite variants *A*, *B* and *C*, and the $<0\bar{1}1>_A$ stereographic projection of the measured austenite *Aus*$_1$.

6.3.2.2 Intergranular martensite

Martensite colonies was also found to form from austenite grain boundaries. **Fig. 6.5**(a_1) shows a typical BSE micrograph of two martensite colonies separated by a midrib plane (marked with the orange dash line) formed from the grain boundary of the austenite.

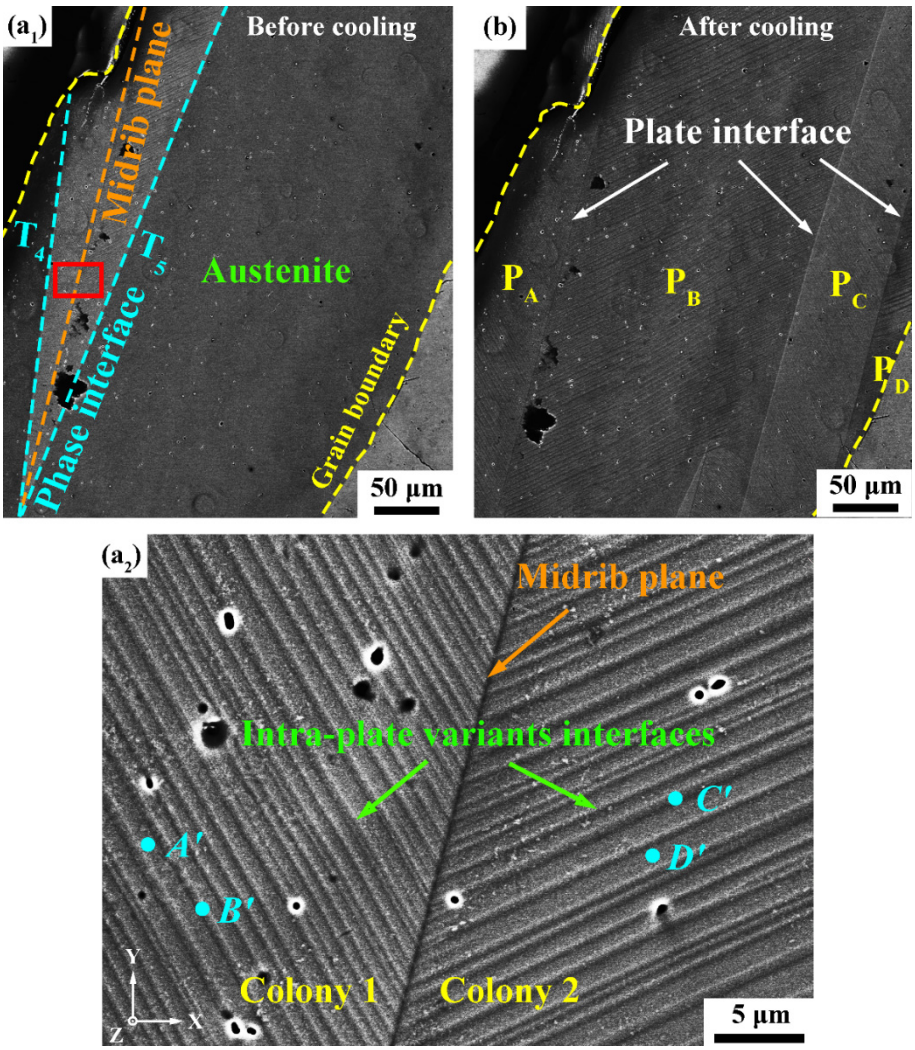

Fig. 6.5 (a_1) BSE micrograph of grain boundary martensite colonies and (a_2) the magnified micrograph displaying fine lamellar martensite in the area enclosed in the red rectangle in (a_1). (b) BSE micrograph acquired in the same area after the sample was further cooled to 283K for 2h.

It can be seen that the two colonies form a wedge-shaped zone. The phase interfaces (marked with blue dash lines, T_4 and T_5), the midrib plane and the intra-plate variants interfaces (shown in **Fig. 6.5**(a_2)) can be easily observed. The martensite lamellae on the two sides of the midrib plane stretch in different directions. Hereafter we denote the colony on the left side of the midrib plane Colony 1 and that on the right side Colony 2, as noted in **Fig. 6.5**(a_2). In order to observe the morphology evolution of the martensite colonies, we cooled the sample to 283K that is close to the M_f of the alloy (282.85K) and kept it for 2h to allow part of the austenite to transform to martensite. The BSE micrograph taken at the same sample area is shown in **Fig.**

6.5(b). It can be seen that the martensite colonies are enlarged by pushing forward the habit planes T_4 and T_5. After transformation the wedge-shaped martensite colonies were transformed to plate-shaped colonies (P_A and P_B in the figure) until they meet the plate-shaped colonies from the neighboring wedges (P_C and P_D in the figure). After the transformation, the phase interfaces T_4 and T_5 disappeared but the midrib plane remain stationary. The disappeared habit plane T_4 and T_5 are replaced by the plate interfaces having the same trace orientation as that of the midrib plane. According to the intra-plate variant trace orientation, we can deduce that plates P_A and P_C are composed of the same martensite variants; so are plates P_B and P_D. Thus in the area boarded by the austenite grain boundaries (the yellow lines) in **Fig. 6.5**(b) there are two distinct plate colonies alternately repeated in the area. These martensite plates are the constituents of the sub-colony found in Chapter 5. This implies that the sub-colonies are composed of the same martensite wedges formed at the beginning of martensite transformation and the final plate interfaces are the midrib planes.

EBSD orientation measurements conducted in the two colonies in the wedge-shaped zone demonstrate that there are in total 4 distinct variants *A′*, *B′*, *C′* and *D′*. Each fine lamella shown in **Fig. 6.5**(a_2) corresponds to one martensite variant. Each colony possesses 2 distinct variants distributed alternately. According to the acquired orientations we calculate the misorientation between variant pairs *A′* and *B′*, and *C′* and *D′*. It is found that both of the two variant pairs possess a type II twin relationship. The related crystallographic information is given in **Table 6.4**.

Table 6.4 Twin information of the two variant pairs in Colony 1 and Colony 2 in **Fig. 6.5**.

Variant pairs	*A′* and *B′*	*C′* and *D′*
Colony	Colony 1	Colony 2
Phase interface	T_4	T_5
Misorientation angle ω (°)	179.6252	179.5053
Rotation axis ***d***	$[1\ \overline{2.0075}\ 2.0103]_M$ 0.11° from $[122]_M$	$[\bar{1}\ 2.0140\ \overline{1.9823}]_M$ 0.38° from $[\bar{1}2\bar{2}]_M$
Twin type	Type II	Type II

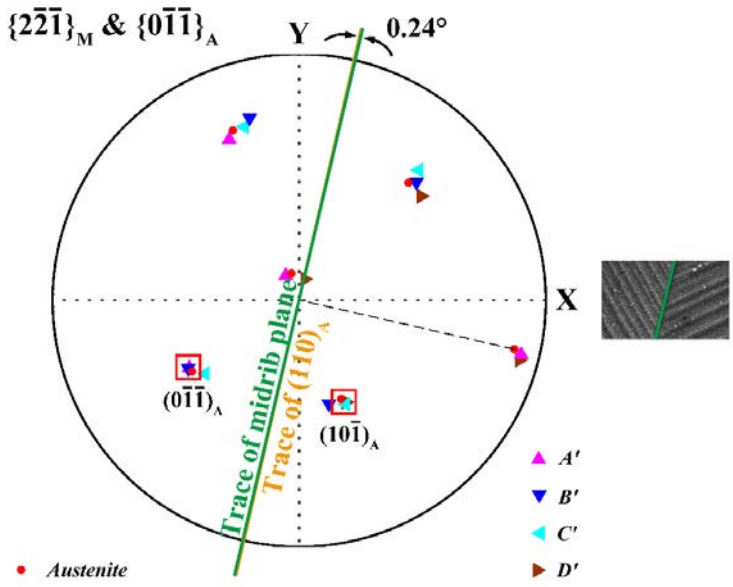

Fig. 6.6 $\{2\bar{2}\bar{1}\}_M$ stereographic projection of variants *A′*, *B′*, *C′* and *D′*, and the $\{0\bar{1}\bar{1}\}_A$ stereographic projection of austenite.

Similarly, we studied the crystallographic coincidence between the martensite variants connected by the midrib plane (inter-colony variants) and with the austenite. As shown by the stereographic projection of $\{2\bar{2}\bar{1}\}_M$ planes of the 4 variants and the stereographic projection of the $\{0\bar{1}\bar{1}\}_A$ planes of austenite in **Fig. 6.6**, we found that variants *A′* and *B′* in Colony 1 share a common $(2\bar{2}\bar{1})_M$ plane and these two planes are parallel to the $(0\bar{1}\bar{1})_A$ plane of austenite. The same relations were also found for variants *C′* and *D′*. The two variants share a common $(2\bar{2}\bar{1})_M$ plane and these planes are parallel to the $(10\bar{1})_A$ plane of austenite. The $(2\bar{2}\bar{1})_M$ planes of the 4 variants are their corresponding twinning plane of type I twin. Moreover, we find that the trace of the $(110)_A$ plane of austenite is almost parallel to the observed trace of the midrib plane (with 0.24° deviation). The three $\{10\bar{1}\}_A$ planes belong to the $[1\bar{1}1]_A$ axis zone.

6.4 Discussion

6.4.1 Sandwich-like martensite and habit plane

The above experimental results show that all the variant colonies possess a sandwich structure, *i.e.*, the colonies are composed of lamellar shaped variants and the variants appear repeatedly in the colonies. It is known that martensitic transformation is realized by coordinated

movements of the atoms of the parent phase. Hence atomic mismatches may appear at the interface areas between the product phase and the parent phase, depending on the crystal structures of the two phases, as illustrated in **Fig. 6.7**(a). Such mismatches induce a kind of resistance to the transformation and the resistance increases with the growth of the new phase. Thus minimization of the elastic strain at the interface region by forming another variant usually happens. As the crystal is still distorted in the area between the phase interface and the variant interfaces, as shown in **Fig. 6.7**(b), the thickness of the lamellar variants are restricted. Thus the transformation is realized by repeated formation of the lamellar variants by forming the so-called sandwich structure, as illustrated in **Fig. 6.7**(b). By adjusting the volume fraction of the two variants, the interface between the two phases or the so-called habit plane could be invariant in macroscopic scale. Thus martensitic transformation is realized by an invariant plane strain.

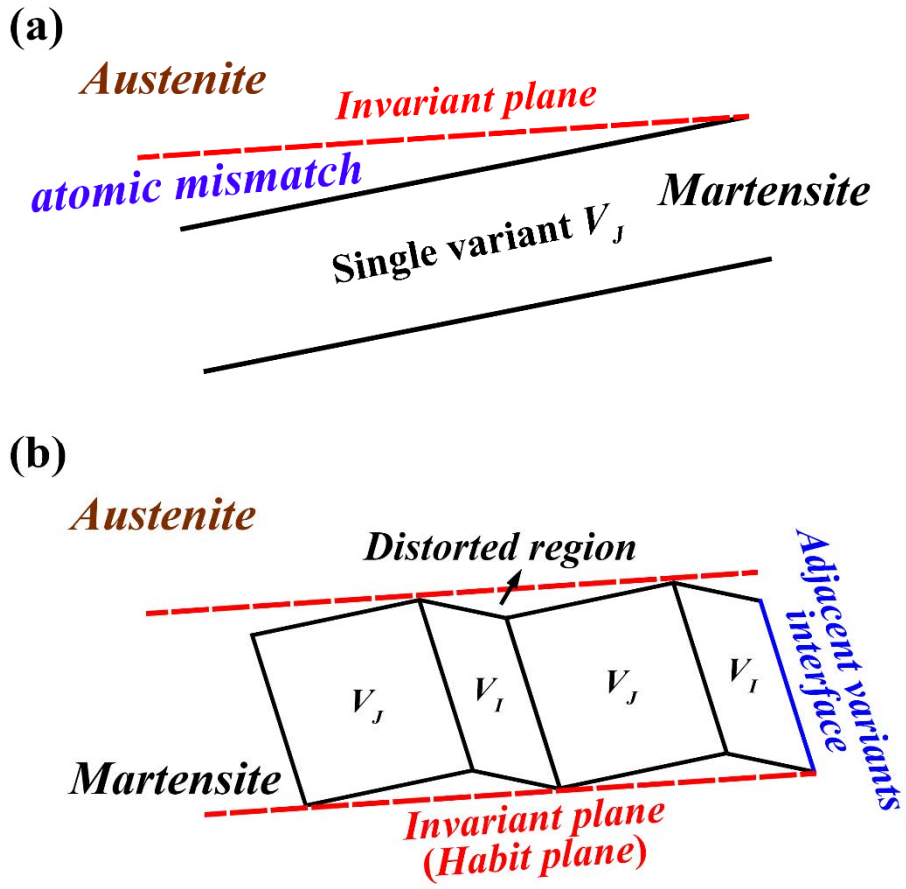

Fig. 6.7 Illustration of the (a) atomic incompatibility between the two phases for the single variant situation and (b) sandwich-like microstructure composed of two martensite variants V_J and V_I to achieve an invariant plane of the phase interface (habit plane).

It is also known that the structure deformation to realize martensitic transformation can be described by a stretch distortion, *i.e.* the Bain distortion, as illustrated in **Fig. 6.8**, and a pure rotation. If the habit plane is invariant, one of the three principal strains of Bain distortion, *i.e.* the three eigenvalues of the Bain distortion gradient tensor, should be equal to 1. For the present alloy, the three principal strains of Bain distortion are:

$$\begin{aligned} \eta_1 &= a_M/\sqrt{2}a_A = 1.0158 \\ \eta_2 &= b_M/a_A = 0.9462 \\ \eta_3 &= \sqrt{2}c_M/a_A = 1.0296. \end{aligned} \tag{6.1}$$

None of the three eigenvalues is equal to 1. Thus the phase interface is not invariant by forming only one martensite variant. Atomic mismatches can be expected, especially when the variant enlarges its volume. Hence, a second variant is needed to accommodate the elastic strains generated by the first variant at the interface regions. The appearance of sandwich structured martensite colonies observed in the present alloy (**Fig. 6.3** and **Fig. 6.5**) should be for achieving an invariant plane at the phase interface.

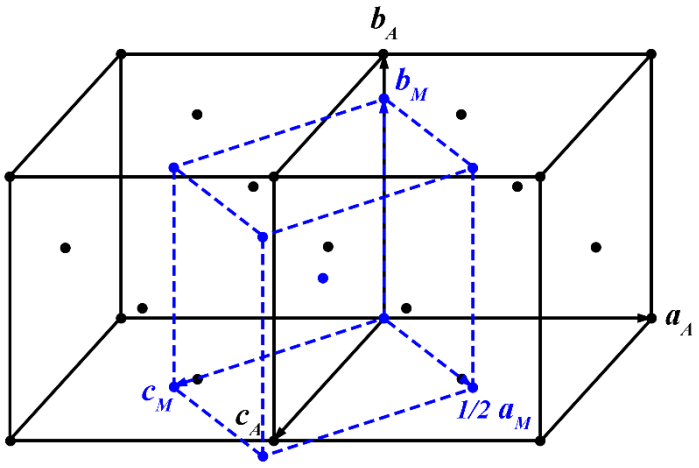

Fig. 6.8 Illustration of the Bain distortion from a cubic lattice to orthorhombic lattice. The black and blue points represent the Bravais lattice points of austenite and martensite, respectively.

For the present alloy, the martensitic transformation obeys the Pitsch OR ($\{0\bar{1}\bar{1}\}_A$ // $\{2\bar{2}\bar{1}\}_M$ and $<0\bar{1}1>_A$ // $<\bar{1}\bar{2}2>_M$), 24 martensite variants in terms of crystallographic orientation can be produced within one initial austenite grain. Under a stress free environment, the 24

variants should have equal chance to appear. However, in the present alloy, only 2 variants with twin relation were detected in the vicinity of the habit plane for both intragranular transformation and intergranular transformation. Therefore the occurrence of the variants is not arbitrary, but selective. To find out the selection rule, we need to know how lattice is deformed during the transformation. In fact, the formation of each possible variant represents a specifically oriented lattice distortion of the parent austenite. By the examining lattice correspondences between the parent austenite and the product martensite under the Pitsch OR, as shown in **Fig. 6.9**, the deformation gradient tensor to form the martensite variant, F_{or} in the OR frame, can be constructed as below:

$$F_{OR} = \begin{pmatrix} 0.9854 & -0.0102 & -0.0776 \\ 0 & 1.0234 & 0.0090 \\ 0 & 0 & 0.9823 \end{pmatrix}. \tag{6.2}$$

It can be further expressed in the Bravais lattice basis of austenite by coordinate transformation:

$$F_0 = \begin{pmatrix} 1.0234 & 0.0064 & 0.0064 \\ -0.0072 & 0.9450 & -0.0403 \\ 0.0072 & 0.0372 & 1.0226 \end{pmatrix}. \tag{6.3}$$

Thus the deformation gradient tensors of the 24 variants can be calculated with the following equation:

$$F_i = S_A^i \times F_0 \times \left(S_A^i\right)^{-1} \ (i = 1\sim24), \tag{6.4}$$

where S_A^i is the rotational symmetry elements of the cubic crystal system.

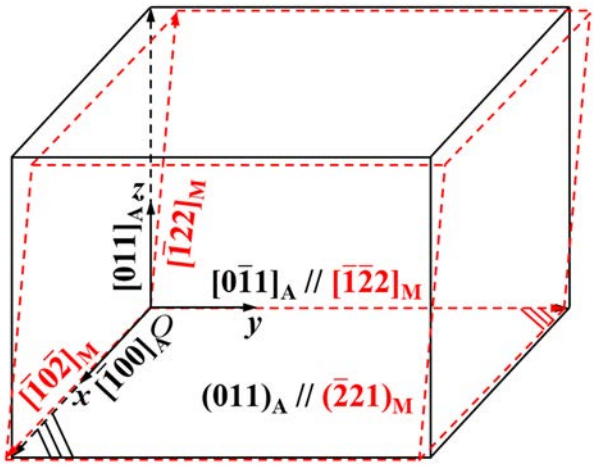

Fig. 6.9 Lattice correspondences between the parent austenite and the product martensite under the Pitsch OR.

The calculated deformation gradient tensors of the 24 variants of the present alloy are listed in **Table 6.5**. According to the phenomenology theory of martensitic transformation [109, 110], the transformation deformation can be decomposed into a stretch distortion represented with a Hermitian matrix *U*, *i.e.* the Bain distortion, and a pure rotation represented with a unitary matrix *R*, as mentioned above:

$$F = RU. \tag{6.5}$$

By polar decomposition theorem [121], U and R can be resolved. The stretch distortion U and the rotation R were further calculated for all the 24 variants and also listed in **Table 6.5**.

Table 6.5 Deformation gradient tensor F_i, stretch tensor or Bain distortion U_i, rotation matrix R_i of martensite variant i obeying Pitsch OR and the corresponding OR between the variant and the parent austenite.

Variant i	Deformation gradient tensor F_i	Bain distortion U_i	Rotation matrix R_i	OR
1	$\begin{pmatrix} 1.02338 & 0.00639 & 0.00639 \\ -0.00720 & 0.94504 & -0.04034 \\ 0.00720 & 0.03724 & 1.02262 \end{pmatrix}$	$\begin{pmatrix} 1.02341 & 0 & 0.00693 \\ 0 & 0.94579 & 0 \\ 0.00693 & 0 & 1.02341 \end{pmatrix}$	$\begin{pmatrix} 0.99998 & 0.00675 & -0.00053 \\ -0.00677 & 0.99920 & -0.03937 \\ 0.00027 & 0.03937 & 0.99922 \end{pmatrix}$	$(0\bar{1}\bar{1})_A$ // $(2\bar{2}\bar{1})_M$ $[0\bar{1}1]_A$ // $[\bar{1}\bar{2}2]_M$
7	$\begin{pmatrix} 1.02338 & -0.00639 & -0.00639 \\ 0.00720 & 0.94504 & -0.04034 \\ -0.00720 & 0.03724 & 1.02262 \end{pmatrix}$	$\begin{pmatrix} 1.02341 & 0 & -0.00693 \\ 0 & 0.94579 & 0 \\ -0.00693 & 0 & 1.02341 \end{pmatrix}$	$\begin{pmatrix} 0.99998 & -0.0675 & 0.00053 \\ 0.00677 & 0.99920 & -0.03937 \\ -0.00027 & 0.03937 & 0.99922 \end{pmatrix}$	$(011)_A$ // $(2\bar{2}\bar{1})_M$ $[01\bar{1}]_A$ // $[\bar{1}\bar{2}2]_M$
21	$\begin{pmatrix} 1.02338 & -0.00639 & -0.00639 \\ -0.00720 & 1.02262 & 0.03724 \\ 0.00720 & -0.04034 & 0.94504 \end{pmatrix}$	$\begin{pmatrix} 1.02341 & -0.00693 & 0 \\ -0.00693 & 1.02341 & 0 \\ 0 & 0 & 0.94579 \end{pmatrix}$	$\begin{pmatrix} 0.99998 & 0.00053 & -0.00675 \\ -0.00027 & 0.99922 & 0.03937 \\ 0.00677 & -0.03937 & 0.99920 \end{pmatrix}$	$(0\bar{1}\bar{1})_A$ // $(2\bar{2}\bar{1})_M$ $[01\bar{1}]_A$ // $[\bar{1}\bar{2}2]_M$
24	$\begin{pmatrix} 1.02338 & 0.00639 & 0.00693 \\ 0.00720 & 1.02262 & 0.03724 \\ -0.00720 & -0.04034 & 0.94501 \end{pmatrix}$	$\begin{pmatrix} 1.02341 & 0.00693 & 0 \\ 0.00693 & 1.02341 & 0 \\ 0 & 0 & 0.94579 \end{pmatrix}$	$\begin{pmatrix} 0.99998 & -0.00053 & 0.00675 \\ 0.00027 & 0.99922 & 0.03937 \\ -0.00677 & -0.03937 & 0.99920 \end{pmatrix}$	$(011)_A$ // $(2\bar{2}\bar{1})_M$ $[0\bar{1}1]_A$ // $[\bar{1}\bar{2}2]_M$
2	$\begin{pmatrix} 1.02262 & 0.03724 & 0.00720 \\ -0.04034 & 0.94504 & -0.00720 \\ 0.00639 & 0.00639 & 1.02338 \end{pmatrix}$	$\begin{pmatrix} 1.02341 & 0 & 0.00693 \\ 0 & 0.94579 & 0 \\ 0.00693 & 0 & 1.02341 \end{pmatrix}$	$\begin{pmatrix} 0.99922 & 0.03937 & 0.00027 \\ -0.03937 & 0.99920 & -0.00677 \\ 0.00053 & -0.00675 & 0.99998 \end{pmatrix}$	$(1\bar{1}0)_A$ // $(2\bar{2}\bar{1})_M$ $[\bar{1}10]_A$ // $[\bar{1}\bar{2}2]_M$
3	$\begin{pmatrix} 1.02262 & 0.03724 & -0.00720 \\ -0.04034 & 0.94504 & 0.00720 \\ -0.00639 & -0.00639 & 1.02338 \end{pmatrix}$	$\begin{pmatrix} 1.02341 & 0 & -0.00693 \\ 0 & 0.94579 & 0 \\ -0.00693 & 0 & 1.02341 \end{pmatrix}$	$\begin{pmatrix} 0.99922 & 0.03937 & -0.00027 \\ -0.03937 & 0.99920 & 0.00677 \\ 0.00053 & -0.00675 & 0.99998 \end{pmatrix}$	$(\bar{1}\bar{1}0)_A$ // $(2\bar{2}\bar{1})_M$ $[1\bar{1}0]_A$ // $[\bar{1}\bar{2}2]_M$
12	$\begin{pmatrix} 0.94504 & -0.04034 & -0.00720 \\ 0.03724 & 1.02262 & 0.00720 \\ 0.00639 & 0.00639 & 1.02338 \end{pmatrix}$	$\begin{pmatrix} 0.94579 & 0 & 0 \\ 0 & 1.02341 & 0.00693 \\ 0 & 0.00693 & 1.02341 \end{pmatrix}$	$\begin{pmatrix} 0.99920 & -0.03937 & -0.00677 \\ 0.03937 & 0.99922 & 0.00027 \\ 0.00675 & -0.00053 & 0.99998 \end{pmatrix}$	$(\bar{1}\bar{1}0)_A$ // $(2\bar{2}\bar{1})_M$ $[\bar{1}10]_A$ // $[\bar{1}\bar{2}2]_M$
18	$\begin{pmatrix} 0.94504 & -0.04034 & 0.00720 \\ 0.03724 & 1.02262 & -0.00720 \\ -0.00639 & -0.00639 & 1.02338 \end{pmatrix}$	$\begin{pmatrix} 0.94579 & 0 & 0 \\ 0 & 1.02341 & -0.00693 \\ 0 & -0.00693 & 1.02341 \end{pmatrix}$	$\begin{pmatrix} 0.99920 & -0.03937 & 0.00677 \\ 0.03937 & 0.99922 & -0.00027 \\ -0.00675 & 0.00053 & 0.99998 \end{pmatrix}$	$(1\bar{1}0)_A$ // $(2\bar{2}\bar{1})_M$ $[1\bar{1}0]_A$ // $[\bar{1}\bar{2}2]_M$

Table 6.5 (*continued*)

Variant i	Deformation gradient tensor F_i	Bain distortion U_i	Rotation matrix R_i	OR
4	$\begin{pmatrix}1.02338 & -0.00639 & 0.00639\\ 0.00720 & 0.94504 & 0.04034\\ 0.00720 & -0.03724 & 1.02262\end{pmatrix}$	$\begin{pmatrix}1.02341 & 0 & 0.00693\\ 0 & 0.94579 & 0\\ 0.00693 & 0 & 1.02341\end{pmatrix}$	$\begin{pmatrix}0.99998 & -0.00675 & -0.00053\\ 0.00677 & 0.99920 & 0.03937\\ 0.00027 & -0.03937 & 0.99922\end{pmatrix}$	$(0\bar{1}1)_A$ // $(2\bar{2}\bar{1})_M$ $[0\bar{1}\bar{1}]_A$ // $[\bar{1}\bar{2}2]_M$
6	$\begin{pmatrix}1.02338 & 0.00639 & -0.00639\\ 0.00720 & 1.02262 & -0.03724\\ 0.00720 & 0.04034 & 0.94504\end{pmatrix}$	$\begin{pmatrix}1.02341 & 0.00693 & 0\\ 0.00693 & 1.02341 & 0\\ 0 & 0 & 0.94579\end{pmatrix}$	$\begin{pmatrix}0.99998 & -0.00053 & -0.00675\\ 0.00027 & 0.99922 & -0.03937\\ 0.0067 & 0.03937 & 0.99920\end{pmatrix}$	$(0\bar{1}1)_A$ // $(2\bar{2}\bar{1})_M$ $[011]_A$ // $[\bar{1}\bar{2}2]_M$
8	$\begin{pmatrix}1.02338 & -0.00639 & 0.00639\\ -0.00720 & 1.02262 & -0.03724\\ -0.00720 & 0.04034 & 0.94504\end{pmatrix}$	$\begin{pmatrix}1.02341 & -0.00693 & 0\\ -0.00693 & 1.02341 & 0\\ 0 & 0 & 0.94579\end{pmatrix}$	$\begin{pmatrix}0.99998 & 0.00053 & 0.00675\\ -0.00027 & 0.99922 & -0.03937\\ -0.00677 & 0.03937 & 0.99920\end{pmatrix}$	$(01\bar{1})_A$ // $(2\bar{2}\bar{1})_M$ $[0\bar{1}\bar{1}]_A$ // $[\bar{1}\bar{2}2]_M$
10	$\begin{pmatrix}1.02338 & 0.00639 & -0.00639\\ -0.00720 & 0.94504 & 0.04034\\ -0.00720 & -0.03724 & 1.02262\end{pmatrix}$	$\begin{pmatrix}1.02341 & 0 & -0.00693\\ 0 & 0.94579 & 0\\ -0.00693 & 0 & 1.02341\end{pmatrix}$	$\begin{pmatrix}0.99998 & 0.00675 & 0.00053\\ -0.00677 & 0.99920 & 0.03937\\ -0.00027 & -0.03937 & 0.99922\end{pmatrix}$	$(01\bar{1})_A$ // $(2\bar{2}\bar{1})_M$ $[011]_A$ // $[\bar{1}\bar{2}2]_M$
5	$\begin{pmatrix}1.02262 & -0.03724 & -0.00720\\ 0.04034 & 0.94504 & -0.00720\\ -0.00639 & 0.00639 & 1.02338\end{pmatrix}$	$\begin{pmatrix}1.02341 & 0 & -0.00693\\ 0 & 0.94579 & 0\\ -0.00693 & 0 & 1.02341\end{pmatrix}$	$\begin{pmatrix}0.99922 & -0.03937 & -0.00027\\ 0.03937 & 0.99920 & -0.00677\\ 0.00053 & 0.00675 & 0.99998\end{pmatrix}$	$(1\bar{1}0)_A$ // $(2\bar{2}\bar{1})_M$ $[\bar{1}\bar{1}0]_A$ // $[\bar{1}\bar{2}2]_M$
14	$\begin{pmatrix}0.94504 & 0.04034 & -0.00720\\ -0.03724 & 1.02262 & -0.00720\\ 0.00639 & -0.00639 & 1.02338\end{pmatrix}$	$\begin{pmatrix}0.94579 & 0 & 0\\ 0 & 1.02341 & -0.00693\\ 0 & -0.00693 & 1.02341\end{pmatrix}$	$\begin{pmatrix}0.99920 & 0.03937 & -0.00677\\ -0.03937 & 0.99922 & -0.00027\\ 0.00675 & 0.00053 & 0.99998\end{pmatrix}$	$(1\bar{1}0)_A$ // $(2\bar{2}\bar{1})_M$ $[110]_A$ // $[\bar{1}\bar{2}2]_M$
17	$\begin{pmatrix}0.94504 & 0.04034 & 0.00720\\ -0.03724 & 1.02262 & 0.00720\\ -0.00639 & 0.00639 & 1.02338\end{pmatrix}$	$\begin{pmatrix}0.94579 & 0 & 0\\ 0 & 1.02341 & 0.00693\\ 0 & 0.00693 & 1.02341\end{pmatrix}$	$\begin{pmatrix}0.99920 & 0.03937 & 0.00677\\ -0.03937 & 0.99922 & 0.00027\\ -0.00675 & -0.00053 & 0.99998\end{pmatrix}$	$(\bar{1}10)_A$ // $(2\bar{2}\bar{1})_M$ $[\bar{1}\bar{1}0]_A$ // $[\bar{1}\bar{2}2]_M$
22	$\begin{pmatrix}1.02262 & -0.03724 & 0.00720\\ 0.04034 & 0.94504 & 0.00720\\ 0.00639 & -0.00639 & 1.02338\end{pmatrix}$	$\begin{pmatrix}1.02341 & 0 & 0.00693\\ 0 & 0.94579 & 0\\ 0.00693 & 0 & 1.02341\end{pmatrix}$	$\begin{pmatrix}0.99922 & -0.03937 & 0.00027\\ 0.03937 & 0.99920 & 0.00677\\ -0.00053 & -0.00675 & 0.99998\end{pmatrix}$	$(\bar{1}10)_A$ // $(2\bar{2}\bar{1})_M$ $[110]_A$ // $[\bar{1}\bar{2}2]_M$

Table 6.5 (*continued*)

Variant i	Deformation gradient tensor F_i	Bain distortion U_i	Rotation matrix R_i	OR
9	$\begin{pmatrix} 0.94504 & 0.00720 & -0.04034 \\ -0.00639 & 1.02338 & -0.00639 \\ 0.03724 & -0.00720 & 1.02262 \end{pmatrix}$	$\begin{pmatrix} 0.94579 & 0 & 0 \\ 0 & 1.02341 & -0.00693 \\ 0 & -0.00693 & 1.02341 \end{pmatrix}$	$\begin{pmatrix} 0.99920 & 0.00677 & -0.03937 \\ -0.00675 & 0.99998 & 0.00053 \\ 0.03937 & -0.00027 & 0.99922 \end{pmatrix}$	$(\bar{1}0\bar{1})_A$ // $(2\bar{2}\bar{1})_M$ $[\bar{1}01]_A$ // $[\bar{1}\bar{2}2]_M$
13	$\begin{pmatrix} 1.02262 & 0.00720 & 0.03724 \\ 0.00639 & 1.02338 & 0.00639 \\ -0.04034 & -0.00720 & 0.94504 \end{pmatrix}$	$\begin{pmatrix} 1.02341 & 0.00693 & 0 \\ 0.00693 & 1.02341 & 0 \\ 0 & 0 & 0.94579 \end{pmatrix}$	$\begin{pmatrix} 0.99922 & 0.00027 & 0.03937 \\ -0.00053 & 0.99998 & 0.00675 \\ -0.03937 & -0.00677 & 0.99920 \end{pmatrix}$	$(\bar{1}0\bar{1})_A$ // $(2\bar{2}\bar{1})_M$ $[10\bar{1}]_A$ // $[\bar{1}\bar{2}2]_M$
16	$\begin{pmatrix} 1.02262 & -0.00720 & 0.03724 \\ -0.00639 & 1.02338 & -0.00639 \\ -0.04034 & 0.00720 & 0.94504 \end{pmatrix}$	$\begin{pmatrix} 1.02341 & -0.00693 & 0 \\ -0.00693 & 1.02341 & 0 \\ 0 & 0 & 0.94579 \end{pmatrix}$	$\begin{pmatrix} 0.99922 & -0.00027 & 0.03937 \\ 0.00053 & 0.99998 & -0.00675 \\ -0.03937 & 0.00677 & 0.99920 \end{pmatrix}$	$(101)_A$ // $(2\bar{2}\bar{1})_M$ $[\bar{1}01]_A$ // $[\bar{1}\bar{2}2]_M$
23	$\begin{pmatrix} 0.94504 & -0.00720 & -0.04034 \\ 0.00639 & 1.02338 & 0.00639 \\ 0.03724 & 0.00720 & 1.02262 \end{pmatrix}$	$\begin{pmatrix} 0.94579 & 0 & 0 \\ 0 & 1.02341 & 0.00693 \\ 0 & 0.00693 & 1.02341 \end{pmatrix}$	$\begin{pmatrix} 0.99920 & -0.00677 & -0.03937 \\ 0.00675 & 0.99998 & -0.00053 \\ 0.03937 & 0.00027 & 0.99922 \end{pmatrix}$	$(101)_A$ // $(2\bar{2}\bar{1})_M$ $[10\bar{1}]_A$ // $[\bar{1}\bar{2}2]_M$
11	$\begin{pmatrix} 0.94504 & 0.00720 & 0.04034 \\ -0.00639 & 1.02338 & 0.00639 \\ -0.03724 & 0.00720 & 1.02262 \end{pmatrix}$	$\begin{pmatrix} 0.94579 & 0 & 0 \\ 0 & 1.02341 & 0.00693 \\ 0 & 0.00693 & 1.02341 \end{pmatrix}$	$\begin{pmatrix} 0.99920 & 0.00677 & 0.03937 \\ -0.00675 & 0.99998 & -0.00053 \\ -0.03937 & 0.00027 & 0.99922 \end{pmatrix}$	$(10\bar{1})_A$ // $(2\bar{2}\bar{1})_M$ $[101]_A$ // $[\bar{1}\bar{2}2]_M$
15	$\begin{pmatrix} 1.02262 & 0.00720 & -0.03724 \\ 0.00639 & 1.02338 & -0.00639 \\ 0.04034 & 0.00720 & 0.94504 \end{pmatrix}$	$\begin{pmatrix} 1.02341 & 0.00693 & 0 \\ 0.00693 & 1.02341 & 0 \\ 0 & 0 & 0.94579 \end{pmatrix}$	$\begin{pmatrix} 0.99922 & 0.00027 & -0.03937 \\ -0.00053 & 0.99998 & -0.00675 \\ 0.03937 & 0.00677 & 0.99920 \end{pmatrix}$	$(10\bar{1})_A$ // $(2\bar{2}\bar{1})_M$ $[\bar{1}0\bar{1}]_A$ // $[\bar{1}\bar{2}2]_M$
19	$\begin{pmatrix} 1.02262 & -0.00720 & -0.03724 \\ -0.00639 & 1.02338 & 0.00639 \\ 0.04034 & -0.00720 & 0.94504 \end{pmatrix}$	$\begin{pmatrix} 1.02341 & -0.00693 & 0 \\ -0.00693 & 1.02341 & 0 \\ 0 & 0 & 0.94579 \end{pmatrix}$	$\begin{pmatrix} 0.99922 & -0.00027 & -0.03937 \\ 0.00053 & 0.99998 & 0.00675 \\ 0.03937 & -0.00677 & 0.99920 \end{pmatrix}$	$(\bar{1}01)_A$ // $(2\bar{2}\bar{1})_M$ $[101]_A$ // $[\bar{1}\bar{2}2]_M$
20	$\begin{pmatrix} 0.94504 & -0.00720 & 0.04034 \\ 0.00639 & 1.02338 & -0.00639 \\ -0.03724 & -0.00720 & 1.02262 \end{pmatrix}$	$\begin{pmatrix} 0.94579 & 0 & 0 \\ 0 & 1.02341 & -0.00693 \\ 0 & -0.00693 & 1.02341 \end{pmatrix}$	$\begin{pmatrix} 0.99920 & -0.00677 & 0.03937 \\ 0.00675 & 0.99998 & 0.00053 \\ -0.03937 & -0.00027 & 0.99922 \end{pmatrix}$	$(\bar{1}01)_A$ // $(2\bar{2}\bar{1})_M$ $[\bar{1}0\bar{1}]_A$ // $[\bar{1}\bar{2}2]_M$

It is seen from the table that the 24 distinct deformations represent only 6 distinct stretch distortions. The differentiation between the variant with the same stretch distortion is made by the rotation. In the classical theory of martensitic transformation, U_0 is calculated according to the Bain distortion model:

$$U_0 = \begin{pmatrix} \frac{\eta_1 + \eta_3}{2} & 0 & \frac{\eta_1 - \eta_3}{2} \\ 0 & \eta_2 & 0 \\ \frac{\eta_1 - \eta_3}{2} & 0 & \frac{\eta_1 + \eta_3}{2} \end{pmatrix}. \tag{6.6a}$$

By symmetry operation, all the possible U_i can be calculated:

$$U_i = \left(S_A^i\right)^{-1} U_0 S_A^i \ (i = 1{\sim}24). \tag{6.6b}$$

The uncertainty left by this method is that the true orientation of the variant or the true variant in the microstructure is not known, as the orientation of the variant is determined by the rotation but not only the Bain distortion. Thus the advantages of our method described above are that all the information about the variants in terms of their deformation gradient tenor, Bain distortion and pure rotation is known and their spatial correlation with their microstructure is also known.

If the formation of the sandwich structure is to minimize the transformation strain, the following two conditions should be satisfied. One is that the two variants should cancel out the elastic strains at habit plane to achieve an invariant plane and the other is that they can offer maximum lattice match at their interfaces, as the formation of intra sandwich interfaces represented by an increase of interfacial area also increases the transformation resistance. According to the crystallographic theory of martensitic transformation [107], the two conditions can be mathematically expressed with the following two equations:

$$Q_1 U_J - U_I = \boldsymbol{a_t} \otimes \boldsymbol{n_t} \tag{6.7a}$$

$$Q_2\left(\lambda Q_1 U_J + (1-\lambda) U_I\right) - I = \boldsymbol{a_h} \otimes \boldsymbol{n_h}. \tag{6.7b}$$

Eq. (6.7a) describes the geometrical compatibility of the two variants at variant interfaces and Eq. (6.7b) the geometrical compatibility between the sandwich and the austenite at habit plane. In Eq. (6.7a), U_J and U_I are stretch tensors or Bain distortion corresponding to variant V_J and

V_I; Q_1 is the additional relative rotation between the two variants to keep a minimum atomic mismatches on variant interface; $\boldsymbol{a_t}$ is a vector on the interface; $\boldsymbol{n_t}$ is the vector normal to the interface. In Eq. (6.7b), Q_2 is another additional relative rotation between the sandwich and the retained austenite to keep a minimum atomic mismatches on the habit plane; λ is the volume fraction of V_J; $\boldsymbol{a_h}$ is a vector on the interface between the sandwich and the austenite or the habit plane; $\boldsymbol{n_t}$ is the vector normal to the habit plane. In the two equations, Q_1U_J, U_I, $Q_2\left(\lambda Q_1U_J + (1-\lambda)U_I\right)$ and I are the relative deformation gradient tensors of variant V_J, variant V_I, the sandwich structure and the retained austenite, respectively. Since there is no deformation for the retained austenite, its deformation matrix is the identity matrix I. If the two variants represented by U_I and U_J can provide geometrical compatibility at the two kinds of interfaces, there should exist two vectors for each equation in Eq. (6.7) such that the left side of the equation can be expressed by a dyadic product of the two vectors, one being the interface normal vector and the other a vector on the interface. Thus the variant interface plane and the habit plane can be respectively resolved. To solve the two equations, only U_I and U_J should be known as the initial input. Using the mathematical treatments described in [107], all the other variables can be solved. Hereafter, all the calculations and results are conducted and expressed in the Bravais lattice basis of the cubic austenite, unless specified otherwise.

Table 6.6 Variant pairs that can form a sandwich-like martensite with the best atomic matches on variant interface and habit plane.

Variant pair	Volume fraction	OR	Variant interface	Habit plane	Correspondence with the experimental results
1-24	0.7179-0.2821 0.2821-0.7179	Type II twin	$(1\ 5.3126\ 5.3126)_A$	$(3.6996\ 4.7074\ 1)_A$ $(6.3337\ \overline{7.0982}\ 1)_A$ $(\overline{6.3337}\ \overline{1}\ 7.0982)_A$ $(3.6996\ 1\ 4.7074)_A$	Variant 1 – Variant *A′* Variant 24 – Variant *B′* Twinning plane – $(1\ 5.3126\ 5.3126)_A$ Habit plane T_4 – $(3.6996\ 4.7074\ 1)_A$
7-21	0.7179-0.2821 0.2821-0.7179	Type II twin	$(\overline{1}\ 5.3126\ 5.3126)_A$	$(6.3337\ 7.0982\ \overline{1})_A$ $(3.6996\ \overline{4.7074}\ \overline{1})_A$ $(3.6996\ \overline{1}\ \overline{4.7074})_A$ $(6.3337\ \overline{1}\ 7.0982)_A$	
1-21	0.7201-0.2799 0.2799-0.7201	Type I twin	$(011)_A$	$(3.9838\ 4.4407\ 1)_A$ $(5.0776\ \overline{6.5193}\ 1)_A$ $(3.9838\ \overline{1}\ \overline{4.4407})_A$ $(5.0776\ \overline{1}\ 6.5193)_A$	
7-24	0.7201-0.2799 0.2799-0.7201	Type I twin	$(011)_A$	$(\overline{3.9838}\ 4.4407\ 1)_A$ $(5.0776\ 6.5193\ \overline{1})_A$ $(5.0776\ 1\ \overline{6.5193})_A$ $(3.9838\ 1\ 4.4407)_A$	

Table 6.6 (*continued*)

Variant pair	Volume fraction	OR	Variant interface	Invariant habit plane	Correspondence with the experimental result
2-12	0.7179-0.2821 0.2821-0.7179	Type II twin	$(5.3126\ 5.3126\ 1)_A$	$(1\ \overline{7.0982}\ 6.3337)_A$ $(1\ 4.7074\ 3.6996)_A$ $(4.7074\ 1\ 3.6996)_A$ $(\overline{7.0982}\ 1\ 6.3337)_A$	
3-18	0.7179-0.2821 0.2821-0.7179	Type II twin	$(5.3126\ 5.3126\ \bar{1})_A$	$(\bar{1}\ \overline{4.7074}\ 3.6996)_A$ $(\bar{1}\ 7.0982\ 6.3337)_A$ $(7.0982\ \bar{1}\ 6.3337)_A$ $(\overline{4.7074}\ \bar{1}\ 3.6996)_A$	Variant 3 – Variant *A* Variant 18 – Variant *B* Twinning plane – $(5.3126\ 5.3126\ \bar{1})_A$ Habit plane $T_{2,3}$ – $(\bar{1}\ \overline{4.7074}\ 3.6996)_A$
2-18	0.7201-0.2799 0.2799-0.7201	Type I twin	$(110)_A$	$(1\ 4.4407\ 3.9838)_A$ $(1\ \overline{6.5193}\ 5.0776)_A$ $(6.5193\ \bar{1}\ 5.0776)_A$ $(4.4407\ 1\ \overline{3.9838})_A$	
3-12	0.7201-0.2799 0.2799-0.7201	Type I twin	$(110)_A$	$(\bar{1}\ 6.5193\ 5.0776)_A$ $(\bar{1}\ \overline{4.4407}\ 3.9838)_A$ $(4.4407\ 1\ 3.9838)_A$ $(\overline{6.5193}\ 1\ 5.0776)_A$	Variant 3 – Variant *A* Variant 12 – Variant *C* Twinning plane – $(110)_A$ Habit plane T_1 – $(\bar{1}\ \overline{4.4407}\ 3.9838)_A$

Table 6.6 (*continued*)

Variant pair	Volume fraction	OR	Variant interface	Invariant habit plane	Correspondence with the experimental result
4-8	0.7179-0.2821 0.2821-0.7179	Type II twin	$(1\ \overline{5.3126}\ 5.3126)_A$	$(3.6996\ \overline{4.7074}\ 1)_A$ $(6.3337\ 7.0982\ 1)_A$ $(\overline{6.3337}\ 1\ 7.0982)_A$ $(3.6996\ \bar{1}\ 4.7074)_A$	
10-6	0.7179-0.2821 0.2821-0.7179	Type II twin	$(\bar{1}\ \overline{5.3126}\ 5.3126)_A$	$(\overline{6.3337}\ 7.0982\ 1)_A$ $(3.6996\ 4.7074\ \bar{1})_A$ $(3.6996\ 1\ \overline{4.7074})_A$ $(6.3337\ 1\ 7.0982)_A$	
4-6	0.7201-0.2799 0.2799-0.7201	Type I twin	$(0\bar{1}1)_A$	$(3.9838\ \overline{4.4407}\ 1)_A$ $(5.0776\ 6.5193\ 1)_A$ $(3.9838\ 1\ \overline{4.4407})_A$ $(5.0776\ 1\ 6.5193)_A$	
10-8	0.7201-0.2799 0.2799-0.7201	Type I twin	$(0\bar{1}1)_A$	$(3.9838\ 4.4407\ \bar{1})_A$ $(\overline{5.0776}\ 6.5193\ 1)_A$ $(\overline{5.0776}\ 1\ 6.5193)_A$ $(3.9838\ \bar{1}\ 4.4407)_A$	

Table 6.6 (*continued*)

Variant pair	Volume fraction	OR	Variant interface	Invariant habit plane	Correspondence with the experimental result
5-17	0.7179-0.2821 0.2821-0.7179	Type II twin	$(5.3126\ \overline{5.3126}\ \bar{1})_A$	$(1\ 7.0982\ \overline{6.3337})_A$ $(\bar{1}\ 4.7074\ 3.6996)_A$ $(\overline{4.7074}\ 1\ 3.6996)_A$ $(7.0982\ 1\ 6.3337)_A$	
22-14	0.7179-0.2821 0.2821-0.7179	Type II twin	$(5.3126\ \overline{5.3126}\ 1)_A$	$(1\ \overline{4.7074}\ 3.6996)_A$ $(1\ 7.0982\ 6.3337)_A$ $(\overline{7.0982}\ \bar{1}\ 6.3337)_A$ $(4.7074\ \bar{1}\ 3.6996)_A$	
5-14	0.7201-0.2799 0.2799-0.7201	Type I twin	$(1\bar{1}0)_A$	$(\bar{1}\ 4.4407\ 3.9838)_A$ $(\bar{1}\ \overline{6.5193}\ 5.0776)_A$ $(\overline{6.5193}\ \bar{1}\ 5.0776)_A$ $(4.4407\ \bar{1}\ 3.9838)_A$	
22-17	0.7201-0.2799 0.2799-0.7201	Type I twin	$(1\bar{1}0)_A$	$(1\ 6.5193\ 5.0776)_A$ $(\bar{1}\ 4.4407\ \overline{3.9838})_A$ $(\overline{4.4407}\ 1\ 3.9838)_A$ $(6.5193\ 1\ 5.0776)_A$	

Table 6.6 (*continued*)

Variant pair	Volume fraction	OR	Variant interface	Invariant habit plane	Correspondence with the experimental result
9-16	0.7179-0.2821 0.2821-0.7179	Type II twin	$(5.3126\ \bar{1}\ 5.3126)_A$	$(4.7074\ \overline{3.6996}\ 1)_A$ $(7.0982\ 6.3337\ \bar{1})_A$ $(\bar{1}\ 6.3337\ 7.0982)_A$ $(1\ \overline{3.6996}\ 4.7074)_A$	
23-13	0.7179-0.2821 0.2821-0.7179	Type II twin	$(5.3126\ 1\ 5.3126)_A$	$(\overline{7.0982}\ 6.3337\ 1)_A$ $(4.7074\ 3.6996\ 1)_A$ $(1\ 3.6996\ 4.7074)_A$ $(1\ 6.3337\ \overline{7.0982})_A$	
9-13	0.7201-0.2799 0.2799-0.7201	Type I twin	$(101)_A$	$(4.4407\ \overline{3.9838}\ 1)_A$ $(6.5193\ 5.0776\ \bar{1})_A$ $(1\ 5.0776\ \overline{6.5193})_A$ $(1\ 3.9838\ 4.4407)_A$	
23-16	0.7201-0.2799 0.2799-0.7201	Type I twin	$(101)_A$	$(4.4407\ 3.9838\ 1)_A$ $(\overline{6.5193}\ 5.0776\ 1)_A$ $(\bar{1}\ 5.0776\ 6.5193)_A$ $(1\ \overline{3.9838}\ 4.4407)_A$	

Table 6.6 (*continued*)

Variant pair	Volume fraction	OR	Variant interface	Invariant habit plane	Correspondence with the experimental result
11-19	0.7179-0.2821 0.2821-0.7179	Type II twin	$(5.3126\ \bar{1}\ \overline{5.3126})_A$	$(4.7074\ \overline{3.6996}\ \bar{1})_A$ $(7.0982\ 6.3337\ 1)_A$ $(\bar{1}\ 6.3337\ \overline{7.0982})_A$ $(\bar{1}\ 3.6996\ 4.7074)_A$	
20-15	0.7179-0.2821 0.2821-0.7179	Type II twin	$(5.3126\ 1\ \overline{5.3126})_A$	$(\overline{7.0982}\ 6.3337\ \bar{1})_A$ $(4.7074\ 3.6996\ \bar{1})_A$ $(1\ 3.6996\ \overline{4.7074})_A$ $(1\ 6.3337\ 7.0982)_A$	Variant 20 – Variant *C′* Variant 15 – Variant *D′* Twinning plane – $(5.3126\ 1\ \overline{5.3126})_A$ Habit plane T_5 – $(4.7074\ 3.6996\ \bar{1})_A$
11-15	0.7201-0.2799 0.2799-0.7201	Type I twin	$(10\bar{1})_A$	$(\overline{4.4407}\ 3.9838\ 1)_A$ $(6.5193\ 5.0776\ 1)_A$ $(1\ 3.9838\ \overline{4.4407})_A$ $(1\ 5.0776\ 6.5193)_A$	
20-19	0.7201-0.2799 0.2799-0.7201	Type I twin	$(10\bar{1})_A$	$(4.4407\ 3.9838\ \bar{1})_A$ $(\overline{6.5193}\ 5.0776\ \bar{1})_A$ $(\bar{1}\ 5.0776\ \overline{6.5193})_A$ $(1\ \overline{3.9838}\ \overline{4.4407})_A$	

Table 6.6 shows the calculated results of all the possible variant pairs that can form a self-accommodated sandwich-like variant colony, *i.e.*, producing coherent variant interface and invariant habit plane. The variant pairs are grouped according to the orientation of the variant interface planes in the table, *i.e.*, variant pairs with closely oriented interface planes are put in one group. It can be seen that all the variant pairs that can provide matched interfaces possess a twin relationship. They can form only two types of twins, type I or type II twin. This corresponds to the results obtained experimentally in this alloy where the variants in the sandwich structure are all twin related either with type I or type II twin relation. It is seen that the 24 variants can be divided into 6 groups. Each group contains 4 variants and they share one common $\{0\bar{1}\bar{1}\}_A$ plane. The 4 variants can form two pairs of type I twins and two pairs of type II twins. The calculated variant interfaces are further expressed in the lattice basis of martensite under the Pitsch OR. The type I twin interfaces are the $\{2\bar{2}\bar{1}\}_M$ planes (corresponding to $\{0\bar{1}\bar{1}\}_A$ plane of austenite) and the type II twin interfaces are $\{1.37\ \overline{1.68}\ \bar{1}\}_M$ ($\{5.3126\ 5.3126\ 1\}_A$), respectively. The calculated variant interfaces coincide with the twinning plane K_1 of either the type I twin or the type II twin. The interfaces of the two type I twins possess the same interface orientation, whereas the interfaces of the two type II twins are deviated by 15.2° across the type I twin interface orientation. These features correspond exactly to the characteristics of variants in a broad plate or variant colony as experimentally revealed in Chapter 4, suggesting that the 4 variants in each group in **Table 6.6** are from one variant colony composed of variants *A*, *B*, *C* and *D*. The calculation results in **Table 6.6** also show that mathematically each variant pair with fixed fraction ratio could produce two habit planes. The volume fraction of the two variants can be exchanged. This exchange does not affect the type of habit plane (belonging to the same family of planes) but affects the orientation of the habit plane. For the variant pairs with type I twin relation, their habit planes belong to either $\{1\ 3.9838\ 4.4407\}_A$ or $\{1\ 5.0776\ 6.5193\}_A$ family and the volume fraction of the main variant is 0.7201, whereas for the variant pairs with type II twin relation, their habit planes belong to either $\{1\ 3.6996\ 4.7074\}_A$ or $\{1\ 6.3337\ 7.0982\}_A$ family and the volume fraction of the main variant is 0.7179.

For the present alloy, all the variant pairs detected through experiments can be found among the calculated variant pairs that can provide geometrical compatibility at both variant interfaces and phase interfaces or habit planes in **Table 6.6**. For the intragranular martensite colony (**Fig. 6.3**), the pair of type I twin, variant pair *A* and *C* in the vicinity of interface T_1, corresponds to variant pair 3-12 in **Table 6.6** and the pair of type II twin, variant pair *A* and *B* in the vicinity of the interfaces T_2 and T_3, corresponds to variant pair 3-18 in **Table 6.6**. For the intergranular colonies in **Fig. 6.5**, the two pairs of type II twins, (variant pairs *A′* and *B′* at the vicinity of T_4 and *C′* and *D′* at the vicinity of T_5), corresponding to variant pairs 1-24 and 20-15 in **Table 6.6**, respectively. The calculated habit planes related to the variant pairs in the colonies at the two locations of austenite were verified with the observed habit plane traces. The results are displayed with the corresponding habit plane pole figures and shown in **Fig. 6.10**. For the intragranular colony, among the three observed phase interfaces ($T_1 \sim T_3$) two of them (T_1 and T_2) can well match the predicted habit planes with about 1° angular deviation. This indicates that interfaces T_1 and T_2 are the invariant planes. However for interface T_3, the observed trace is 9.62° away from the theoretical trace. The reason of this discrepancy will be analyzed latter. For the intergranular colonies (as shown in **Fig. 6.5**), the observed phase interfaces T_4 and T_5 can well match the predicted traces of the habit planes $((3.6996\ 4.7074\ 1)_A$ and $(4.7074\ 3.6996\ \bar{1}))$ (with about 0.65° angular deviation). For the volume fractions, the experimental values of the major and minor variants shown in the inset of **Fig. 6.3**(b) and **Fig. 6.5**(a_2) are basically in accordance with the calculated ones. These results indicate that the formation of the sandwich structures in the present alloy is indeed to minimize the lattice mismatches at the phase interface regions and thus to reduce the transformation resistance.

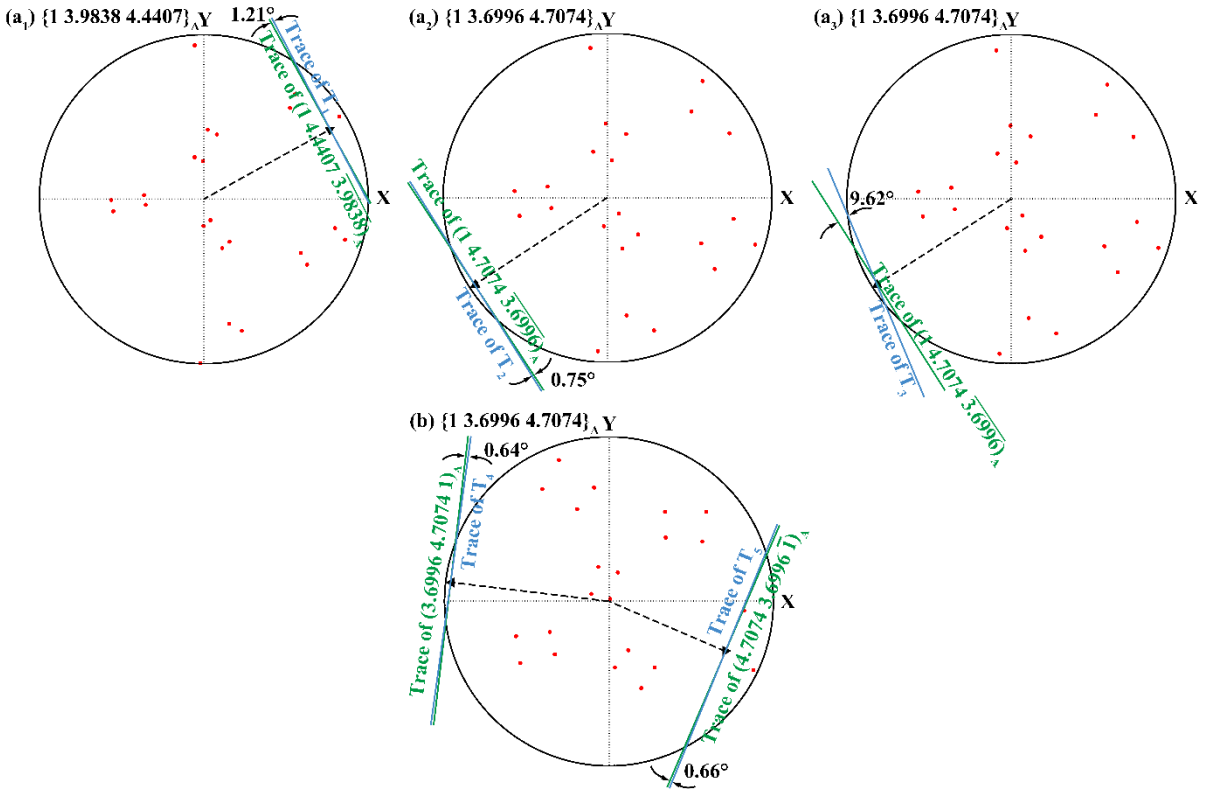

Fig. 6.10 Stereographic projections of the calculated habit planes compared with the observed habit plane traces in **Fig. 6.3** and **Fig. 6.5**. (a_1)~(a_3) Habit planes of the intragranular martensite sandwich and (b) habit planes of the intergranular martensite sandwiches.

In fact, the results shown in **Table 6.6** only include variant pairs that provide compatible variant interfaces and invariant habit planes. There also exist some variant pairs that can form compatible variant interfaces but cannot produce an invariant phase interface or habit plane. The details of these variant pairs and the corresponding OR and variant interface are given in **Table 6.7**.

Table 6.7 Variant pairs that can only form compatible variant interface and OR between the paired variants and the Miller indices of the interface.

Variant pair	OR	Variant interface	Variant pair	OR	Variant interface
1-7	Compound twin	$(100)_A$	24-21	Compound twin	$(100)_A$
2-3	Compound twin	$(001)_A$	12-18	Compound twin	$(001)_A$
4-10	Compound twin	$(100)_A$	8-6	Compound twin	$(100)_A$
5-22	Compound twin	$(001)_A$	17-14	Compound twin	$(001)_A$
9-23	Compound twin	$(010)_A$	16-13	Compound twin	$(010)_A$
11-20	Compound twin	$(010)_A$	19-15	Compound twin	$(010)_A$

It can be seen that there are 12 variant pairs and all these 12 pairs are compound twin related. The variant interface is the $\{001\}_A$ plane that correspond to the $\{201\}_M$ twinning plane of compound twins. Such twins have been found in variant colonies between variant *A* and *D* and between variant *B* and *C*, as shown in **Fig. 4.5** in Chapter 4. Compound twins are variant pairs in the length direction of a lamella in the sandwich structure, as illustrated in **Fig. 6.11**.

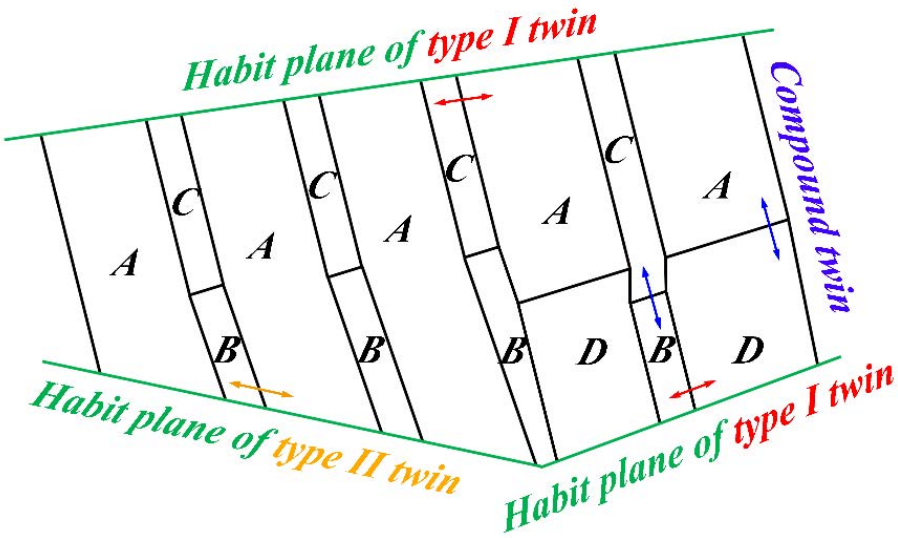

Fig. 6.11 Illustration of sandwich structure composed of 4 distinct variants that form 3 different twin types.

By forming compound twins in the length direction of the lamellae in a sandwich, the variant combination changes from type I twin relation from one habit plane to type II twin relation to another habit plane, as shown in **Fig. 6.11**, thus the sandwich structure can be enclosed by several differently oriented invariant habit planes and form a closed variant colony. Thus the practical sandwich structure in the present alloy is more complicated than that illustrated in **Fig. 6.7**(b), where the structure contains only two variants and only one oriented habit plane.

6.4.2 Dimension characters of sandwich structured variant colony

The above analyses using the crystallographic theory of martensitic transformation well revealed the underlying mechanisms of the formation of sandwich structure of martensite variant colonies for self-accommodation of the transformation strains. However there are still

questions remain un-answered. The morphology or dimension features of the sandwich structured variant colonies are not explained and the appearance of some phase interfaces not predicted by the theory, as the case of habit plane T_3, is also not explained. Moreover, the numbers of the variant pairs with type I and type II twin relations are not the same, although the calculated results demonstrate that there is no advantages one over the other in terms of invariant habit plane and compatible variant interface.

Clearly the dimension singularity of the sandwich structured variant colony is closely related to the transformation strain characters of the paired variants. Thus with the deformation gradient tensor obtained by examining atomic correspondences between the parent and the product phase under the Pitsch OR as described above, the deformation gradient tensor of each variant can be obtained. Here we use the three variants *A*, *B*, and *C* in the intragranular variant colony in **Fig. 6.3** as an example. The three variants correspond to variant 3, 18 and 12 in **Table 6.5**. The total deformation gradient tensor for type I twin (F_I for variant pair *A* and *C*) and type II twin (F_{II} for variant pair *A* and *B*) combination with the volume fraction of each variant indicated in **Table 6.6** are calculated and displayed in Eqs. (6.8a) and (6.8b). F_A, F_B and F_C are the deformation gradient tensors of the respective variants. The coefficients before these three deformation gradient tensors are the calculated volume fraction of the three variants from **Table 6.6**. All the deformation gradient tensors given in Eqs. (6.8a) and (6.8b) are expressed in an orthonormal coordinate frame '*i*-*j*-*k*' whose ***i*** is $[\overline{0.6035}\ 0.6035\ 0.5212]_A$ (the intersection line of the habit plane T_1 $(\bar{1}\ \overline{4.4407}\ 3.9838)_A$ and the twinning plane of type I twin $(110)_A$), ***k*** is $[\overline{0.1653}\ \overline{0.7341}\ 0.6586]_A$ (the normal of the habit plane T_1), and ***j*** is $[\overline{0.7801}\ \overline{0.3113}\ \overline{0.5428}]_A$ (the cross product of axes ***k*** and ***i***) as illustrated in **Fig. 6.12**.

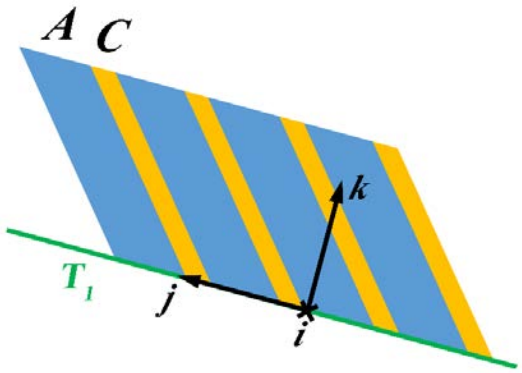

Fig. 6.12 Illustration of the '*i*-*j*-*k*' frame set respect to the microstructure of the intragranular variant colony at the vicinity of habit plane T_1.

$$F_I = 0.7201\times F_A + 0.2799\times F_C = \begin{matrix} \\ i \\ j \\ k \end{matrix}\begin{matrix} \begin{matrix} i & \quad j & \quad k \end{matrix} \\ \begin{pmatrix} 1.0002 & 0.0084 & 0.0384 \\ -0.0090 & 0.9999 & -0.0071 \\ 0.0109 & -0.0214 & 0.9909 \end{pmatrix} \end{matrix} \quad (6.8a)$$

$$F_{II} = 0.7179\times F_A + 0.2821\times F_B = \begin{matrix} \\ i \\ j \\ k \end{matrix}\begin{matrix} \begin{matrix} i & \quad j & \quad k \end{matrix} \\ \begin{pmatrix} 0.9977 & 0.0133 & 0.0371 \\ -0.0100 & 0.9989 & -0.0100 \\ 0.0121 & -0.0201 & 0.9945 \end{pmatrix} \end{matrix} \quad (6.8b)$$

In the deformation gradient tensor, the difference of the 3 diagonal elements $F(i, i)$, $F(j, j)$ or $F(k, k)$ from 1 represent a normal strain along the *i*, *j* or *k* axis, while the 6 off diagonal elements represent a shear (for example the element $F(i, j)$ represents a shear in ***i*** direction on the plane normal to ***j***). For the first matrix we can find that the two elements $F_I(i, i)$ = 1.0002 and $F_I(j, j)$ = 0.9999 are quite close to 1, *i.e.* the normal strain along the *i* and *j* axes are very small. However, the element $F_I(k, k)$ = 0.9909 is much smaller than 1, *i.e.* there exists a high compressive strain (0.0091) along the normal of the habit plane. Among the 6 shear strain elements, $F_I(i, k)$ is much higher (0.0384), indicating that a large strain can be reached when the sandwich thickens in the direction of ***k***. The second highest shear component is $F_I(k, j)$ (-0.0214), inferring that a relative large shear strain can be created when the sandwich enlarges in the direction of ***j***. The deformation strain of the type II twin combination (Eq. (6.8b)) possesses almost the same characters as those of the type I twin. Such a deformation will result in a plate-shaped variant colony whose length along the *k* axis is much limited (restricted by the high compressive strain along this direction and the shear $F_I(i, k)$), whereas the other two

directions ***i*** and ***j*** are much longer, especially the dimension in the direction of ***i*** (almost stress-free). This corresponds to the intragranular colony in **Fig. 6.3**(a) that largely extends along the habit plane T_1. However, the constraint in the direction of ***j*** ($F_I(k, j)$) cannot be ignored. The habit planes cannot extend unlimitedly. This explains why the sandwich structured variant colonies are always enclosed by segments of differently oriented habit planes.

Such a deformation character of the sandwiched variant pair with either type I twin or type II twin relation can also explain the appearance of the non-predicted habit plane, T_3 in **Fig. 6.3**. Calculation results show that the two habit planes T_1 and T_2 have a 3.68° angular deviation. Thus, with the extension of the sandwich structured colony along the habit plane T_1 and T_2, the distance between the two habit planes increases. The high compressive strain along the *k* axis and the shear component $F_I(i, k)$ will lead to a large accumulated strain in the direction of ***k***. Thus, another phase interface, *i.e.* interface T_3, is generated to enclose this plate-shaped sandwich structure and limits the dimension of the colony in the direction of ***k***. Experimental results show that the variants composition in the vicinity of interfaces T_2 and T_3 are the same. Therefore the orientation change of the habit plane could be realized by introducing steps of the type II twin interfaces to T_2, as illustrated with the red dash lines in **Fig. 6.13**. In this way, the dimension in *k* will be limited. The composition of T_3 are the planes (T_2 and K_1 of type II twin) with excellent geometrical compatibility and hence of low interfacial energy planes.

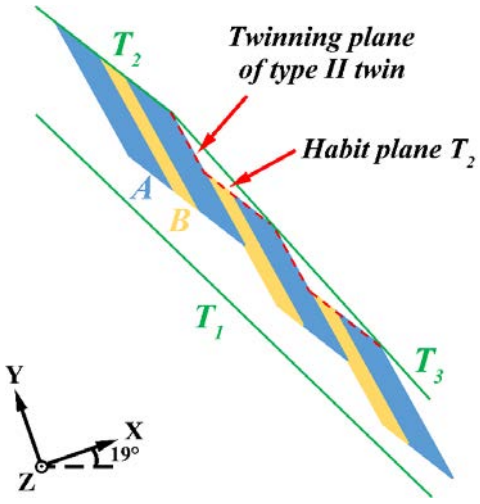

Fig. 6.13 Illustration of the composition of the phase interface T_3. The '*x*-*y*-*z*' coordinate set with respect to the one shown in **Fig. 6.3**.

6.4.3 Selection of variant combination in variant colony

The in-equivalent occurrence frequencies of the type I and the type II twin related variant pairs in the sandwich structured variant colonies are also related to the characteristic deformation of the paired variants. For convenience, the deformation gradient tensors of the variant pairs with type I twin or type II twin relations were further expressed in the type I twinning reference system and displayed in Eq. (6.9).

$$F_I{}' = \begin{matrix} i \\ j \\ k \end{matrix} \overset{\begin{matrix} i & j & k \end{matrix}}{\begin{pmatrix} 0.9847 & 0.0056 & 0.0334 \\ -0.0046 & 1.0240 & 0.0080 \\ 0 & 0 & 0.9823 \end{pmatrix}} \tag{6.9a}$$

$$F_{II}{}' = \begin{matrix} i \\ j \\ k \end{matrix} \overset{\begin{matrix} i & j & k \end{matrix}}{\begin{pmatrix} 0.9854 & -0.0001 & 0.0325 \\ -0.0045 & 1.0234 & 0.0129 \\ 0 & 0 & 0.9823 \end{pmatrix}} \tag{6.9b}$$

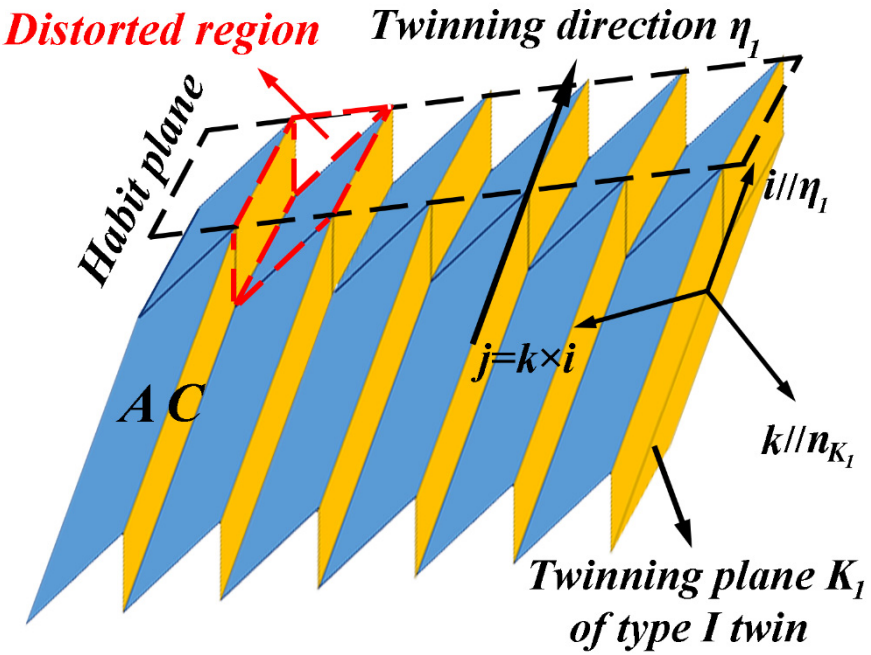

Fig. 6.14 Illustration of the sandwich structure composed of type I twin and the reference system '*i*-*j*-*k*' set to the twinning system.

Under the twinning reference system as illustrated in **Fig. 6.14**, the unit basis vector ***i*** is parallel to $\boldsymbol{\eta_1}$ (the twinning direction $[0.7022\ \overline{0.7022}\ 0.1173]_A$ expressed in the Bravais lattice basis of austenite), ***k*** parallel to the normal direction of K_1 ($(110)_A$, the twinning plane and also the variant interface) and ***j*** the vector product of ***k*** and ***i***. Comparing the two matrices, one can

find that the largest difference happens to the shear component $F'(i, j)$. The value of $F_{II}'(i, j)$ of the type II twin combination (-0.0001) is much smaller than that of the type I twin combination (0.0056). This shear strain will restrict the elongation of the variants in the direction of ***j***. The large value results in a dimension reduction of the variants in this direction and hence an increase in the interfacial area. Thus type II twin combination is more energetically favorable. For the other components, the type II twin combination has slightly smaller values except $F_{II}'(j, k)$. The value of the type II twin is 0.0129 larger than that of the type I twin 0.0080. This shear component restricts the growth of the variant pair in the direction normal to the variant interface. As the thickening of the lamellae is mainly restricted by the lattice distortion near the habit plane area, as outlined with the red dash lines in **Fig. 6.14**, the thickness of the variants are greatly reduced with respect to the other two perpendicular directions. The accumulated shear in the direction normal to the variant interface is much smaller thus the adverse influence of the $F_{II}'(j, k)$ component of type II twin become negligible. As a whole, the type II twin combination is more energetically favorable than the type I twin combination and thus occurs in majority in the present alloy.

6.4.4 Selection rule of neighboring sandwich structured variant colonies to form wedge-shaped martensite and midrib plane

From the above results, it can be seen that the sandwich structured variant colony is the basic microstructural unit of the orthorhombic martensite in NiMnSb alloys. As revealed by the experimental results in Chapter 5, the adjacency of variant colonies (sandwiches) is not arbitrary but also selective, especially in the case of sub-colonies in Chapter 5. Thus the selection of variant colonies as neighbors exists. Due to the selection, the so-called wedge-shaped martensite agglomeration composed of two sandwich-like variant colonies that are conjoined by a straight midrib plane, as illustrated in **Fig. 6.15**, at the beginning stage of martensitic transformation is produced and reported in the literature [116]. Such specific microstructural features also appear in the present alloy, as shown in **Fig. 6.5**.

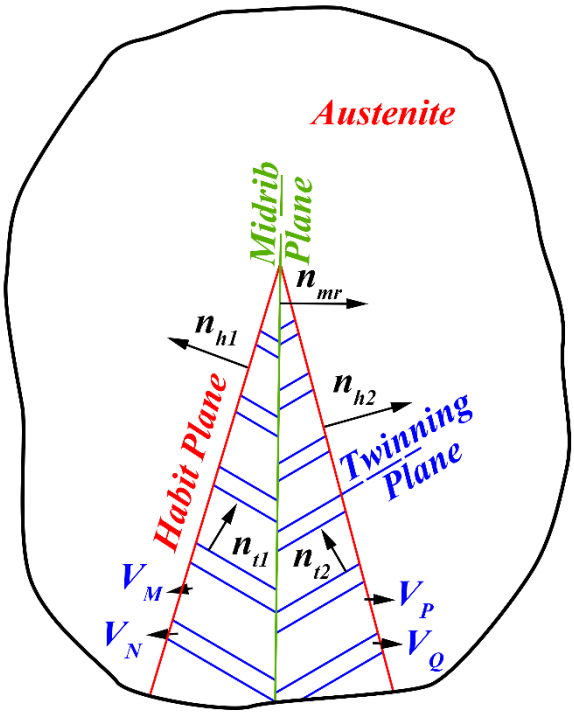

Fig. 6.15 Illustration of martensite variants in wedge-shaped morphology in austenite.

According to the crystallographic theory of martensitic transformation, the combination of the two sandwiches should produce the smallest atomic misfit at the midrib plane. Obeying the same geometrical compatibility criterion as for variant interface and habit plane, the geometrical compatibility conditions of the two variant colonies at the midrib plane should be satisfied, as mathematically expressed in Eq. (6.10).

$$(\boldsymbol{a_{h1}}\otimes\boldsymbol{n_{h1}} + I) - (\boldsymbol{a_{h2}}\otimes\boldsymbol{n_{h2}} + I) = \boldsymbol{a_{mr}}\otimes\boldsymbol{n_{mr}}. \tag{6.10}$$

The variables in the equation are indicated in **Fig. 6.15**. To solve Eq. (6.10), the geometrical compatibility equations for variant interfaces in the 2 sandwiches and for the habit planes of the two sandwiches on the two sides of the midrib plane can be used to obtain the needed variables in Eq. (6.10). They are:

$$\begin{aligned} Q_{12}(\lambda_1 Q_{11} U_M - (1-\lambda_1)U_N) - I &= \boldsymbol{a_{h1}}\otimes\boldsymbol{n_{h1}} \\ Q_{22}\big(\lambda_2 Q_{21} U_P - (1-\lambda_2)U_Q\big) - I &= \boldsymbol{a_{h2}}\otimes\boldsymbol{n_{h2}} \end{aligned} \tag{6.11a}$$

for habit planes and

$$\begin{aligned} Q_{11} U_M - U_N &= \boldsymbol{a_{t1}}\otimes\boldsymbol{n_{t1}} \\ Q_{21} U_P - U_Q &= \boldsymbol{a_{t2}}\otimes\boldsymbol{n_{t2}} \end{aligned} \tag{6.11b}$$

for the variant interfaces. In Eq. (6.10), the two terms, $\boldsymbol{a_{h1}}\otimes\boldsymbol{n_{h1}}+I$ and $\boldsymbol{a_{h2}}\otimes\boldsymbol{n_{h2}}+I$, are the relative deformation gradient tensors of the sandwiches on the left and on the right in **Fig. 6.15**; $\boldsymbol{n_{mr}}$ is the vector normal to the midrib plane; $\boldsymbol{a_{mr}}$ is a vector on the midrib plane. If the two sandwiches are geometrically compatible at the midrib plane, as the case of variant interface and the case of habit plane, there should exist two vectors for Eq. (6.10) such that the left side of the equation, $(\boldsymbol{a_{h1}}\otimes\boldsymbol{n_{h1}}+I)-(\boldsymbol{a_{h2}}\otimes\boldsymbol{n_{h2}}+I)$, can be expressed by a dyadic product of the two vectors, one being the normal vector of the midrib plane and the other a vector on the midrib plane. With all the possible variants that can form self-accommodated sandwiches listed in **Table 6.6**, we calculate all the possible combinations of variants to form a wedge-shaped structure. However, the calculations reveal that none of the combinations of sandwiches can produce a total match at the midrib plane, *i.e.* a stress-free plane without atomic mismatch. The same situation has been found for materials undergoing cubic to orthorhombic transformation [116, 145, 146]. Thus a tiny rotation Q_{mr} is induced in the theory to describe the degree of misfit at the midrib plane [130], so that Eq. (6.10) is rewritten as

$$Q_{mr}(\boldsymbol{a_{h1}}\otimes\boldsymbol{n_{h1}}+I)-(\boldsymbol{a_{h2}}\otimes\boldsymbol{n_{h2}}+I)=\boldsymbol{a_{mr}}\otimes\boldsymbol{n_{mr}}, \tag{6.12}$$

with

$$\theta_{mr}=\left|arc\cos\left(\frac{tr(Q_{mr})-1}{2}\right)\right|. \tag{6.13}$$

The rotation matrix Q_{mr} serves as an indicator to characterize the misfit of the two sandwiches at the midrib plane. Balandraud *et al.* found that this indicator should satisfy the critical condition that $\theta_{mr}\leq 0.3°$ [130]. Based on this criterion, we calculate all the possible sandwich combinations. Results show that there exist 48 distinct wedges in total. Their midrib planes belong to the family of $\{0\bar{1}\bar{1}\}_A$ planes. The 48 wedges can further divided into 6 equivalent groups, each group possessing a common $\{0\bar{1}\bar{1}\}_A$ plane. Here, we take the group that possess the $(101)_A$ plane as the midrib plane as an example and illustrate their geometrical feature, such as twin type, variant interfaces, habit planes and the misfit angle in **Fig. 6.16**.

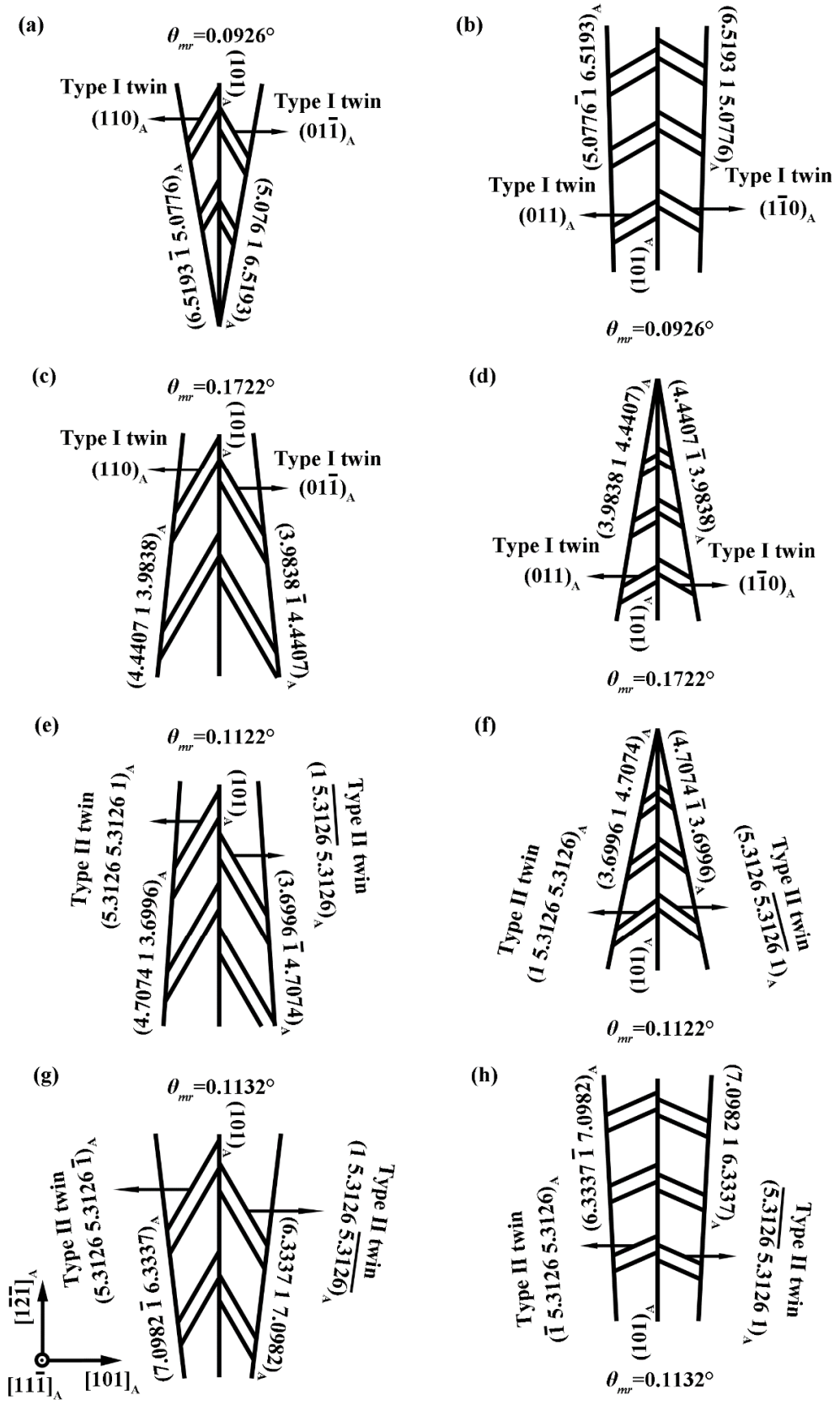

Fig. 6.16 Geometrical features of the group of wedges possessing the $(101)_A$ plane as the midrib plane.

It is seen that from **Fig. 6.16** the variant pairs in the two sandwiches possess the same twin type, either type I or type II. The habit planes of the two sandwiches belong to the same plane family. The habit planes of each wedge is also close to the corresponding midrib plane $(101)_A$ (with a 6.83° ~ 11.67° angular deviation). For the misfit indicator θ_{mr}, we can see that the wedges that possess the same family of planes as the habit planes have the common misfit indicator (0.0926° for the wedges in **Figs. 6.16**(a) and (b), 0.1722° in **Figs. 6.16**(c) and (d), 0.1122° in **Figs. 6.16**(e) and (f) and 0.1132° in **Figs. 6.16**(g) and (h)). The misfit indicator on the midrib plane for type I - type I wedge with the habit planes in the $\{5.0776\ 1\ 6.5193\}_A$ family (**Figs. 6.16**(a) and (b)) is the smallest (0.0926°), whereas that for type I - type I wedge with the habit plane in the $\{4.4407\ 1\ 3.9838\}_A$ family (**Figs. 6.16**(c) and (d)) is the largest (0.1722°). The other two pairs of type II - type II wedges have a slightly higher θ_{mr}, (~0.02°) than the smallest one. This infers that the type I - type I wedge with smallest misfit and the two pairs of type II - type II wedges are energetically favorable and could be easy to form during the martensitic transformation. The other 5 groups of wedges are equivalent to the above example group and can be easily obtained by symmetry operation. The detailed crystallographic information concerning the twin types, the habit planes, the midrib planes and the midrib plane misfit indicators of all the wedges are given in **Table 6.8**. For reference and for completion, the information about the volume fraction of the variants and their geometrical correlations is also listed in the table.

Table 6.8 Crystallographic information of the 48 calculated wedge-shaped martensite.

Wedge No.	Variant pair	Volume fraction	OR	Midrib plane	Common $\{0\bar{1}\bar{1}\}_A$ plane shared by the two variants	Zone axis of the three $\{0\bar{1}\bar{1}\}_A$ planes (variant interface and the midrib plane)	misfit indicator θ_{mr}
1	1-24 20-15	0.7179-0.2821 0.7179-0.2821	Type II twin	$(110)_A$	$(0\bar{1}\bar{1})_A$ $(10\bar{1})_A$	$[1\bar{1}1]_A$	0.1122°
2	1-21 20-19	0.7201-0.2799 0.7201-0.2799	Type I twin	$(110)_A$	$(0\bar{1}\bar{1})_A$ $(10\bar{1})_A$	$[1\bar{1}1]_A$	0.1722°
3	7-24 11-15	0.7201-0.2799 0.7201-0.2799	Type I twin	$(110)_A$	$(0\bar{1}\bar{1})_A$ $(10\bar{1})_A$	$[1\bar{1}1]_A$	0.0926°
4	7-21 11-19	0.7179-0.2821 0.7179-0.2821	Type II twin	$(110)_A$	$(0\bar{1}\bar{1})_A$ $(10\bar{1})_A$	$[1\bar{1}1]_A$	0.1132°
5	4-8 9-16	0.7179-0.2821 0.7179-0.2821	Type II twin	$(110)_A$	$(0\bar{1}1)_A$ $(\bar{1}0\bar{1})_A$	$[\bar{1}11]_A$	0.1132°
6	4-6 9-13	0.7201-0.2799 0.7201-0.2799	Type I twin	$(110)_A$	$(0\bar{1}1)_A$ $(\bar{1}0\bar{1})_A$	$[\bar{1}11]_A$	0.0926°
7	10-8 23-16	0.7201-0.2799 0.7201-0.2799	Type I twin	$(110)_A$	$(0\bar{1}1)_A$ $(\bar{1}0\bar{1})_A$	$[\bar{1}11]_A$	0.1722°
8	10-6 23-13	0.7179-0.2821 0.7179-0.2821	Type II twin	$(110)_A$	$(0\bar{1}1)_A$ $(\bar{1}0\bar{1})_A$	$[\bar{1}11]_A$	0.1122°

Table 6.8 (*continued*)

Wedge No.	Variant pair	Volume fraction	OR	Midrib plane	Common $\{0\bar{1}\bar{1}\}_A$ plane shared by the two variants	Zone axis of the three $\{0\bar{1}\bar{1}\}_A$ planes (variant interface and the midrib plane)	misfit indicator θ_{mr}
9	7-24 9-13	0.7201-0.2799 0.7201-0.2799	Type I twin	$(110)_A$	$(0\bar{1}\bar{1})_A$ $(\bar{1}0\bar{1})_A$	$[11\bar{1}]_A$	0.1722°
10	10-6 20-15	0.7179-0.2821 0.7179-0.2821	Type II twin	$(110)_A$	$(0\bar{1}1)_A$ $(10\bar{1})_A$	$[111]_A$	0.1132°
11	10-8 20-19	0.7201-0.2799 0.7201-0.2799	Type I twin	$(110)_A$	$(0\bar{1}1)_A$ $(10\bar{1})_A$	$[111]_A$	0.0926°
12	7-21 9-16	0.7179-0.2821 0.7179-0.2821	Type II twin	$(110)_A$	$(0\bar{1}\bar{1})_A$ $(\bar{1}0\bar{1})_A$	$[11\bar{1}]_A$	0.1122°
13	4-8 11-19	0.7179-0.2821 0.7179-0.2821	Type II twin	$(110)_A$	$(0\bar{1}1)_A$ $(10\bar{1})_A$	$[111]_A$	0.1122°
14	1-21 23-16	0.7201-0.2799 0.7201-0.2799	Type I twin	$(110)_A$	$(0\bar{1}\bar{1})_A$ $(\bar{1}0\bar{1})_A$	$[11\bar{1}]_A$	0.0926°
15	4-6 11-15	0.7201-0.2799 0.7201-0.2799	Type I twin	$(110)_A$	$(0\bar{1}1)_A$ $(10\bar{1})_A$	$[111]_A$	0.1722°
16	1-24 23-13	0.7179-0.2821 0.7179-0.2821	Type II twin	$(110)_A$	$(0\bar{1}\bar{1})_A$ $(\bar{1}0\bar{1})_A$	$[11\bar{1}]_A$	0.1132°

Table 6.8 (*continued*)

Wedge No.	Variant pair	Volume fraction	OR	Midrib plane	Common $\{0\bar{1}\bar{1}\}_A$ plane shared by the two variants	Zone axis of the three $\{0\bar{1}\bar{1}\}_A$ planes (variant interface and the midrib plane)	misfit indicator θ_{mr}
17	7-21 5-17	0.2821-0.7179 0.2821-0.7179	Type II twin	$(101)_A$	$(0\bar{1}\bar{1})_A$ $(1\bar{1}0)_A$	$[11\bar{1}]_A$	0.1132°
18	10-8 3-12	0.2799-0.7201 0.2799-0.7201	Type I twin	$(101)_A$	$(0\bar{1}1)_A$ $(110)_A$	$[\bar{1}11]_A$	0.1722°
19	10-6 3-18	0.2821-0.7179 0.2821-0.7179	Type II twin	$(101)_A$	$(0\bar{1}1)_A$ $(110)_A$	$[\bar{1}11]_A$	0.1132°
20	7-24 5-14	0.2799-0.7201 0.2799-0.7201	Type I twin	$(101)_A$	$(0\bar{1}\bar{1})_A$ $(1\bar{1}0)_A$	$[11\bar{1}]_A$	0.1722°
21	4-8 2-12	0.2821-0.7179 0.2821-0.7179	Type II twin	$(101)_A$	$(0\bar{1}1)_A$ $(110)_A$	$[\bar{1}11]_A$	0.1122°
22	1-21 22-17	0.2799-0.7201 0.2799-0.7201	Type I twin	$(101)_A$	$(0\bar{1}\bar{1})_A$ $(1\bar{1}0)_A$	$[11\bar{1}]_A$	0.0926°
23	1-24 22-14	0.2821-0.7179 0.2821-0.7179	Type II twin	$(101)_A$	$(0\bar{1}\bar{1})_A$ $(1\bar{1}0)_A$	$[11\bar{1}]_A$	0.1122°
24	4-6 2-18	0.2799-0.7201 0.2799-0.7201	Type I twin	$(101)_A$	$(0\bar{1}1)_A$ $(110)_A$	$[\bar{1}11]_A$	0.0926°

Table 6.8 (*continued*)

Wedge No.	Variant pair	Volume fraction	OR	Midrib plane	Common $\{0\bar{1}\bar{1}\}_A$ plane shared by the two variants	Zone axis of the three $\{0\bar{1}\bar{1}\}_A$ planes (variant interface and the midrib plane)	misfit indicator θ_{mr}
25	7-21 3-18	0.2821-0.7179 0.2821-0.7179	Type II twin	$(10\bar{1})_A$	$(0\bar{1}\bar{1})_A$ $(110)_A$	$[1\bar{1}1]_A$	0.1122°
26	10-8 5-14	0.2799-0.7201 0.2799-0.7201	Type I twin	$(10\bar{1})_A$	$(0\bar{1}1)_A$ $(1\bar{1}0)_A$	$[111]_A$	0.0926°
27	10-6 5-17	0.2821-0.7179 0.2821-0.7179	Type II twin	$(10\bar{1})_A$	$(0\bar{1}1)_A$ $(1\bar{1}0)_A$	$[111]_A$	0.1122°
28	7-24 3-12	0.2799-0.7201 0.2799-0.7201	Type I twin	$(10\bar{1})_A$	$(0\bar{1}\bar{1})_A$ $(110)_A$	$[1\bar{1}1]_A$	0.0926°
29	1-21 2-18	0.2799-0.7201 0.2799-0.7201	Type I twin	$(10\bar{1})_A$	$(0\bar{1}\bar{1})_A$ $(110)_A$	$[1\bar{1}1]_A$	0.1722°
30	4-8 22-14	0.2821-0.7179 0.2821-0.7179	Type II twin	$(10\bar{1})_A$	$(0\bar{1}1)_A$ $(1\bar{1}0)_A$	$[111]_A$	0.1132°
31	1-24 2-12	0.2821-0.7179 0.2821-0.7179	Type II twin	$(10\bar{1})_A$	$(0\bar{1}\bar{1})_A$ $(110)_A$	$[1\bar{1}1]_A$	0.1132°
32	4-6 22-17	0.2799-0.7201 0.2799-0.7201	Type I twin	$(10\bar{1})_A$	$(0\bar{1}1)_A$ $(1\bar{1}0)_A$	$[111]_A$	0.1722°

Table 6.8 (*continued*)

Wedge No.	Variant pair	Volume fraction	OR	Midrib plane	Common $\{0\bar{1}\bar{1}\}_A$ plane shared by the two variants	Zone axis of the three $\{0\bar{1}\bar{1}\}_A$ planes (variant interface and the midrib plane)	misfit indicator θ_{mr}
33	5-14 13-9	0.7201-0.2799 0.7201-0.2799	Type I twin	$(011)_A$	$(1\bar{1}0)_A$ $(\bar{1}0\bar{1})_A$	$[11\bar{1}]_A$	0.1722°
34	3-18 15-20	0.7179-0.2821 0.7179-0.2821	Type II twin	$(011)_A$	$(110)_A$ $(10\bar{1})_A$	$[1\bar{1}1]_A$	0.1132°
35	5-17 13-23	0.7179-0.2821 0.7179-0.2821	Type II twin	$(011)_A$	$(1\bar{1}0)_A$ $(\bar{1}0\bar{1})_A$	$[11\bar{1}]_A$	0.1122°
36	3-12 15-11	0.7201-0.2799 0.7201-0.2799	Type I twin	$(011)_A$	$(110)_A$ $(10\bar{1})_A$	$[1\bar{1}1]_A$	0.0926°
37	2-18 19-20	0.7201-0.2799 0.7201-0.2799	Type I twin	$(011)_A$	$(110)_A$ $(10\bar{1})_A$	$[1\bar{1}1]_A$	0.1722°
38	22-14 16-9	0.7179-0.2821 0.7179-0.2821	Type II twin	$(011)_A$	$(1\bar{1}0)_A$ $(\bar{1}0\bar{1})_A$	$[11\bar{1}]_A$	0.1132°
39	22-17 16-23	0.7201-0.2799 0.7201-0.2799	Type I twin	$(011)_A$	$(1\bar{1}0)_A$ $(\bar{1}0\bar{1})_A$	$[11\bar{1}]_A$	0.0926°
40	2-12 19-11	0.7179-0.2821 0.7179-0.2821	Type II twin	$(011)_A$	$(110)_A$ $(10\bar{1})_A$	$[1\bar{1}1]_A$	0.1122°

Table 6.8 (*continued*)

Wedge No.	Variant pair	Volume fraction	OR	Midrib plane	Common $\{0\bar{1}\bar{1}\}_A$ plane shared by the two variants	Zone axis of the three $\{0\bar{1}\bar{1}\}_A$ planes (variant interface and the midrib plane)	misfit indicator θ_{mr}
41	5-14 19-20	0.7201-0.2799 0.7201-0.2799	Type I twin	$(01\bar{1})_A$	$(1\bar{1}0)_A$ $(10\bar{1})_A$	$[111]_A$	0.0926°
42	3-18 16-9	0.7179-0.2821 0.7179-0.2821	Type II twin	$(01\bar{1})_A$	$(110)_A$ $(\bar{1}0\bar{1})_A$	$[\bar{1}11]_A$	0.1122°
43	3-12 16-23	0.7201-0.2799 0.7201-0.2799	Type I twin	$(01\bar{1})_A$	$(110)_A$ $(\bar{1}0\bar{1})_A$	$[\bar{1}11]_A$	0.1722°
44	5-17 19-11	0.7179-0.2821 0.7179-0.2821	Type II twin	$(01\bar{1})_A$	$(1\bar{1}0)_A$ $(10\bar{1})_A$	$[111]_A$	0.1132°
45	2-18 13-9	0.7201-0.2799 0.7201-0.2799	Type I twin	$(01\bar{1})_A$	$(110)_A$ $(\bar{1}0\bar{1})_A$	$[\bar{1}11]_A$	0.0926°
46	22-14 15-20	0.7179-0.2821 0.7179-0.2821	Type II twin	$(01\bar{1})_A$	$(1\bar{1}0)_A$ $(10\bar{1})_A$	$[111]_A$	0.1122°
47	2-12 13-23	0.7179-0.2821 0.7179-0.2821	Type II twin	$(01\bar{1})_A$	$(110)_A$ $(\bar{1}0\bar{1})_A$	$[\bar{1}11]_A$	0.1132°
48	22-17 15-11	0.7201-0.2799 0.7201-0.2799	Type I twin	$(01\bar{1})_A$	$(1\bar{1}0)_A$ $(10\bar{1})_A$	$[111]_A$	0.1722°

Comparing the calculated results with the experimentally detected wedge-shaped martensite agglomeration shown in **Fig. 6.5**, we can find the observed one corresponds to wedge 1 in **Table 6.8**. All the observed interfaces, containing the habit planes, twinning planes and the midrib plane are in good accordance with the calculated ones. In addition, from the results listed in **Table 6.8**, more crystallographic characteristic of the wedge can be revealed. For each wedge, the three $\{0\bar{1}\bar{1}\}_A$ planes possessed by one wedge, one being the midrib plane and two being the common $\{0\bar{1}\bar{1}\}_A$ planes shared by the two variants in each sandwich, belong to one $<111>_A$ axis zone. These three $\{0\bar{1}\bar{1}\}_A$ planes are interrelated by a 60° rotation along the common $<111>_A$ axis. Such crystallographic feature is in accordance with that of the sub-colony thoroughly explained in Chapter 5. Hence, the formation of the wedge-shaped martensite structure in the early stage of intergranular transformation is well correlated with the resultant microstructure of the martensite phase.

Furthermore, the deformation characteristics of the component sandwiches in the wedge is also studied. Here, we take the wedge shown in **Fig. 6.5** as an example. The deformation gradient tensors of the two sandwiches F_{III} (for variant pair A' and B') and F_{IV} (for variant pair C' and D') are given in Eqs. (6.14a) and (6.14b).

$$F_{III} = 0.7179\times F_{A'} + 0.2821\times F_{B'} = \begin{matrix} \\ i \\ j \\ k \end{matrix}\begin{matrix} \begin{matrix} i & j & k \end{matrix} \\ \begin{pmatrix} 0.9992 & -0.0187 & -0.0353 \\ 0.0077 & 0.9952 & -0.0050 \\ -0.0161 & -0.0192 & 0.9967 \end{pmatrix} \end{matrix} \tag{6.14a}$$

$$F_{IV} = 0.7179\times F_{C'} + 0.2821\times F_{D'} = \begin{matrix} \\ i \\ j \\ k \end{matrix}\begin{matrix} \begin{matrix} i & j & k \end{matrix} \\ \begin{pmatrix} 0.9992 & -0.0187 & 0.0353 \\ 0.0077 & 0.9952 & 0.0050 \\ 0.0161 & 0.0192 & 0.9967 \end{pmatrix} \end{matrix} \tag{6.14b}$$

The two deformation gradient tensors are expressed in the orthonormal coordinate frame '*i*-*j*-*k*' whose ***i*** is $[\overline{0.6133}\ 0.6133\ \overline{0.4978}]_A$ (the intersection line of the midrib plane $(110)_A$ and the K_1 plane of the type II twin (variant pair A' and B') $(5.3126\ 1\ \overline{5.3126})_A$), ***k*** is $[0.7071\ 0.7071\ 0]_A$ (the normal direction of the midrib plane), and ***j*** to $[\overline{0.3520}\ 0.3520\ 0.8673]_A$ (the cross product of ***k*** and ***i***), as shown in **Fig. 6.17**.

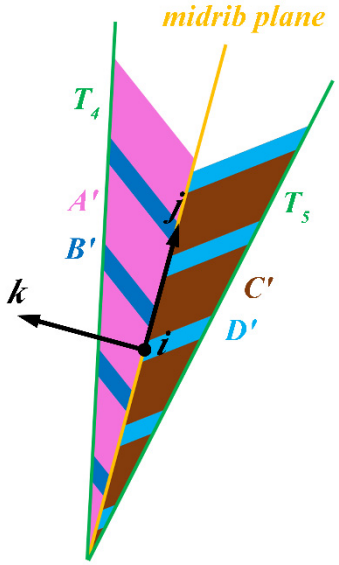

Fig. 6.17 Illustration of the orthonormal '*i*-*j*-*k*' frame and the microstructure of the martensite wedge.

It can be seen that the components of the two tensor matrices possess a matched edge to edge deformation character. All the corresponding elements in the two tensors have exactly the same absolute value with the sign of $F(i, k)$, $F(j, k)$, $F(k, i)$ and $F(k, j)$ reversed. With **Fig. 6.17**, we can see that, under such a deformation manner, the two sandwiches keep a matched transformation deformation along the directions of ***i*** and ***j*** (the same $F(j, i)$ and $F(i, j)$). For the shear deformation either in the direction of ***k*** or on the plane normal to ***k***, *i.e.* on the midrib plane, the sign of the strain is reversed. This keeps the deformation on the two sides of the midrib plane symmetrical and balanced. This is why during the transformation process the midrib plane is stationary. For the other 47 wedge-shaped martensite listed in **Table 6.8** the situations are equivalent. Thus the formation of wedge-shaped martensite structure is also to minimize the transformation strain and mismatches at plate interfaces and thus energetically favorable.

6.5 Summary

In this chapter, the formation mechanism and its correlation with the morphological and crystallographic features of the orthorhombic NiMnSb martensite microstructure were studied. The experimental and theoretical calculation results reveal that the sandwich structured variant colony is the basic microstructural unit of the martensite. The sandwich colony is composed of alternately distributed twin related fine lamellar variants. The variant interfaces are totally coherent. The phase

interfaces, *i.e.* the habit planes, between the sandwich colony and the parent austenite are all invariant planes. The formation of this kind of structure can effectively minimize the transformation resistance and achieving a structure with high atomic compatibility on these two interfaces. Due to the large normal strain in the direction normal to the habit plane and the large shear strain on the plane parallel to the habit plane of the paired variants in variant colonies, the sandwich structured variant colony is always in plate shape, especially at the beginning of the transformation. They mainly stretch along the habit plane but very less in the direction normal to the habit plane. Due to such deformation characteristics, habit planes composed of segments of invariant habit plane and variant interface can be formed to enclose the variant colony. Due to the relative small shear strain that restricts the elongation of the variant pairs along the twinning direction η_1 of type I twin, the formation of type II twin related variant pairs in the variant colony is energetically favorable, thus the occurrence of type II twins in variant colonies are in majority. The formation of wedge-shaped structure composed of two selected sandwiches separated by a midrib plane is also to minimize the transformation strain at the interface of the sandwiches. The midrib plane is the $\{0\bar{1}\bar{1}\}_A$ plane and shared by the variants from the two colonies. The atomic mismatch of the two colonies at the midrib plane θ_{mr} is between 0.0926° and 0.1722° in the present alloy. All these above results indicate that the formation of the martensite phase obeys the minimum transformation strain and the best atomic matches criteria, *i.e.* the minimum interfacial and elastic strain energy criteria and the martensite phase is self-accommodated resulting in a specific microstructural pattern.

With the experimental and the theoretical results obtain in this chapter, the formation mechanisms of sandwich colony, habit plane and wedged-shaped agglomeration are resolved.

Chapter 7 Conclusions and Perspectives

7.1 Conclusions

In the present work, a thorough experimental and theoretically crystallographic study on microstructure and martensitic transformation has been conducted on NiMnSb metamagnetic multi-functional alloys. From the experimental and calculation results of the present work, following main conclusions can be drawn:

Morphological and crystallographic features of austenite and 4O modulated martensite

The austenite of NiMnSb alloys possesses a cubic $L2_1$ crystal structure belonging to the space group $Fm\bar{3}m$ (No. 225). The lattice constants of the $Ni_{50}Mn_{37}Sb_{13}$ austenite are a_A = 5.9749 Å.

The martensite has a *4O* structure belonging to the space group *Pmma* (No. 051) with Ni atoms occupying the *4h* (0, 0.7547, 0.5) and *4k* (0.25, 0.2483, 0.0731) positions; Mn atoms the *2a* (0, 0, 0), *2f* (0.25, 0.5, 0.5721), *2b* (0, 0.5, 0) and *2e* (0.25, 0, 0.5731) positions; Sb atoms *2b* (0, 0.5, 0) and *2e* (0.25, 0, 0.5731) positions. The lattice constants of the $Ni_{50}Mn_{37}Sb_{13}$ martensite are a_M = 8.5830 Å, b_M = 5.6533 Å and c_M = 4.3501 Å, and those of the $Ni_{50}Mn_{38}Sb_{12}$ martensite are a_M = 8.5788 Å, b_M = 5.6443 Å and c_M = 4.3479 Å, respectively. The size of the cell reduces with the increase of Mn and the decrease of Sb.

Morphological and crystallographic features of austenite and 4O modulated martensite

For the NiMnSb alloy, the high temperature phase is austenite, composed of equiaxed grains with sizes of about hundreds of micrometres in diameter and the low temperature phase is martensite in lamellar shape with widths in sub micrometer range.

The microstructure of the *4O* NiMnSb modulated martensite possesses a hierarchical organization of the martensite variants. Martensite lamellae or variants are organized into colonies in plate shape with widths about 5 - 10 μm. In each broad shaped variant colony, there are 4 distinct variants *A*, *B*, *C* and *D* distributed alternately and stretching roughly in the same direction, forming a kind of sandwich structure. The 4 variants are all twin related with either type I twin, type II twin or

compound twin relation. The twinning elements of the three types of twins are fully resolved in the present PhD work. The 4 variants can form two pairs of type I twin (*A* and *C*; *B* and *D*), two pairs of type II twin (*A* and *B*; *C* and *D*) and two pairs of compound twin (*A* and *D*; *B* and *C*). The interfaces between variants coincide with their twinning plane K_1. The two types of type I twin possess the same interface orientation and so do the two pairs of compound twin interfaces, whereas the two pairs of type II twin each possesses an interface orientation. The angle between the two interfaces is 15.2° and the orientations of the two type II twin interfaces are in symmetry relation with respect to that of the type I twin interface. Plate shaped variant colonies having common plate interface orientation are further organized into sub-colonies. Each sub-colony contains 2 distinct variant colonies, *i.e.* 8 distinct variants, that are distributed alternately. For any of the 4 distinct variants in one variant colony, there exists one variant in the adjacent variant colony that possesses a 180° rotation relationship with it. The planes normal to the 180° rotation axes in these variants possesses the same orientation and are parallel to the plate interface. Sub-colonies having the common plate interface orientation can further form plate colonies. Each plate colony is composed of 2 distinct sub-colonies (containing 4 distinct plates and 16 distinct variants) that are also distributed alternately. Eventually, several plate colonies with different plate interface orientations occupy an original austenite grain.

Martensitic transformation OR and crystallographic correlation between martensite variant colonies

The Pitsch OR, specified as $\{0\bar{1}\bar{1}\}_A$ // $\{2\bar{2}\bar{1}\}_M$ and $<0\bar{1}1>_A$ // $<\bar{1}\bar{2}2>_M$, is the effective OR for the martensitic transformation between the cubic austenite and the *4O* modulated martensite of the NiMnSb alloys. Under this OR, 24 distinct martensite variants can be produced in one original austenite grain. In fact, the organizations of variants in variant colonies, sub colonies and plate colonies are all referenced to the $\{0\bar{1}\bar{1}\}_A$ planes of austenite. The 4 variants in each variant colony are all with their type I twinning planes $\{2\bar{2}\bar{1}\}_M$ parallel to one of the 6 $\{0\bar{1}\bar{1}\}_A$ planes. The plate interfaces in each sub colony is parallel to another $\{0\bar{1}\bar{1}\}_A$ plane. The three $\{0\bar{1}\bar{1}\}_A$ planes shared by one sub-colony, one corresponding to the plate interface and the other two to the type I twin interfaces in the adjacent plates, are related by 60° and belong to one $<111>_A$ axis zone. For the plate colony,

the two groups of three $\{0\bar{1}\bar{1}\}_A$ planes, each shared by one sub colony, belong to two $<111>_A$ axis zones but the two axis zones possess one common $\{0\bar{1}\bar{1}\}_A$ plane. This plane is also the plate interfaces of the constituent plates in the plate colony.

The characters of the self-accommodated martensitic transformation and its impact on microstructure

During the transformation, variant colonies form intragranularly and intergranularly in austenite. The sandwich structured variant colony is the basic microstructural unit of the martensite. The formation of the type I or type II twin related sandwich structure can cancel the elastic strain produced by one variant with that produced by the other variant at the phase interface regions, which results in macroscopically invariant habit planes, and provide coherently matched variant interface. Although compound twin related variants cannot generate invariant habit plane, it allows variant combination change from type I (or II) relation to type II (or I) relation, thus producing differently oriented habit planes. Phase interface can also be formed with segments of invariant phase interface and coherent variant interfaces to close up the variant colony. The sandwich structured variant colonies are in general in plate shape with the dimension normal to the habit plane smallest, owing to the anisotropic strain produced by the variant pair. The largest strain occurs to the direction normal to the habit planes and the strains on the other two perpendicular direction are very small. The relatively small shear strain of type II twin related variant pairs that restricts the elongation of the variant pairs along the twinning direction η_1 of type I twinning system makes the occurrence of type II twin more favorable and thus their appearance is in majority. Wedge-shaped structures that composed of two selected sandwiches separated by a midrib plane also form during the transformation. The two variant colonies can largely match at the midrib plane. The misfit θ_{mr} is between 0.0926° and 0.1722° in the present alloy. The midrib plane corresponds to one of the $\{0\bar{1}\bar{1}\}_A$ planes of austenite and also the plate interface of the variant colonies. The two variant colonies in the wedge structure constitute of the two distinct variant plates of one sub colony. During the transformation process, the habit planes move toward the austenite and disappear when meeting other variant colonies, whereas the midrib plane

stays stationary, as the strains from the two variant colonies at the midrib plane are totally symmetrical and balanced.

To conclude, the martensitic transformation of NiMnSb alloys is self-accommodated to achieve invariant habit plane, coherent variant interfaces and well matched variant colony interfaces. The deformation characteristics of the transformation determine the self-accommodation mechanisms and the resultant microstructure.

7.2 Perspectives

In this PhD work, a thoroughly crystallographic study was conducted on the crystal structures of austenite and martensite, martensitic transformation OR and its correlation with the martensite microstructure features, and the transformation deformation characteristics and their self-accommodations in ternary NiMnSb alloys. Comprehensive information concerning these fundamental issues was obtained for this new type of multifunctional materials, opening new perspectives on further investigations of this alloy system and can be summarized as follows:

(1) For NiMnSb alloys, all the magnetic properties are closely related to the magnetic structure of the martensite and the austenite. Since the crystal structure information of the two phases is clear now, the magnetic structure can be studied by *ab-initio* calculations. Thus, the interactions between atoms, especially the Mn-Mn atoms, can be clarified. This will allow revealing the underlying physical mechanisms behind the magnetic field driven phenomena of these alloys.

(2) It is known that the magnetic properties of polycrystalline NiMnSb alloys can be improved via texturation. With the knowledge on orientation relationships between martensite variants and between austenite and martensite, efficient mechanical or thermo-mechanical training schemes can be designed and practiced for texturation of these alloys.

(3) The crystal structures of martensite and austenite have been proved to be decisive factors on the transformation strain as well as on the microstructure of martensite phase. Hence, effect of changing the lattice constants by means of element doping to modify variant organization manners can be studied for theoretical purpose and for technical purpose.

References

[1] L.C. Chang, T.A. Read. Plastic deformation and diffusionless phase changes in metals - the AuCd β-phase, Trans. AIME 191(1) (1951) 47-52.

[2] A. Ölander. The crystal structure of AuCd, Z. Kristallogr. 83(1/2) (1932) 145-148.

[3] W.J. Buehler, J.V. Gilfrich, R.C. Wiley. Effect of low-temperature phase changes on the mechanical properties of alloys near composition TiNi, Appl. Phys. 34 (1963) 1475-1477.

[4] R.H. Bricknell, K.N. Melton, O. Mercier. The structure of NiTiCu shape memory alloys, Metall. Mater. Trans. A 10 (1979) 693-697.

[5] D.A. Miller, D.C. Lagoudas. Thermomechanical characterization of NiTiCu and NiTi SMA actuators: influence of plastic strains, Smart Mater. Struct. 9 (2000) 640-652.

[6] H. Sehitoglu, I. Karaman, X. Zhang, A. Viswanath, Y. Chumlyakov, H.J. Maier. Strain-temperature behavior of NiTiCu shape memory single crystals, Acta Mater. 49 (2001) 3621-3634.

[7] A. Biscarini, B. Coluzzi, G. Mazzolai, A. Tuissi, F.M. Mazzolai. Extraordinary high damping of hydrogen-doped NiTi and NiTiCu shape memory alloys, J. Alloy. Compd. 355 (2003) 52-57.

[8] J. Pfetzing-Micklich, M.F.-X. Wagner, R. Zarnetta, J. Frenzel, G. Eggeler, A.E. Markaki, J. Wheeler, T.W. Clyne. Nanoindentation of a Pseudoelastic NiTiFe Shape Memory Alloy, Adv. Eng. Mater. 12 (2010) 13-19.

[9] V.G. Pushin, V.N. Khachin, A.S. Savvinov, V.V. Kondratiev. Structural phase-transformations and properties of NiTi and NiTiFe alloys, Dokl. Akad. Nauk. SSSR+ 277 (1984) 1388-1391.

[10] E. Choi, Y.S. Chung, J.H. Choi, H.T. Kim, H. Lee. The confining effectiveness of NiTiNb and NiTi SMA wire jackets for concrete, Smart Mater. Struct. 19 (2010) 035024.

[11] M.J. Wang, M.Y. Jiang, G.Y. Liao, S. Guo, X.Q. Zhao. Martensitic transformation involved mechanical behaviors and wide hysteresis of NiTiNb shape memory alloys, Prog. Nat. Sci. 22 (2012) 130-138.

[12] G.S. Bigelow, S.A. Padula, A. Garg, D. Gaydosh, R.D. Noebe. Characterization of ternary NiTiPd high-temperature shape-memory alloys under load-biased thermal cycling, Metall. Mater. Trans. A 41A (2010) 3065-3079.

[13] J.A. Monroe, I. Karaman, D.C. Lagoudas, G.S. Bigelow, R.D. Noebe, S.A. Padula. Determining recoverable and irrecoverable contributions to accumulated strain in a NiTiPd high-temperature shape memory alloy during thermomechanical cycling, Scripta Mater. 65 (2011) 123-126.

[14] G.N. Sure, L.C. Brown. The mechanical properties of grain refined β-CuAlNi strain-memory alloys, Metall. Mater. Trans. A 15 (1984) 1613-1621.

[15] P. Sedlák, H. Seiner, M. Landa, V. Novák, P. Šittner, L. Mañosa. Elastic constants of bcc austenite and 2H orthorhombic martensite in CuAlNi shape memory alloy, Acta Mater. 53 (2005) 3643-3661.

[16] D.N. Fang, W. Lu, W.Y. Yan, T. Inoue, K.C. Hwang. Stress-strain relation of CuAlNi SMA single crystal under biaxial loading-constitutive model and experiments, Acta Mater. 47 (1998) 269-280.

[17] K. Gall, K. Jacobus, H. Sehitoglu, H.J. Maier. Stress-induced martensitic phase transformations in polycrystalline CuZnAl shape memory alloys under different stress states, Metall. Mater. Trans. A 29 (1998) 765-773.

[18] K. Takezawa, T. Shindo, S. Sato. Shape memory effect in β_1-CuZnAl alloys, Scripta Metall. Mater. 10 (1976) 13-18.

[19] Y. Yamaguchi, S. Miyazaki, S. Kumai, A. Sato. Strengthening of a FeMnSi-based shape memory alloy by dispersion of χ-phase domains, Philos. Mag. 86 (2006) 4319-4340.

[20] C. Feng, J.C. Zhao, F. Yang, S.J. Hao, K. Gong, D. Hu, Y. Cao, X.M. Jiang, Z.Q. Wang, L. Chen, S.R. Li, L. Sun, L.S. Cui, G.H. Yu. Reversible and nonvolatile modulations of magnetization switching characteristic and domain configuration in $L1_0$-FePt films via nonelectrically controlled strain engineering, Appl. Mater. Interfaces 8 (2016) 7545-7552.

[21] D. Stoeckel. Shape memory actuators for automotive applications, Mater. Des. 11 (1990) 302-307.

[22] C. Bil, K. Massey, E.J. Abdullah. Wing morpging control with shape memory alloy actuators, J. Intell. Mater. Syst. Struct. 24 (2013) 879-898.

[23] D.J. Hartl, D.C. Lagoudas. Aerospace applications of shape memory alloys, P. I. Mech. Eng. G-J. Aer. 221 (2007) 535-552.

[24] K. Otsuka, X.B. Ren. Recent developments in the research of shape memory alloys, Intermetallics 7 (1999) 511-528.

[25] K. Rolfs, M. Chmielus, R.C. Wimpory, A. Mecklenburg, P. Müllner, R. Schneider. Double twinning in Ni-Mn-Ga-Co, Acta Mater. 58 (2010) 2646-2651.

[26] E. Pagounis, R. Chulist, T. TLippmann, M. Laufenberg, W. Skrotzki. Structural modification and twinning stress reduction in a high-temperature Ni-Mn-Ga magnetic shape memory alloy, Appl. Phys. Lett. 103 (2013) 111911.

[27] L. Straka, J. Drahokoupil, O. Pacherová, K. Fabiánová, V. Kopecký, H. Seiner, H. Hänninen, O. Heczko. The relation between lattice parameters and very low twinning stress in $Ni_{50}Mn_{(25+x)}Ga_{(25-x)}$ magnetic shape memory alloys, Smart Mater. Struct. 25 (2016) 025001.

[28] B. Muntifering, L. Kovarik, N.D. Browning, R.C. Pond, W.B. Knowlton, P. Müllner. Stress-assisted removal of conjugation boundaries in non-modulated Ni–Mn–Ga by coordinated secondary twinning, J. Mater. Sci. 51 (2015) 457-466.

[29] H.E. Karaca, I. Karaman, B. Basaran, Y. Ren, Y.I. Chumlyakov, H.J. Maier. Magnetic field-induced phase transformation in NiMnCoIn magnetic shape-memory alloys - a new actuation mechanism with large work output, Adv. Funct. Mater. 19 (2009) 983-998.

[30] R. Kainuma, Y. Imano, W. Ito, Y. Sutou, H. Morito, S. Okamoto, O. Kitakami, K. Oikawa, A. Fujita, T. Kanomata, K. Ishida. Magnetic-field-induced shape recovery by reverse phase transformation, Nature 439 (2006) 957-960.

[31] T. Krenke, E. Duman, M. Acet, E.F. Wassermann, X. Moya, L. Manosa, A. Planes, E. Suard, B. Ouladdiaf. Magnetic superelasticity and inverse magnetocaloric effect in Ni-Mn-In, Phys. Rev. B 75 (2007) 104414-104411.

[32] R. Kainuma, Y. Imano, W. Ito, H. Morito, Y. Sutou, K. Oikawa, A. Fujita, K. Ishida, S. Okamoto, O. Kitakami, T. Kanomata. Metamagnetic shape memory effect in a Heusler-type $Ni_{43}Co_7Mn_{39}Sn_{11}$ polycrystalline alloy, Appl. Phys. Lett. 88 (2006) 192513.

[33] K. Ito, W. Ito, R.Y. Umetsu, S. Tajima, H. Kawaura, R. Kainuma, K. Ishida. Metamagnetic shape memory effect in polycrystalline NiCoMnSn alloy fabricated by spark plasma sintering, Scripta Mater. 61 (2009) 504-507.

[34] Y. Sutou, Y. Imano, N. Koeda, T. Omori, R. Kainuma, K. Ishida, K. Oikawa. Magnetic and martensitic transformations of NiMnX (X = In, Sn, Sb) ferromagnetic shape memory alloys, Appl. Phys. Lett. 85 (2004) 4358-4360.

[35] S.Y. Yu, J.J. Wei, S.S. Kang, J.L. Chen, G.H. Wu. Large temperature and magnetic field induced strain in polycrystalline $Ni_{50}Mn_{36}In_{(14-x)}Sb_x$ alloys, J. Alloys Compd. 586 (2014) 328-332.

[36] J. Du, Q. Zheng, W.J. Ren, W.J. Feng, X.G. Liu, Z.D. Zhang. Magnetocaloric effect and magnetic-field-induced shape recovery effect at room temperature in ferromagnetic Heusler alloy Ni-Mn-Sb, J. Phys. D: Appl. Phys. 40 (2007) 5523-5526.

[37] A. Fujita, K. Fukamichi, F. Gejima, R. Kainuma, K. Ishida. Magnetic properties and large magnetic-field-induced strains in off-stoichiometric Ni–Mn–Al Heusler alloys, Appl. Phys. Lett. 77 (2000) 3054-3056.

[38] Y. Murakami, D. Shindo, K. Oikawa, R. Kainuma, K. Ishida. Magnetic domain structure in a ferromagnetic shape memory alloy $Ni_{51}Fe_{22}Ga_{27}$ studied by electron holography and Lorentz microscopy, Appl. Phys. Lett. 82 (2003) 3695-3697.

[39] K. Oikawa, T. Ota, T. Ohmori, Y. Tanaka, H. Morito, A. Fujita, R. Kainuma, K. Fukamichi, K. Ishida. Magnetic and martensitic phase transitions in ferromagnetic Ni–Ga–Fe shape memory alloys, Appl. Phys. Lett. 81 (2002) 5201-5203.

[40] M. Wuttig, J. Li, C. Craciunescu. A new ferromagnetic shape memory alloy system, Scripta Mater. 44 (2001) 2393-2397.

[41] K. Ulakko, J.K. Huang, C. Kantner, R.C. O'Handley, V.V. Kokorin. Large magnetic-field-induced strains in Ni_2MnGa single crystals, Appl. Phys. Lett. 69 (1996) 1966-1968.

[42] A. Sozinov, N. Lanska, A. Soroka, W. Zou. 12% magnetic field-induced strain in Ni-Mn-Ga-based non-modulated martensite, Appl. Phys. Lett. 102 (2013) 021902.

[43] R.N. Couch, I. Chopra. Experimental characterization of NiMnGa magnetic shape memory alloy rods under dynamic magnetic fields, Proc. SPIE 5053 (2003) 169-180.

[44] C.P. Henry, D. Bono, J. Feuchtwanger, S.M. Allen, R.C. O'Handley. AC field-induced actuation of single crystal Ni-Mn-Ga, J. Appl. Phys. 91 (2002) 7810-7811.

[45] J. Liu, T. Gottschall, K.P. Skokov, J.D. Moore, O. Gutfleisch. Giant magnetocaloric effect driven by structural transitions, Nat. Mater. 11 (2012) 620-620.

[46] T. Krenke, E. Duman, M. Acet, E.F. Wassermann, X. Moya, L. Mañosa, A. Planes. Inverse magnetocaloric effect in ferromagnetic Ni-Mn-Sn alloys, Nat. Mater. 4 (2005) 450-454.

[47] M. Khan, N. Ali, S. Stadler. Inverse magnetocaloric effect in ferromagnetic $Ni_{50}Mn_{(37+x)}Sb_{(13-x)}$ Heusler alloys, J. Appl. Phys. 101 (2007) 053919.

[48] S.Y. Yu, Z.H. Liu, G.D. Liu, J.L. Chen, Z.X. Cao, G.H. Wu, B. Zhang, X.X. Zhang. Large magnetoresistance in single-crystalline $Ni_{50}Mn_{(50-x)}In_x$ alloys (x=14–16) upon martensitic transformation, Appl. Phys. Lett. 89 (2006) 162503.

[49] H.C. Xuan, Y.X. Zheng, S.C. Ma, Q.Q. Cao, D.H. Wang, Y.W. Du. The martensitic transformation, magnetocaloric effect, and magnetoresistance in high-Mn content $Mn_{(47+x)}Ni_{(43-x)}Sn_{10}$ ferromagnetic shape memory alloys, J. Appl. Phys. 108 (2010) 103920.

[50] M. Khan, I. Dubenko, S. Stadler, J. Jung, S.S. Stoyko, A. Mar, A. Quetz, T. Samanta, N. Ali, K.H. Chow. Enhancement of ferromagnetism by Cr doping in Ni-Mn-Cr-Sb Heusler alloys, Appl. Phys. Lett. 102 (2013) 112402.

[51] V.K. Sharma, M.K. Chattopadhyay, S.B. Roy. Kinetic arrest of the first order austenite to martensite phase transition in $Ni_{50}Mn_{34}In_{16}$: dc magnetization studies, Phys. Rev. B 76 (2007) 140401(R).

[52] B.M. Wang, Y. Liu, P. Ren, B. Xia, K.B. Ruan, J.B. Yi, J. Ding, X.G. Li, L. Wang. Large exchange bias after zero-field cooling from an unmagnetized state, Phys. Rev. Lett. 106 (2011) 077203.

[53] Z. Li, C. Jing, J.P. Chen, S.J. Yuan, S.X. Cao, J.C. Zhang. Observation of exchange bias in the martensitic state of $Ni_{50}Mn_{36}Sn_{14}$ Heusler alloy, Appl. Phys. Lett. 91 (2007) 112505.

[54] R. Barman, S.K. Singh, D. Kaur. Enhanced exchange bias in magnetron-sputtered Ni–Mn–Sb–Al ferromagnetic shape memory alloy thin films, Curr. Appl. Phys. 14 (2014) 1755-1759.

[55] R.A. De Groot, F.M. Mueller, P.G. Van Engen, K.H.J. Buschow. New class of materials: half-metallic ferromagnets, Phys. Rev. Lett. 50 (1983) 2024-2027.

[56] J.A. Caballero, Y.D. Park, A. Cabbibo, J.R. Childress, F. Petroff, R. Morel. Deposition of high-quality NiMnSb magnetic thin films at moderate temperatures, J. Appl. Phys. 81 (1997) 2740-2744.

[57] C.T. Tanaka, J. Nowak, J.S. Moodera. Magnetoresistance in ferromagnet-insulator-ferromagnet tunnel junctions with half-metallic ferromagnet NiMnSb compound, J. Appl. Phys. 81 (1997) 5515-5517.

[58] C. Hordequin, J.P. Nozieres, J. Pierre. Half metallic NiMnSb-based spin-valve structures, J. Magn. Magn. Mater. 183 (1998) 225-231.

[59] H.S. Akkera, N. Choudhary, D. Kaur. Martensitic phase transformations and magnetocaloric effect in Al co-sputtered Ni–Mn–Sb alloy thin films, Mater. Sci. Eng. B 198 (2015) 113-119.

[60] Y. Yoshimine, D. Mitsunaga, H. Orihashi, D. Shimada, M. Hiroi, R. Onodera, S. Kimura, K. Takahashi, K. Koyama. Magnetic and electrical properties of $Mn_{(2-x)}Ni_{(1+x)}Sb$, Magnetics, IEEE Transactions on 50 (2014) 1-4.

[61] M.K. Ray, K. Bagani, R.K. Singh, B. Majumdar, S. Banerjee. Effect of Al doping on structural and magnetic properties of $Ni_{50}Mn_{37}Al_xSb_{(13-x)}$ alloy, Physica B 448 (2014) 33-37.

[62] M.K. Ray, K. Bagani, R.K. Singh, B. Majumdar, S. Banerjee. Microstructure, magnetic and electrical transport properties of melt-spun Ni-Mn-Sb ribbons, J. Appl. Phys. 114 (2013) 123904.

[63] M.K. Lee, L.S. Xu, V.V. Marchenkov, R.L. Wang, R.J. Chen, S. Guo, C.P. Yang, J.C.A. Huang. Effect of Ge and Al substitutions on exchange bias in Ni-Mn-Sb alloy, J. Appl. Phys. 113 (2013) 17D712.

[64] H.S. Akkera, R. Barman, N. Kaur, N. Choudhary, D. Kaur. Exchange bias effect in NiMnSb/CrN heterostructures deposited by magnetron sputtering, J. Appl. Phys. 113 (2013) 17D723.

[65] S. Agarwal, P.K. Mukhopadhyay. Role of replacement of Sb with Al in the phase transformation of Ni-Mn-Sb alloys. In: Bhardwaj S, Shekhawat MS, Suthar B, (Eds.). AIP Conf. Proc., vol. 1536. Bikaner, Rajasthan, India: AIP Publishing, 2013. p.977-978.

[66] R. Sahoo, A.K. Nayak, K.G. Suresh, A.K. Nigam. Effect of Fe substitution on the magnetic, transport, thermal and magnetocaloric properties in $Ni_{50}Mn_{38-x}Fe_xSb_{12}$ Heusler alloys, J. Appl. Phys. 109 (2011) 123904.

[67] N.V. Nong, L.T. Tai, N.T. Huy, N.T. Trung, C.R.H. Bahl, R. Venkatesh, F.W. Poulsen, N. Pryds. Structural, magnetic and magnetocaloric properties of Heusler alloys $Ni_{50}Mn_{38}Sb_{12}$ with boron addition, Mater. Sci. Eng. B 176 (2011) 1322-1325.

[68] A.K. Nayak, K.G. Suresh, A.K. Nigam. Correlation between reentrant spin glass behavior and the magnetic order-disorder transition of the martensite phase in Ni-Co-Mn-Sb Heusler alloys, J. Phys.: Condens. Matter 23 (2011) 416004.

[69] W.J. Feng, L. Zuo, Y.B. Li, Y.D. Wang, M. Gao, G.L. Fang. Abnormal e/a - dependence of TM and large inverse magnetocaloric effect in $Ni_{49-x}Cu_xMn_{39}Sb_{12}$ alloys, Mater. Sci. Eng. B 176 (2011) 621-625.

[70] A.K. Nayak, K.G. Suresh, A.K. Nigam. Phase coexistence induced by cooling across the first order transition in Ni-Co-Mn-Sb shape memory alloy, J. Appl. Phys. 108 (2010) 063915.

[71] H.Z. Luo, F.B. Meng, Q.X. Jiang, H.Y. Liu, E.K. Liu, G.H. Wu, Y.X. Wang. Effect of boron on the martensitic transformation and magnetic properties of $Ni_{50}Mn_{36.5}Sb_{13.5-x}B_x$ alloys, Scripta Mater. 63 (2010) 4.

[72] W.J. Feng, Q. Zhang, L.Q. Zhang, B. Li, J. Du, Y.F. Deng, Z.D. Zhang. Large reversible high-temperature magnetocaloric effect in alloys, Solid State Commun. 150 (2010) 949-952.

[73] N.V.R. Rao, R. Gopalan, V. Chandrasekaran, K.G. Suresh. Phase coexistence, microstructure and magnetism in Ni-Mn-Sb alloys, J. Phys. D: Appl. Phys. 42 (2009) 065002.

[74] A.K. Nayak, K.G. Suresh, A.K. Nigam. Giant inverse magnetocaloric effect near room temperature in Co substituted NiMnSb Heusler alloys, J. Phys. D: Appl. Phys. 42 (2009) 035009.

[75] S. Aksoy, M. Acet, E.F. Wassermann, T. Krenke, X. Moya, L. Mañosa, A. Planes, P.P. Deen. Structural properties and magnetic interactions in martensitic Ni-Mn-Sb alloys, Philos. Mag. 89 (2009) 2093-2109.

[76] M. Khan, I. Dubenko, S. Stadler, N. Ali. Magnetostructural phase transitions in $Ni_{50}Mn_{(25+x)}Sb_{(25-x)}$ heusler alloys, J. Phys.: Condens. Matter 20 (2008) 235204.

[77] R. Sahoo, K.G. Suresh, A. Das. Structural and magnetic properties probed using neutron diffraction technique in $Ni_{50-x}Co_xMn_{38}Sb_{12}$ (x = 0 and 5) Heusler system, J. Magn. Magn. Mater. 371 (2014) 94-99.

[78] V. Sánchez-Alarcos, J.I. Pérez-Landazábal, V. Recarte, I. Lucia, J. Vélez, J.A. Rodríguez-Velamazán. Effect of high-temperature quenching on the magnetostructural transformations and the long-range atomic order of Ni-Mn-Sn and Ni-Mn-Sb metamagnetic shape memory alloys, Acta Mater. 61 (2013) 4676-4682.

[79] P.J. Brown, A.P. Gandy, K. Ishida, W. Ito, R. Kainuma, T. Kanomata, K.-U. Neumann, K. Oikawa, B. Ouladdiaf, A. Sheikh, K.R.A. Ziebeck. Magnetic and structural properties of the magnetic shape memory compound $Ni_2Mn_{1.48}Sb_{0.52}$, J. Phys.: Condens. Matter 22 (2010) 096002.

[80] I. Dubenko, M. Khan, A.K. Pathak, B.R. Gautam, S. Stadler, N. Ali. Magnetocaloric effects in Ni-Mn-X based Heusler alloys with X = Ga, Sb, In, J. Magn. Magn. Mater. 321 (2009) 754-757.

[81] R. Sahoo, A.K. Nayak, K.G. Suresh, A.K. Nigam. Structural, magnetic, magnetocaloric and magnetotransport properties in Ge doped Ni-Mn-Sb Heusler alloys, J. Magn. Magn. Mater. 324 (2012) 1267-1271.

[82] N.V.R. Rao, J.A. Chelvane, V. Chandrasekaran, A.V. Morozkin, J. Lamsal, W.B. Yelon, R. Nirmala, K.G. Suresh, S.K. Malik. Neutron diffraction studies on the Heusler alloy $Ni_{50}Mn_{37}Sb_{13}$, J. Appl. Phys. 109 (2011) 07A907.

[83] A.K. Nayak, K.G. Suresh, A.K. Nigam. Anomalous effects of repeated martensitic transitions on the transport, magnetic and thermal properties in Ni-Co-Mn-Sb Heusler alloy, Acta Mater. 59 (2011) 3304-3312.

[84] S. Chatterjee, S. Giri, S. Majumdar, A.K. Deb, S.K. De, V. Hardy. Magneto-structural instability in $Ni_2Mn_{1.4}Sb_{0.6}$ alloy, J. Phys.: Condens. Matter 19 (2007) 346213.

[85] W.J. Feng, J. Du, B. Li, W.J. Hu, Z.D. Zhang, X.H. Li, Y.F. Deng. Large low-field inverse magnetocaloric effect in $Ni_{50-x}Mn_{38+x}Sb_{12}$ alloys, J. Phys. D: Appl. Phys 42 (2009) 125003.

[86] A.K. Pathak, M. Khan, I. Dubenko, S. Stadler, N. Ali. Large magnetic entropy change in $Ni_{50}Mn_{50-x}In_x$ Heusler alloys, Appl. Phys. Lett. 90 (2007) 262504.

[87] A.K. Nayak, K.G. Suresh, A.K. Nigam. Magnetic, electrical, and magnetothermal properties in Ni-Co-Mn-Sb Heusler alloys, J. Appl. Phys. 107 (2010) 09A927.

[88] A.K. Nayak, K.G. Suresh, A.K. Nigam, A.A. Coelho, S. Gama. Pressure induced magnetic and magnetocaloric properties in NiCoMnSb Heusler alloy, J. Appl. Phys. 106 (2009) 053901.

[89] A.K. Nayak, N.V.R. Rao, K.G. Suresh, A.K. Nigam. Magneto-thermal and magneto-transport behavior around the martensitic transition in $Ni_{50-x}Co_xMn_{40}Sb_{10}$ (x=9, 9.5) Heusler alloys, J. Alloys Compd. 499 (2010) 140-143.

[90] R. Sahoo, A.K. Nayak, K.G. Suresh, A.K. Nigam. Effect of Si and Ga substitutions on the magnetocaloric properties of NiCoMnSb quaternary Heusler alloys, J. Appl. Phys. 109 (2011) 07A921.

[91] R. Sahoo, A.K. Nayak, K.G. Suresh, A.K. Nigam. Effect on Magnetic and Magnetocaloric Properties with Ge substitution in Ni-Mn-Sb Heusler Alloys. in: Mittal R, Chauhan AK, Mukhopadhyay R, (Eds.). Solid State Physics, Pts 1 and 2, vol. 1447. 2012. pp. 1225-1226.

[92] R. Sahoo, D.M.R. Kumar, D.A. Babu, K.G. Suresh, A.K. Nigam, M.M. Raja. Effect of annealing on the magnetic, magnetocaloric and magnetoresistance properties of Ni-Co-Mn-Sb melt spun ribbons, J. Magn. Magn. Mater. 347 (2013) 95-100.

[93] R. Barman, D. Kaur. Improved magnetocaloric effect in magnetron sputtered Ni–Mn–Sb–Al ferromagnetic shape memory alloy thin films, Vacuum 120 (2015) 22-26.

[94] A.K. Pathak, I. Dubenko, C. Pueblo, S. Stadler, N. Ali. Magnetism and magnetocaloric effects in $Ni_{50}Mn_{35-x}Co_xIn_{15}$ Heusler alloys, J. Appl. Phys. 107 (2010) 09A907.

[95] V.K. Sharma, M.K. Chattopadhyay, S.B. Roy. Large magnetocaloric effect in $Ni_{50}Mn_{33.66}Cr_{0.34}In_{16}$alloy, J. Phys. D: Appl. Phys 43 (2010) 225001.

[96] J. Ren, H.W. Li, S.T. Feng, Q.J. Zhai, J.X. Fu, Z.P. Luo, H.X. Zheng. Giant magnetocaloric effect in a Heusler $Mn_{50}Ni_{40}In_{10}$ unidirectional crystal, Intermetallics 65 (2015) 10-14.

[97] Z.G. Guo, L.Q. Pan, M.Y. Rafique, X.F. Zheng, H.M. Qiu, Z.H. Liu. Metamagnetic phase transformation and magnetocaloric effect in quinary $Ni_{45}Co_5Mn_{40}In_xSn_{10-x}$ heusler alloy, J. Alloy. Compd. 577 (2013) 174-178.

[98] W.H. Meikleiohn, C.P. Bean. New Magnetic Anisotropy, Phys. Rev. 102 (1956) 1413-1414.

[99] J. Nogués, I.K. Schuller. Exchange bias, J. Magn. Magn. Mater. 192 (1999) 203-232.

[100] M. Khan, I. Dubenko, S. Stadler, N. Ali. Exchange bias behavior in Ni-Mn-Sb Heusler alloys, Appl. Phys. Lett. 91 (2007) 072510.

[101] R.L. Wang, M.K. Lee, L.S. Xu, Z.G. Sun, V.V. Marchenkov, C. Tien, J.C.A. Huang, C.P. Yang. Effect of thermal cycle on the interfacial antiferromagnetic spin configuration and exchange bias in Ni-Mn-Sb alloy, AIP Advances 2 (2012) 032181.

[102] R.L. Wang, L.S. Xu, Z.G. Sun, V.V. Marchenkov, H.B. Xiao, L.F. Xu, J.C.A. Huang, C.P. Yang. Tuning exchange bias through zero field cooling from different remanent states above blocking temperature in $Ni_{50}Mn_{36}Sb_{14}$ alloy, Phys. Status Solidi RRL 6 (2012) 448-450.

[103] A.K. Nayak, K.G. Suresh, A.K. Nigam. Observation of enhanced exchange bias behaviour in NiCoMnSb Heusler alloys, J. Phys. D: Appl. Phys 42 (2009) 115004.

[104] A.K. Nayak, R. Sahoo, K.G. Suresh, A.K. Nigam, X. Chen, R.V. Ramanujan. Anisotropy induced large exchange bias behavior in ball milled Ni-Co-Mn-Sb alloys, Appl. Phys. Lett. 98 (2011) 232502.

[105] D.H. Wang, Z.D. Han, H.C. Xuan, S.C. Ma, S.Y. Chen, C.L. Zhang, Y.W. Du. Martensitic transformation and related magnetic effects in Ni-Mn-based ferromagnetic shape memory alloys, Chin. Phys. B 22 (2013) 077506.

[106] S.Y. Yu, L. Ma, G.D. Liu, Z.H. Liu, J.L. Chen, Z.X. Cao, G.H. Wu, B. Zhang, X.X. Zhang. Magnetic field-induced martensitic transformation and large magnetoresistance in NiCoMnSb alloys, Appl. Phys. Lett. 90 (2007) 242501.

[107] K. Bhattacharya. Theory of martensitic microstructure and the shape-memory effect. in: Müller I, Airoldi G, Miyazaki S, (Eds.). Shape memory alloys: from microstructure to macroscopic properties. Trans. Tech. Publications, 1998.

[108] E.C. Bain, N.Y. Dunkirk. Trans. AIME 70 (1924) 25-35.

[109] M.S. Wechsler, D.S. Lieberman, T.A. Read. On the theory of the formation of martensite, Trans. AIME 197 (1953) 1503-1515.

[110] J.S. Bowles, J.K. Mackenzie. The crystallography of martensite transformation I, Acta Metall. 2 (1954) 129-137.

[111] J.K. Mackenzie, J.S. Bowles. The crystallography of martensite transformation II, Acta Metall. 2 (1954) 138-147.

[112] J.S. Bowles, J.K. Mackenzie. The crystallography of martensite transformation III. Face-centred cubic to body-centred tetragonal transformations, Acta Metall. 2 (1954) 224-234.

[113] J.S. Bowles, J.K. Mackenzie. The crystallography of martensite transformation-IV body-centred cubic to orthorhombic transformations, Acta Metall. 5 (1957) 137-149.

[114] J.M. Ball, R.D. James. Fine phase mixtures as minimizers of energy, Arch. Ration. Mech. Anal. 100 (1987) 13-52.

[115] A.G. Khachaturyan. Theory of structural transformations in solids, John Wiley, New York, 1983.

[116] K. Bhattacharya. Wedge-like microstructure in martensites, Acta Metall. 39 (1991) 2431-2444.

[117] K.F. Hane, T.W. Shield. Microstructure in a cubic to orthorhombic transition, J. Elasticity 59 (2000) 267-318.

[118] K. Otsuka, K. Shimizu. Morphology and crystallography of thermoelastic γ' Cu-Al-Ni martensite, Jpn. J. Appl. Phys. 8 (1969) 1196-1204.

[119] K.F. Hane, T.W. Shield. Symmetry and microstructure in martensites, Philos. Mag. A 78 (1998) 1215-1252.

[120] R.D. James, K.F. Hane. Martensitic transformations and shape-memory materials, Acta Mater. 48 (2000) 197-222.

[121] J.Y. M., G.J. Weng. A direct method for the crystallography of martensitic transformation and its application to TiNi and AuCd, Acta Mater. 50 (2002) 2967-2987.

[122] K.F. Hane, T.W. Shield. Microstructure in the cubic to monoclinic transition in titanium–nickel shape memory alloys, Acta Mater. 47 (1999) 2603-2617.

[123] K.F. Hane, T.W. Shield. Microstructure in the cubic to trigonal transition, Mater. Sci. Eng. A 291 (2000) 147-159.

[124] J.L. Ericksen. Phase transformations and material instabilities in solids. in: Gurtin M, (Ed.). Academic Press, New York, 1984.

[125] J.M. Ball. Mathematical models of martensitic microstructure, Materials Science and Engineering: A 378 (2004) 61-69.

[126] H.J. Bunge, C. Esling, J. Muller. The role of the inversion centre in texture analysis, J. Appl. Cryst. 13 (1980) 544-554.

[127] H.J. Bunge, C. Esling, J. Muller. The influence of crystal and sample symmetries on the orientation distribution function of the crystallites in polycrystalline materials, Acta Cryst. A37 (1981) 889-899.

[128] M. Humbert, N. Gey, J. Muller, C. Esling. Determination of a Mean Orientation from a Cloud of Orientations. Application to Electron Back-Scattering Pattern Measurements, J. Appl. Cryst. 29 (1996) 662-666.

[129] Y.D. Zhang, Z.B. Li, C. Esling, J. Muller, X. Zhao, L. Zuo. A general method to determine twinning elements, J. Appl. Cryst. 43 (2010) 1426-1430.

[130] X. Balandraud, D. Delpueyo, M. Grédiac, G. Zanzotto. Almost compatible microstructures in shape memory alloys, Acta Mater. 58 (2010) 4559-4577.

[131] V. Petříček, M. Dušek, L. Palatinus. *JANA*2006, Institute of Physics, Prague, Czech Republic (2006).

[132] L. Righi, F. Albertini, G. Calestani, L. Pareti, A. Paoluzi, C. Ritter, P.A. Algarabel, L. Morellon, R.I. M. Incommensurate modulated structure of the ferromagnetic shape-memory Ni_2MnGa martensite, J. Solid State Chem. 179 (2006) 3525-3533.

[133] L. Righi, F. Albertini, E. Villa, A. Paoluzi, G. Calestani, V. Chernenko, S. Besseghini, C. Ritter, F. Passaretti. Crystal structure of 7M modulated Ni–Mn–Ga martensitic phase, Acta Mater. 56 (2008) 4529-4535.

[134] H.L. Yan, Y.D. Zhang, N. Xu, A. Senyshyn, H.-G. Brokmeier, C. Esling, X. Zhao, L. Zuo. Crystal structure determination of incommensurate modulated martensite in Ni–Mn–In Heusler alloys, Acta Mater. 88 (2015) 375-388.

[135] A. Sozinov, A.A. Likhachev, N. Lanska, K. Ullakko. Giant magnetic-field-induced strain in NiMnGa seven-layered martensitic phase, Appl. Phys. Lett. 80 (2002) 1746-1748.

[136] M. Pasquale, C.P. Sasso, L.H. Lewis, L. Giudici, T.A. Lograsso, D.L. Schlagel. Magnetostructural transition and magnetocaloric effect in $Ni_{55}Mn_{20}Ga_{25}$ single crystals, Phys. Rev. B 72 (2005) 094435.

[137] Z.B. Li, Y.D. Zhang, C. Esling, X. Zhao, Y.D. Wang, L. Zuo. New approach to twin interfaces of modulated martensite, J. Appl. Cryst. 43 (2010) 617-622.

[138] Z.B. Li, Y.D. Zhang, C. Esling, X. Zhao, L. Zuo. Twin relationships of 5M modulated martensite in Ni-Mn-Ga alloy, Acta Materialia 59 (2011) 3390-3397.

[139] D.Y. Cong, Y.D. Zhang, Y.D. Wang, C. Esling, X. Zhao, L. Zuo. Determination of microstructure and twinning relationship between martensitic variants in 53 at.%Ni–25 at.%Mn–22 at.%Ga ferromagnetic shape memory alloy, J. Appl. Cryst. 39 (2006) 723-727.

[140] C.Y. Zhang, H.L. Yan, Y.D. Zhang, C. Esling, X. Zhao, L. Zuo. Crystal structure and crystallographic characteristics of martensite in $Ni_{50}Mn_{38}Sb_{12}$ alloys, J. Appl. Cryst. 49 (2016) 513-519.

[141] G. Kurdjumov, G. Sachs. Z. Phys. 64 (1930) 325-343.

[142] Z. Nishiyama. Sci. Rep. Tohoku Imp. Univ. 23 (1934) 637-644.

[143] G. Wassermann. Mitt. K.-Wilh.-Inst Eisenforsch. 17 (1935) 149-155.

[144] W. Pitsch. Acta Metall. 10 (1962) 897-900.

[145] Z.Y. Zhang, R.D. James, S. Müller. Energy barriers and hysteresis in martensitic phase transformations, Acta Mater. 57 (2009) 4332-4352.

[146] R. Delville, D. Schryvers, Z.Y. Zhang, R.D. James. Transmission electron microscopy investigation of microstructures in low-hysteresis alloys with special lattice parameters, Scripta Mater. 60 (2009) 293-296.

Publication list

I: Publications in international journals

[1] **C. Y. Zhang**, H. L. Yan, Y. D. Zhang, C. Esling, X. Zhao, L. Zuo. Crystal structure and crystallographic characteristics of martensite in $Ni_{50}Mn_{38}Sb_{12}$ alloys, J. Appl. Cryst. 49 (2016) 513-519.

[2] H. L. Yan, **C. Y. Zhang**, Y. D. Zhang, X. L. Wang, C. Esling, X. Zhao, L. Zuo. Crystallographic insights into Ni–Co–Mn–In metamagnetic shape memory alloys, J. Appl. Cryst. 49 (2016) 1585-1592.

[3] **C. Y. Zhang**, Y. D. Zhang, C. Esling, X. Zhao, L. Zuo. Martensitic transformation orientation relationship and martensite variant organization of $Ni_{50}Mn_{38}Sb_{12}$ alloy, J. Appl. Cryst. under review.

[4] **C. Y. Zhang**, Y. D. Zhang, C. Esling, X. Zhao, L. Zuo. Microstructural and crystallographic insights of in a martensite and / austenite concomitant dual phase Ni-Mn-Sb alloy, Adv. Eng. Mater. under review.

II: Contributions to International Conferences

[1] **C. Y. Zhang**, H. L. Yan, Y. D. Zhang, C. Esling, X. Zhao, L. Zuo. Crystal structure and microstructure characteristics of $Ni_{50}Mn_{38}Sb_{12}$ metamagnetic shape memory alloy, **Anisotropy and Texture 2015, Metz (France)**. (**Poster**)

[2] C. Esling, **C. Y. Zhang**, Y. D. Zhang, X. Zhao, L. Zuo. Martensitic transformation orientation relationship and martensite variant organization of $Ni_{50}Mn_{38}Sb_{12}$ alloy, **XXV International Materials Research Congress 2016, Cancun (Mexico)**. (**Invited lecture**)

Acknowledgements

The present work is accomplished at the Laboratoire d'Étude des Microstructures et de Mécanique des Matériaux (LEM3), UMR CNRS 7239, Université de Lorraine, Metz, France, and the Key Laboratory for Anisotropy and Texture of Materials (ATM), Northeastern University, Shenyang, China. I have the honor to work with numerous colleagues in the two laboratories and I would like to give my hearted thanks for their kind help.

I gratefully acknowledge the China Scholarship Council (CSC) for providing a PhD scholarship. This work is supported by the National Natural Science Foundation of China (Grant No. 51431005) and the 863 Programme of China (Grant No. 2015AA034101),.

I would like to sincerely thank all the jury members for taking time out of their busy schedules to achieve my dissertation defense, and special gratitude to Professor Leo KESTENS and Professor Yinong WANG for their evaluation of my dissertation and for the constructive suggestions and comments.

I sincerely extend my deepest gratitude to my supervisors, Dr. Yudong ZHANG at Université de Lorraine, France, and Professor Xiang ZHAO at Northeastern University, China, for their guidance and support to my PhD work and their constant and selfless help in my daily life. I would also like to express my appreciation to Professor Liang ZUO for insightful guidance to this work. Lastly, I would like to express my sincerely gratitude to Professor Claude ESLING for his help in my academic study and daily life.

I would like to express my thanks to Mr. Jérôme SLOWENSKY, Ms. Auriane MANDRELLI, Ms. Jacqueline DECKER, Ms. Nathalie KASPRZAK, Ms. Anne-martine BLUM and Ms. Arlette JACQUIERRE at LEM3, France, and Dr. Tong HE, Dr. Xinli WANG, Dr. Na XIAO, Ms. Minkun GAO, Ms. Yiqiao YANG and Ms. Henghe ZHAO at Northeastern University, China, for their technical and administrative help and support to my PhD work.

I am also grateful to all the staffs and students in the two laboratories, LEM3 and ATM, and my friends who shared their experiences with me and offered help to my study, especially to Dr. Haile YAN, Dr. Xiaorui LIU, Dr. Zongbin LI, Dr. Cai CHEN, Dr. Yajun ZHAO, Dr. Jiangkun FAN, Mr.

Naifu ZOU, Mr. Yu ZHANG, Mr. Shun XU, Mr. Ke HUA, Ms. Chunqing LIN, Ms. Xiaomeng LIU, Ms. Meishuai LIU, Ms. Chunhua WANG, Ms. Jing WEN, Ms. Dan ZHAO. Special thanks to Dr. Cai CHEN, Ms. Li ZUO and my young friend Ms. Pengru ZHAO for their endless help in my daily life.

Last but not least, I would like to express my deep love and gratitude to my parents and my family members who have always been loving, helping, encouraging and supporting me in my life.